

WP16 – MMC Test Bench Demonstrator

Deliverable 16.4 - Test Case Analysis

PROMOTiON – Progress on Meshed HVDC Offshore Transmission Networks
Mail info@promotion-offshore.net
Web www.promotion-offshore.net

This result is part of a project that has received funding from the European Union's Horizon 2020 research and innovation programme under grant agreement No 691714.

Publicity reflects the author's view and the EU is not liable of any use made of the information in this report.

CONTACT

DOCUMENT INFO SHEET

Document Name: Deliverable 16.4
Responsible partner: RWTH
Work Package: WP 16
Work Package leader: RWTH
Task: Task 16.6: Demonstration of defined test cases regarding interoperability, control schemes and protection
Task lead: RWTH

DISTRIBUTION LIST

PROMOTioN partners, European Commission

APPROVALS

	Name	Company
Validated by:		
Task leader:	Fisnik Loku	RWTH
WP Leader:	Philipp Ruffing	RWTH

DOCUMENT HISTORY

Version	Date	Main modification	Author
1.0			All listed authors

WP Number	WP Title	Person months	Start month	End month
16	MMC Test Bench Demonstrator	106.8	M24	M54

Deliverable Number	Deliverable Title	Type	Dissemination level	Due Date
16.4	Test Case Analysis	Report	Public	30.09.2020

LIST OF CONTRIBUTORS

Work Package and deliverable involve a large number of partners and contributors. The names of the partners, who contributed to the present deliverable, are presented in the following table.

PARTNER	NAME
RWTH AACHEN	Fisnik Loku, Matthias Quester, Philipp Wienkamp, Markus Kaiser, Philipp Ruffing
UPV	Soledad Bernal-Perez, Jaime Martínez, Ramón Blasco-Gimenez
DTU	Amir Arasteh
KTH	Ilka Jahn, Mehrdad Nahalparvari
DNV GL	Yongtao Yang, Alessandro Iannarelli, Leonel Noris Martinez
Orsted	Mohammad Kazem Dowlatabadi, Lorenzo Zeni

EXECUTIVE SUMMARY

Within Work Package 16 of the PROMOTioN project, the operation and control of meshed high-voltage direct current (HVDC) systems as well as their interaction with offshore wind power plants (WPPs) is investigated. While previous work packages of the project, i.e. WP2, WP3 and WP4, focus on simulation-based investigations regarding the challenges associated with the control and protection of future MTDC networks and the connected WPPs, WP16 continues their analysis using power and control hardware as well as a laboratory scaled MTDC demonstrator.

Within this deliverable, the HVDC converter controls developed in WP2 are demonstrated using a 4-terminal bipolar configuration with (lab-scaled) power hardware components. Therefore, a Power-Hardware-in-the-Loop (PHIL) test bench is set up. The results obtained from the laboratory setup are compared with its corresponding lab-scale simulation model and a simulated full-scale model. The comparison shows a high degree of conformity between the test bench results and the simulated models, and thereby increase the confidence for the developed converter control concepts. Moreover, two fault clearing approaches in HVDC networks are demonstrated using the test bench: A protection strategy based on fault blocking converters and a protection strategy based on fast DC circuit breakers. The obtained results show a high degree of consistency with the corresponding simulation models and thereby confirm the theoretical feasibility of the fault clearing approach shown in WP4 as well as the fault clearing approach with the DC-bypass concept, respectively.

The investigations carried out analytically in an RMS simulation tool within WP2 regarding frequency support solutions for HVDC grids are demonstrated using real-time EMT simulations and the MMC Test Bench converter controls. To demonstrate the developed communication-less frequency support approach between asynchronous AC systems, a point-to-point connection in the EMT time-domain simulation toolbox Hypersim is utilised, where the two synchronous ac systems are represented in an IEEE 39 bus case. The obtained results confirm the RMS investigations carried out in WP2 and that the MMC control, which was developed for the other study cases including the MMC Test Bench, works also for the frequency support investigations.

Furthermore, wind turbine and wind park controllers developed within WP3 of PROMOTioN are validated in realistic scenarios utilising a Controller-Hardware-in-the-Loop (CHiL) demonstrator setup. To assess the system performance of the test cases defined within WP3, a HVAC black start operation scenario as well as a scenario consisting of point-to-point Diode Rectifier Unit (DRU) connections are setup. The results obtained from the CHiL implementation show good matching with the results obtained from WP3 regarding the HVAC black start operation and the grid forming controllers for DRU operation.

In addition, the impedance measuring methods developed in PROMOTioN are successfully applied on two demonstrators: The MMC Test Bench laboratory at RWTH Aachen and the wind turbine control replica system at DNV GL, Arnhem. The derived impedances are used to investigate potential instabilities due to converter control interactions in non-fault situations in offshore networks in the frequency domain. The investigation results reveal that the measurement-based approach does not require the exchange of detailed models and component data, enabling stability and interaction studies of systems not owned by a single entity.

CONTENT

- Document info sheet** 1
 - Distribution list 1
 - Approvals 1
 - Document history 1
 - List of Contributors 2
- Executive Summary** 3
- 1 Introduction** 1
 - 1.1 Context within PROMOTioN 2
 - 1.2 Objective and Scope of Work 4
- 2 PROMOTioN Test Benches** 5
 - 2.1 Overview 5
 - 2.2 MMC Test Bench 5
 - 2.2.1 Overview 5
 - 2.2.2 Test Levels and Demonstration Approach 10
 - 2.2.3 Power-Hardware-in-the-Loop Setup for the MMC Test bench 11
 - 2.2.4 Protection IED 12
 - 2.2.5 DC Circuit Breaker 14
 - 2.3 Wind Power Plant – CHiL Test bench 15
 - 2.3.1 System Description 15
 - 2.3.2 Basic Test System 17
 - 2.4 MMC CHiL Test Bench 18
- 3 MTDC Grid Demonstration** 20
 - 3.1 Introduction 20
 - 3.2 MTDC bipolar network configuration 20
 - 3.2.1 Network Setup and Test Case 20
 - 3.3 Fault Clearing in HVDC Networks 25
 - 3.3.1 Non-Selective Fault Clearing based on FB-MMC 26
 - 3.3.2 DC-Bypass 32
 - 3.4 Frequency Support via MTDC networks 38
 - 3.4.1 Introduction 38
 - 3.4.2 System and Control Setup 39
 - 3.4.3 Communcation-Less Frequency Support 41
 - 3.4.4 Conclusion 45

- 3.5 Fault-ride-through and frequency response tests in MMC CHiL test bench 46
 - 3.5.1 Fault-ride-through test 46
 - 3.5.2 Frequency response 48
- 4 Grid Forming WPP Demonstration 51**
 - 4.1 Introduction..... 51
 - 4.2 CHiL compliance evaluation of offshore WT and WPP controllers for HVAC black start operation 51
 - 4.2.1 System Description 51
 - 4.2.2 Sequential Black Start Procedure 52
 - 4.2.3 Machine Side Converter Control 53
 - 4.2.4 Grid Side Converter Control..... 54
 - 4.2.5 Start up and synchronization of the WTGs connected to the first string 55
 - 4.2.6 Off shore substation energisation using POW 57
 - 4.2.7 Export cable energization (direct connection) 59
 - 4.2.8 On shore substation energisation (POW)..... 62
 - 4.2.9 40 MW power block connection / disconnection 63
 - 4.2.10 Synchronisation to existing on-shore HVAC grid 65
 - 4.2.11 HVAC export cable fault..... 67
 - 4.2.12 Soft start Energisation..... 68
 - 4.2.13 Discussion..... 70
 - 4.3 CHiL compliance evaluation of offshore WT and WPP controllers for point-to-point Diode Rectifier Unit (DRU) connections 70
 - 4.3.1 System Description 70
 - 4.3.2 Grid Side Converter Control..... 71
 - 4.3.3 Dynamic voltage control during islanding operation (DRU not conducting) 72
 - 4.3.4 Filter connection and change from islanded to connected operation 73
 - 4.3.5 Intentional Islanding..... 74
 - 4.3.6 Off-shore ac faults (ring bus fault)..... 75
 - 4.3.7 Discussion..... 76
- 5 Stability Analysis in Offshore Networks..... 78**
 - 5.1 Introduction..... 78
 - 5.2 MMC Impedance Derivation Method 79
 - 5.2.1 DC side impedance 79
 - 5.2.2 AC side impedance..... 82
 - 5.3 AC Side MMC Impedance Models..... 84
 - 5.3.1 Impedance Scaling 85

- 5.4 OWP Impedance Derivation 87
- 5.5 Stability Assessment Offshore MMC and Wind Farm 88
 - 5.5.1 Frequency Domain Stability Assessment 89
- 5.6 Stability Assessment Onshore MMC and AC Grid 94
 - 5.6.1 Frequency Domain Stability Assessment 95
 - 5.6.2 Time Domain Validation 99
- 5.7 Conclusion 100
- 6 Recommendations 102**
- 7 Summary and Conclusions 106**
- 8 References 108**

1 INTRODUCTION

Within the framework of the modernisation of the European electricity grid, multi-terminal HVDC (MTDC) offshore grids connecting several tens to hundreds of gigawatts of wind power from the Northern Seas shall be integrated into the surrounding AC transmission systems. Additionally, offshore MTDC networks are foreseen as interconnectors between large synchronous zones (e.g. ENTSO-E, UK and the Nordic Grid). However, MTDC systems lead to novel challenges for transmission grid operators, grid planners and manufacturers. To increase the experience regarding the operation of these systems as well as their interaction with AC transmission systems and the offshore Wind Power Plants (WPP), novel demonstration methods that can lift the technology readiness level of the control of HVDC and wind turbine converters have to be exploited.

Within Work Package 16 (WP16) of PROMOTioN, the operation and control of multi-terminal and even meshed HVDC systems as well as their interaction with offshore WPPs is investigated. While previous work packages of the project, i.e. WP2, WP3 and WP4, focus on simulation-based investigations regarding the challenges associated with the control and protection of future MTDC networks and the connected WPPs, WP16 continues their analysis using power-hardware-in-the-loop (PHiL) and controller-hardware-in-the-loop (CHiL) methods as well as both full-scale and laboratory scaled demonstrators.

Accordingly, the main objectives of the work package are the:

- **Demonstration** of applicability of developed controls and simulation models of PROMOTioN
- **Technical de-risking** for the deployment and continuous operation of meshed HVDC-systems
- **Improvement** of the feasibility of MTDC grids for road mapping processes and standardization efforts

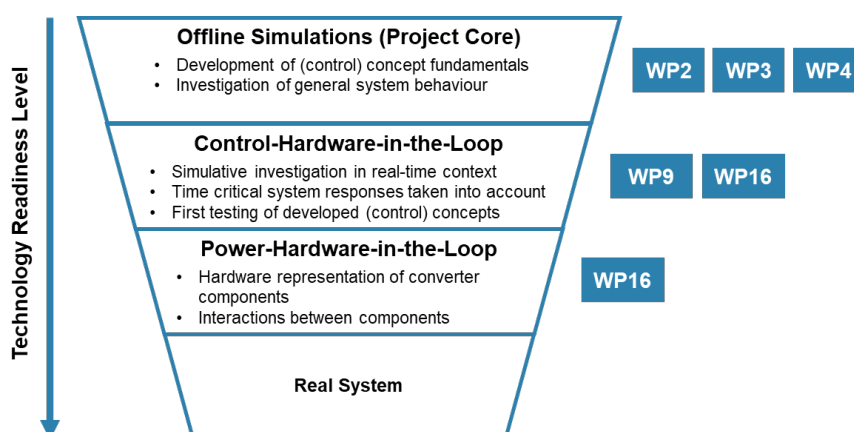


Figure 1-1: Technology-Readiness-Level of converter and grid control method within the PROMOTioN project

1.1 CONTEXT WITHIN PROMOTION

A key aspect of WP16 is to demonstrate the knowledge gained in the technical work packages of PROMOTioN. This includes grid operation and control concepts for meshed and DRU connected DC networks from WP2, the wind turbine and wind power plant controls developed in WP3 and protection strategies from WP4. Additionally, it is an objective of WP16 to integrate the protection IED developed in WP4 into a Power-Hardware-in-the-Loop (PHIL) test bench.

The findings of WP16 will be used as an input for WP11 and WP12, to contribute to the standardisation efforts and the elaboration of a roadmap for future meshed offshore DC networks. The interactions of WP16 with other work packages of PROMOTioN is illustrated in Figure 1-2.

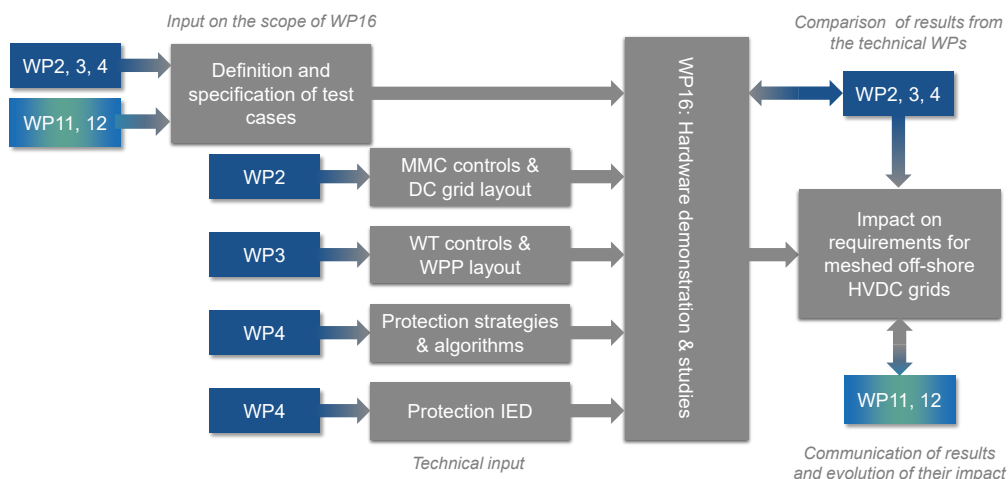


Figure 1-2: Illustration of the link between WP16 and other work packages of PROMOTioN

To create a strong link between the technical work packages – especially WP2, WP3 and WP4 – as well as the deployment plan of PROMOTioN (WP12) test cases have been defined and documented in collaboration in Deliverable D16.1 [1]. Based on these test cases three main work streams for WP16 have been defined. These are also shown in Figure 1-3.

MTDC Test Bench

A central part of WP16 is the demonstration of the general controllability of meshed offshore grids. Therefore, the generic control algorithms developed in WP2 have been transferred onto the controllers of the MMC Test Bench system in order to demonstrate their functionality. The test cases include the controllability and interoperability of HVDC grids and the offshore WPP as well as the proposed frequency support concepts. Another important aspect is the demonstration of HVDC grid protection concepts, in particular regarding the converter behaviour during DC fault operation. Although simplifications have to be made in a down-scaled laboratory test bench, the functionality of protection chain is strongly indicative of correct operation and it is analysed for several cases and scenarios.

Therefore, the protection IED developed in WP4 is integrated in the Test Bench system as well. With these demonstrations, it is the objective of WP16 to increase the TRL of HVDC converter controls.

DRU-connected and black-start offshore WPPs

WP3 introduced a procedure for the compliance evaluation of WPP and grid forming wind turbine controllers for the HVDC connection of WPPs using diode rectifiers and also for compliance evaluation of WPP and WTG controllers for service restoration after a black-out. These two applications are particularly relevant for the cost-effective integration of WPPs into systems with a high percentage of renewable energy. The procedure in WP3 included the functional requirements, scenarios and test cases to be used for controller compliance evaluation using detailed simulations. The work carried out in WP16 extends the compliance evaluation procedure developed in WP3 to a real-time Control Hardware-in-the-Loop system, which allows for an increase on the wind turbine controllers TRL.

Stability Assessment in Offshore Networks

In addition to the demonstrations relating to the investigations of previous work packages, WP 16 addresses a topic that has not been investigated in PROMOTiON so far. Being identified as crucial for the operations of offshore HVDC systems, the presented stability analysis addresses instabilities in offshore networks due to converter control interactions. Two test cases are defined to assess the stability and potential interactions between a grid following MMC and the onshore AC grid as well as between a grid forming MMC and an offshore wind farm. Moreover, the test cases aim at validating a frequency-domain stability assessment by utilizing measured impedances that enables the study of the stability of multiple scenarios. A measurement-based impedance derivation method is used to demonstrate how stability can be assessed when components are owned by different entities and no internal information of the components or models can be shared.

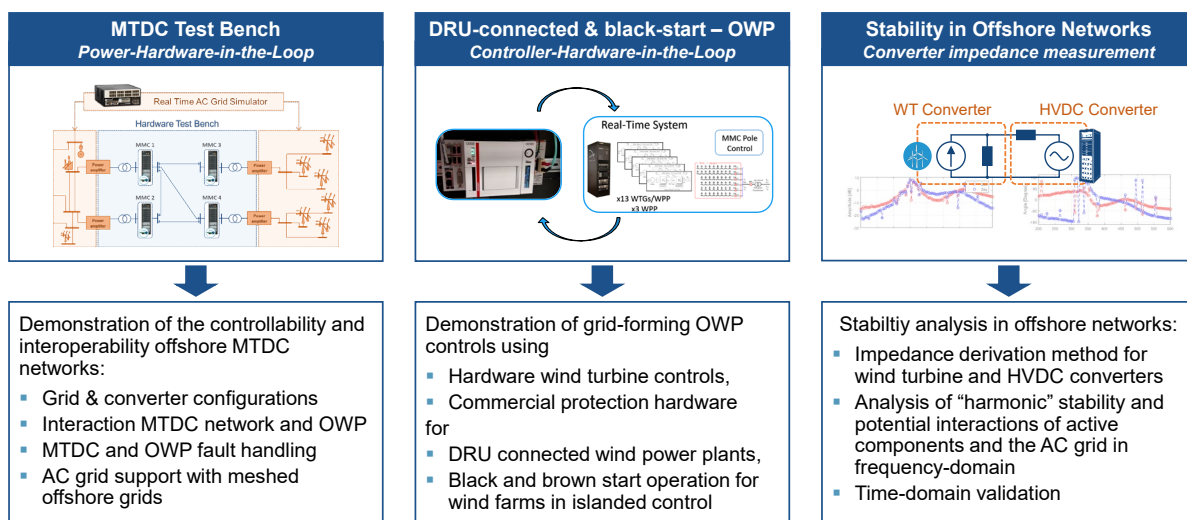


Figure 1-3: Overview about the scope of WP16

1.2 OBJECTIVE AND SCOPE OF WORK

Within this deliverable, the converter controls developed in WP2 of PROMOTioN are demonstrated for a bipolar configuration in a MTDC network. Furthermore, two fault handling approaches are demonstrated as well. The grid forming WPP controls developed within WP3 as well as the black start of an entire DRU-connected offshore wind farm (OWF) are demonstrated utilising a CHiL setup. Lastly, the stability analysis of offshore HVDC networks is carried out in frequency domain.

The objectives and main contributions of this work are:

- The 4-terminal symmetric monopole configuration demonstrated in D16.3 is adopted to a 4-terminal bipolar configuration. The bipolar model is implemented as a simulated full-scale model, simulated lab-scale model and with the MMC Test Bench. The results of the simulated models and the MMC Test Bench are compared and the grid-following controls for a bipolar configuration of the MMC stations are demonstrated. The difference between the physical lab system, its simulation model replica and a full-scaled model are evaluated.
- Demonstration of the unidirectional communication less frequency support developed in WP 2.
- Two fault clearing strategies are demonstrated using the MMC Test Bench:
 - Non-selective fault clearing based on fault blocking converters, where the DC voltage and the DC current are actively controlled to near-zero values by full-bridge MMCs prior to opening the DC circuit breakers.
 - Fault separation based on fast DC circuit breakers – Here, no active control of the DC voltage and current occurs before opening the DC circuit breakers. Using the developed IED, the DC circuit breakers are triggered and thus interrupt the full DC fault current.
- Wind turbine and wind park controllers are validated for realistic scenarios using a CHiL demonstrator. To assess the system performance, a HVAC black start operation as well as a point-to-point configuration of a diode rectifier-based connection are demonstrated.
- To analyse the stability of offshore networks, the frequency dependent impedances of the converter stations, which are considered as black-boxes, are derived. Here, two different methods are described, which are used to derive the frequency dependent impedance from the AC and the DC side, respectively. Furthermore, the frequency dependent impedance of the OWF is derived as well as the stability of a HVDC connected OWF is analysed using the developed approaches. Finally, the stability assessment in frequency-domain is validated using time-domain simulations.

Based on the technical analysis and the demonstrations carried out within WP16, recommendations towards future grid codes, the (compliance) testing of converter controllers and further research are summarised in chapter 6.



2 PROMOTION TEST BENCHES

2.1 OVERVIEW

In this chapter, the laboratory demonstrators that are used within WP16 are described. These include:

- The MMC Test Bench, a PHIL system consisting of hardware laboratory scaled modular multilevel converter stations
- A controller-hardware-in-the-loop (CHiL) demonstrator for the investigation of grid-forming offshore wind power plants
- A controller-hardware-in-the-loop (CHiL) demonstrator for the investigation of the interoperability of a commercial MMC and wind turbine converter controller

Regarding the MMC Test Bench, section 2.2 summarises the description containing the basic technical description is provided.

2.2 MMC TEST BENCH

2.2.1 OVERVIEW

The MMC Test Bench comprises of simulated AC systems, e.g. AC grids and offshore wind farms (OWFs), and a hardware DC grid consisting of eight laboratory-scaled modular multilevel converters (MMCs), DC circuit breaker models as well as pi-line sections. The AC systems are simulated in Hypersim or Matlab/Simulink and RT-Lab and implemented in an RTS: an OPAL-RT OP5707. The coupling of the simulated AC systems with the hardware DC grid is achieved via linear power amplifiers (PAs) at the AC-side of the MMCs and the MMC Test Bench consists of four linear PAs in total. The PAs can either be configured in voltage source mode or current source mode. The choice depends on the control of the connected systems. The MMC Test Bench can be configured as an eight-terminal symmetrical monopole configuration or as a four-terminal bipolar configuration. Furthermore, each MMC station includes an RTS (an OPAL-RT OP4510), where the MMC control algorithm is implemented. Here, the upper level control of the MMC is implemented on the Central Processing Unit (CPU) of the RTS and the lower level controls are implemented on the Field Programmable Gate Array (FPGA) of the RTS. The dispatch controller of the MMCs and the supplementary control levels are implemented on a separate OP4510 RTS. The schematic system configurations of the symmetrical monopole and bipolar MTDC networks are presented in Figure 2-1.

Each Test Bench MMC is a three-phase converter comprised of the six arms with a nominal DC voltage of $V_{DC,n} = 400$ V. The number of submodules per phase-arm is 10 and therefore the nominal cell voltage is $V_{c,n} = 40$ V. The nominal DC current of the MMC is $I_{DC,n} = 15$ A and the nominal output power of the MMC is $P_{DC,n} = 6$ kW. Regarding the nominal AC voltage and nominal AC RMS current, the MMC is rated at



$V_{AC,1}/V_{AC,2} = 400/208$ V phase to phase and $I_{AC} = 16.7$ A respectively. The switching frequency of the power electronic switches (MOSFETs) can be adjusted as needed for a specific test case. The cell capacitors and the arm inductors of the MMC are $C_{SM} = 4.92$ mF and $L_{Arm} = 2.5$ mH respectively. The MMC ratings of the full-scale system and the MMC Test Bench are presented in Table 2-1.

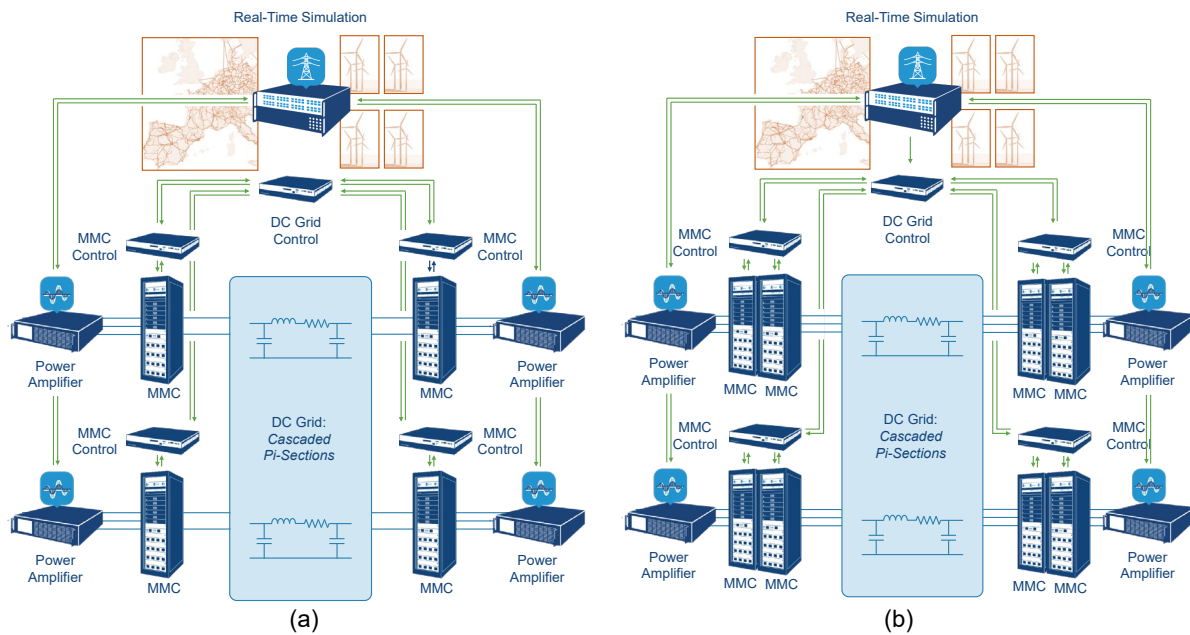


Figure 2-1: Laboratory setup as (a) symmetrical monopole and (b) bipolar DC network

Table 2-1: MMC parameters

Full-scale MMC (simulation only)		Ratings	MMC Test Bench (lab-scale)		Ratings
Nominal DC voltage	$V_{DC,n}$	640 kV	Nominal DC voltage	$V_{DC,n}$	400 V
Nominal DC current	$I_{DC,n}$	1.875 kA	Nominal DC current	$I_{DC,n}$	15 A
Nominal output power	$P_{DC,n}$	1200 MW	Nominal output power	$P_{DC,n}$	6 kW
Nominal AC voltage; LL-RMS	$V_{AC,1}$ $V_{AC,2}$	400 kV 350 kV	Nominal AC voltage; LL-RMS	$V_{AC,1}$ $V_{AC,2}$	400 V 208 V
Nominal AC RMS current	I_{AC}	2.582 kA	Nominal AC RMS current	I_{AC}	16.7 A
No. of Submodules	n_{sub}	350	No. of Submodules	n_{sub}	10
IGBT switching frequency	f_{sw}	10 kHz	MOSFET switching frequency	f_{sw}	0-10 kHz

The submodules can be configured as half-bridge or full-bridge. The submodules are designed for a nominal voltage and current of 40 V and 15 A_{RMS} respectively. The maximum switching frequency of the submodules is 10 kHz and the on/off propagation delay is less than 100 ns. Additionally, the submodule consists of a cell bypass electronic switch, which enables the submodules to be bypassed if required (see Figure 2-2). Furthermore, cell current measurement is also included. The measurements are sent to the controller using a 12-bit, 500 kbps serial sampling analogue/digital converter (ADC). A fixed hardware instantaneous overcurrent detection is also part of the submodules' inner-protection. The submodule parameters are summarised in Table 2-2.

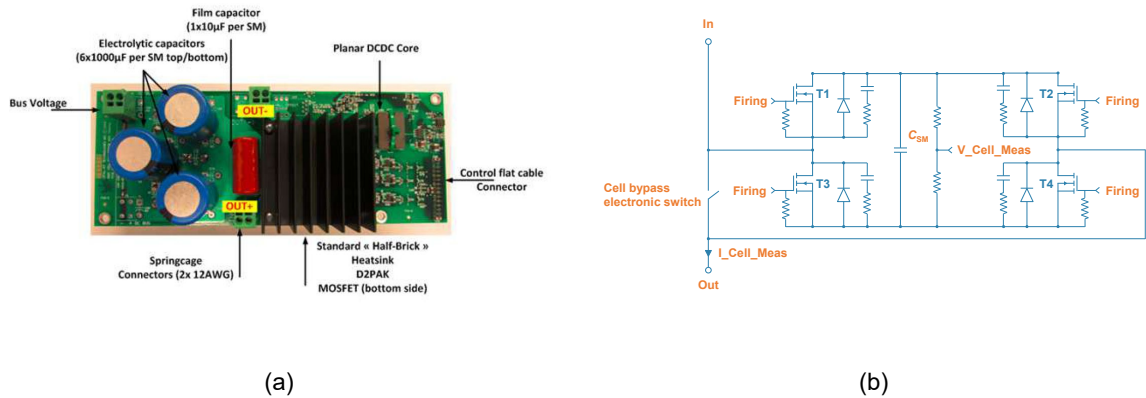


Figure 2-2: (a) picture and (b) equivalent circuit of a submodule [1]

Table 2-2: Submodule Parameters

Submodule designs		half- and full-bridge
Capacitor value	C_{SM}	4.92 mF
Arm inductor	L_{Arm}	2.5 mH
Nominal current	$I_{SM,n}$	15 A _{RMS}
Nominal voltage	$V_{SM,n}$	40 V
Maximum switching frequency	$f_{SW,Max}$	10 kHz
On/off propagation delay		≤ 100 ns

Table 2-3 shows the transformer parameters that are used in the MMC Test-Bench. Each of the eight 3-phase transformers is integrated in one MMC rack. The transformers are rated at a power of $S_{Tr} = 8$ kVA and are built in Y/Δ-configuration. The primary side and the secondary side voltages are rated at $V_{Tr,1} = 400$ V_{RMS} and $V_{Tr,2} = 208$ V_{RMS} respectively.

Table 2-3: Transformer parameters

Rated Power	S_{Tr}	8 kVA
Configuration		Y/Δ
Nominal primary voltage: Y(phase-phase, RMS)	$V_{Tr,1}$	400 V _{RMS}
Nominal primary voltage: Δ (phase-phase, RMS)	$V_{Tr,2}$	208 V _{RMS}

Figure 2-3 shows the schematic laboratory set-up of the minimal meshed network developed within WP2 and investigated in D16.3 [2]. The AC grid and the OWF are implemented as full-scale simulated models using real time simulators and the corresponding simulation tools. The measured voltages and currents from the simulated AC grids and OWF are scaled down to their laboratory scaled values and then are provided as reference signals to the respective power amplifiers. The PAs are connected to the hardware laboratory scaled MMC stations and the DC grid is represented by Pi-line sections.

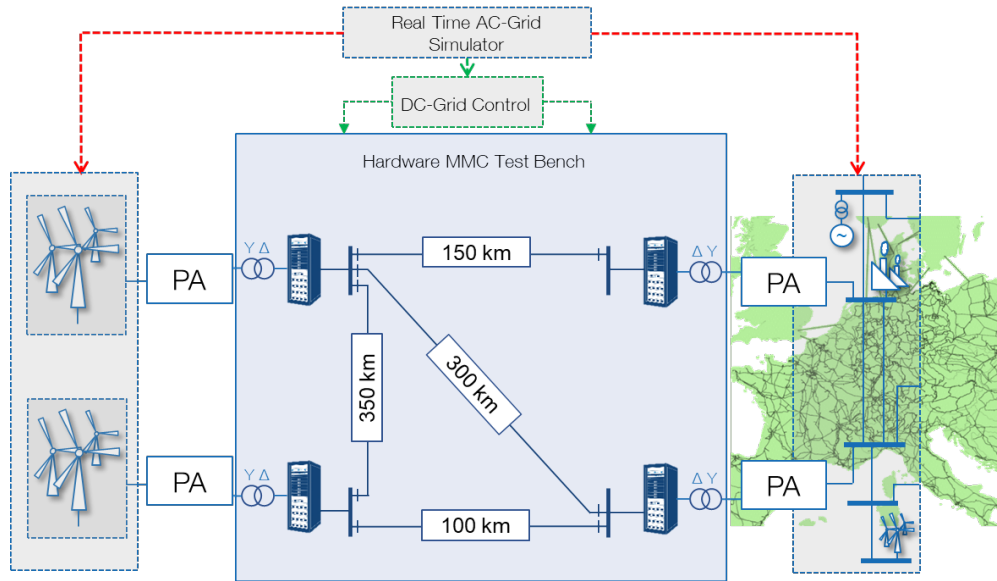


Figure 2-3: Laboratory set-up of the minimal meshed network with Pi-sections as DC cable representation

To design a cable for a lab-scaled system remains a challenge. For the MMC Test Bench cascaded Pi-sections are used to emulate the DC line connection between the MMCs. The cable parameters for the MMC Test Bench are based on a cable design of a 320-kV submarine cable. The cable is initially designed in the EMT software tool PSCAD-EMTDC, where the cable equivalent Pi-section parameters are extracted. The Pi-section parameters for the full-scale system are then scaled down according to the following relations of the rated voltages and powers of the full-scale and lab-scale systems:

$$Z_{LS} = Z_{FS} \cdot \frac{1200 \text{ MW}}{(640 \text{ kV})^2} \cdot \frac{(400 \text{ V})^2}{6000 \text{ W}} \quad (2.1)$$

For the investigation of fault clearing, the Pi-sections are extended to represent the transient behaviour of a cable more accurately. This is done by creating several parallel resistive inductive paths in the main current path of the Pi-sections [3, 4]. The extended Pi-section is called Pi³-section in the following and is shown in Figure 2-4.

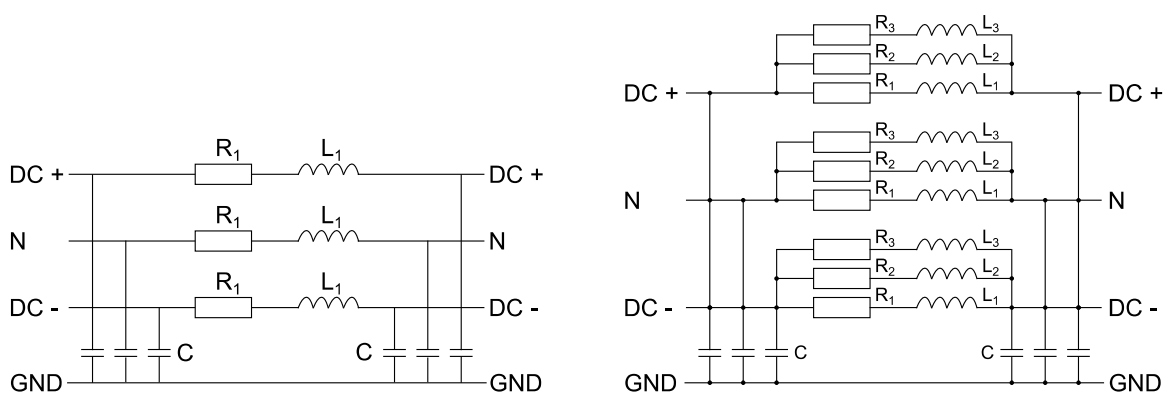


Figure 2-4: Transmission line model (Pi-section and Pi³-section)

Figure 2-5 illustrates the differences in the transient transmission behaviours of the Pi-section, Pi³-section and the Universal Line Model (ULM) cable model in the time domain. In the figure, the simulated output voltage is shown at the end of a 100 km long cable. At the beginning of the cable a voltage step from 200 V to 0 V in 1 ms is simulated to represent a pole-to-ground fault. Compared to the Pi-section, the Pi³-section is able to reproduce the transmission behaviour of the ULM cable model more accurately. Thus, it is concluded that the Pi³-sections are suitable for the proof of concept demonstrations of different protection strategies within WP16.

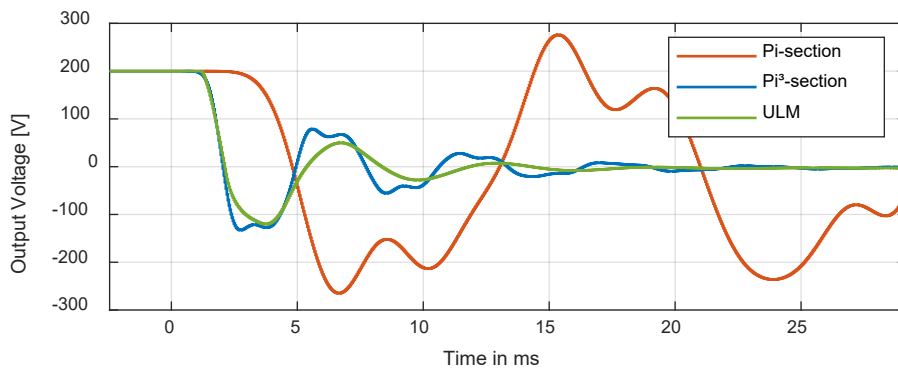


Figure 2-5: Simulated comparison of different cable representations after fault occurrence

The parameters of the used components are provided in Table 2-4. To test different network topologies, cable and overhead line configurations, the capacitance of each Pi-section and Pi³-section can be individually set to 25 μF , 50 μF or 100 μF . Each Pi-section represents a length of $l_{\text{Pi}} (\pm 200 \text{ V}) = 50 \text{ km}$ at a nominal DC voltage of $V_{\text{DC}} = \pm 200 \text{ V}$ and $l_{\text{Pi}} (\pm 400 \text{ V}) = 25 \text{ km}$ at a nominal DC voltage of $V_{\text{DC}} = \pm 400 \text{ V}$. Each Pi³-section represents a length of $l_{\text{Pi}^3} (\pm 200 \text{ V}) = 38 \text{ km}$ at a nominal DC voltage of $V_{\text{DC}} = \pm 200 \text{ V}$ and $l_{\text{Pi}^3} (\pm 400 \text{ V}) = 19 \text{ km}$ at a nominal DC voltage of $V_{\text{DC}} = \pm 400 \text{ V}$. The total number of Pi-sections and Pi³-sections is 32.

Table 2-4: Pi-section and Pi³-section Parameters

Component		Pi-section	Pi ³ -section
Resistance (inner resistance of the inductor)	R_1	37 m Ω	37 m Ω
Inductance	L_1	10 mH	10 mH
Capacitance	C	100 / 50 / 25 μF	100 / 50 / 25 μF
Resistance	R_2	-	220 m Ω
Resistance	R_3	-	330 m Ω
Inductance	L_2	-	4,7 mH
Inductance	L_3	-	1 mH

The Pi-sections and Pi³-sections are integrated in six cabinets. The connection of different grid configurations is done by using insulated 4 mm copper cables.

2.2.2 TEST LEVELS AND DEMONSTRATION APPROACH

Prior to the demonstration of the models that are developed to investigate certain network topologies and control algorithms, the models are initially developed as offline simulation models utilising electromagnetic transient (EMT) simulation tools. In order to increase the confidence in the developed network configurations or control algorithms, a demonstration is required. However, a demonstration with a full-size DC grid at high voltage is limited to very specific cases due to the high costs and missing infrastructure. As an alternative approach, HiL systems, such as CHiL or PHiL systems are considered. HiL implementations require prior offline simulation and digital twin simulation studies, the developed concepts with the simulated full-scale models may not directly be ready to be implemented using hardware components. The alternative possible approach to obtain solutions at the high-voltage level is shown in Figure 2-6. With this approach the differences between the simulated full-scale models and the simulated lab-scale models are initially identified and analysed. Proper adjustments are conducted, so that certain phenomena of the simulated full-scale model can be more accurately represented at a simulated lab-scale model. The simulated lab-scale model is then compared to the hardware implementation with the MMC Test Bench. Considering the limitations of the MMC Test Bench, differences between the simulated lab-scale model and the MMC Test Bench are identified and analysed

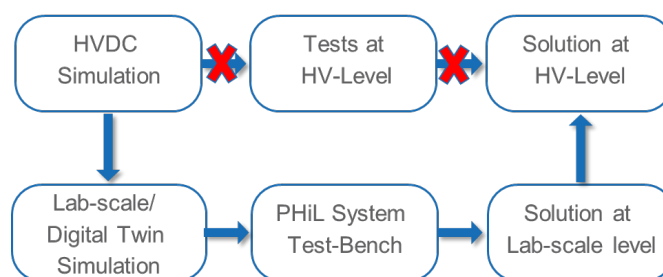


Figure 2-6: Possible approach to obtain solutions at full-size DC grid

The steps described in the described approach, can be typically grouped into three more general stages are considered:

1. Offline simulation:

In offline simulation, everything including the AC grids, the power plants, the DC grid, the physical components and the converter controls is simulated. The offline simulation is typically used to design and simulate the test case that will be demonstrated with the MMC Test Bench.

2. Digital Twin simulation:

The digital twin of the MMC Test Bench includes simulated converter stations in a RTS excluding their respective converter controls. The converter controls are implemented in separate RTS. The converter stations are therefore controlled independently, at asynchronous simulation times including all the inner protection logic of the hardware converter stations of the MMC Test Bench. The communication between the simulated converter stations and the corresponding converter controls implemented with separate RTS is done via SFP connections. Before implementing a certain model with the MMC Test Bench, the digital twin simulation is a crucial step in order to ensure that no protection logic is activated from the

control. Otherwise a direct test with the MMC Test Bench may lead to a fault modus for the MMC converter stations, which is more complicated to debug in the RTS environment.

3. Hardware-in-the-loop (HiL) simulation:

3.1. Controller-Hardware-in-the-loop (CHiL):

In CHiL simulation, the power plant is simulated and a real controller is used. Typically, this method is used to test real controllers within a simulated power plant. HiL can be an open loop simulation or a closed loop simulation. The closed loop simulation is the more common of the two types. In the closed-loop simulation, the signals are sent to the device under test through the real time simulator. The measurement signals are given back to the real time simulator (and the control) as the response of the device under test. The communication between the real time simulator and the device under test typically is provided by analogue signals, i.e. low voltage levels of ± 10 V.

3.2. Power-hardware-in-the-loop:

In PHiL simulation, power devices such as converters are also included in the simulation. In contrast to HiL simulations, the PHiL simulations can run test cases at the full power required by the device under test. Power amplifiers are used in PHiL in order to make the required connection from the real time simulator to the included power devices.

A comparison of the results obtained from a simulated full-scale model, simulated lab-scale model and a HiL system provides a possibility to analyse and study the differences between the models, which can be used to enhance the simulation models as well as the HiL systems in order to ensure a “good quality” matching of the results and demonstration of a respective test case. The consistency of all three stages ensures that the demonstration corresponds to a test in a full-size DC grid with the highest possible confidence. All test cases are therefore considered successful if the following conditions are met:

1. The full functionality of the examined test cases is shown.
2. The consistency in all three demonstration stages is given.

2.2.3 POWER-HARDWARE-IN-THE-LOOP SETUP FOR THE MMC TEST BENCH

In this section, a general introduction to PHiL is initially given and then the PHiL interface algorithm is introduced, that is used to implement the PHiL connected offshore wind farms, for the demonstration of controllability and interoperability of an MTDC network in chapter 0.

To couple a simulated network with hardware components, several PHiL interfaces, such as the Ideal Transformer Method (ITM) or the Damping Impedance method (DIM) can be applied [2]. For the demonstration of the 4-terminal MTDC network including wind speed set point changes, ITM is applied as it is an interface algorithm with a high accuracy [5]. ITM can be implemented as a voltage or a current type and this is shown in Figure 2-7. The voltage type ITM is typically used for a network consisting a simulated voltage source and a hardware component. Here, the simulated voltage is measured and it is provided as a reference voltage to a controlled voltage source (CVS) on the hardware side of the network. As a result, a current flow on the hardware side of the network and this current is measured and provided to a simulated controlled current source (CCS). For the current type ITM, the current is measured at the simulated side of the network and provided to a CCS on the hardware side of the

network. Here, the voltage is measured and is provided as a reference signal to the CVS on the simulated side of the network.

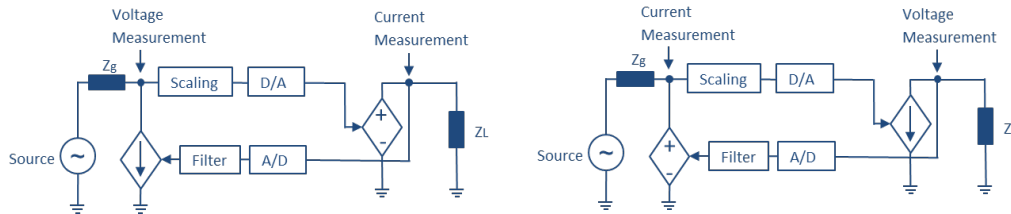


Figure 2-7. ITM interface algorithm – voltage type (left), current type (right) [2]

A challenge for PHIL investigations is the design of the interface algorithm between the hardware components and the RTS due to the instabilities that can occur when the whole system is considered. These instabilities can be for instance the measurement noises that can influence the measured voltage or current on the simulation side of the circuit, which then can be transferred and amplified to the hardware side of the network. The overall stability also depends on the strength of the simulated grid, as a strong grid is normally less susceptible to the effects of the measurement noise. The transfer functions of the above-described ITM algorithms are presented in (2.2) and (2.3), respectively [5]:

$$G_{ITM_V} = -\frac{Z_g}{Z_L} \cdot e^{-s\Delta t} \quad (2.2)$$

$$G_{ITM_I} = -\frac{Z_L}{Z_g} \cdot e^{-s\Delta t} \quad (2.3)$$

where, Δt is the time delay of the interface. Z_L and Z_g are the equivalent impedances in the hardware circuit and the simulated network, respectively. The indexes V and I represent the transfer function of the voltage and current type, respectively. Depending on the relation of the equivalent impedance of the simulated network Z_g and the equivalent impedance of the hardware network Z_L , the interface algorithms can be stable or not. Using the Nyquist Criterion, an impedance ratio greater than one would mean that the interface algorithm is not stable and a value of smaller than one would mean a stable interface algorithm.

Due to its high accuracy characteristics and its stability characteristics, the ITM method is utilised for the PHIL implementation of the AC grids and the OWF. For the PHIL implementation of the AC grids, the voltage type ITM can be utilised and for the implementation of the OWF the current type ITM is utilised, as described in deliverable D16.3 [2].

2.2.4 PROTECTION IED

A protection intelligent electronic device (IED), formerly called relay, has the task to correctly detect and identify faults, and initiate the required actions in protective equipment. In an HVDC system, this could include, e.g., trip signals for DC circuit breakers, MMC blocking/de-blocking signals, or trip signals for AC circuit breakers or high-speed switches. The specifics depend on the chosen protection philosophy and resulting equipment. For coordination within a multi-terminal HVDC substation, three options for an IED configuration have been proposed [6], i.e., as (1) standalone protection device, (2) integrated in a converter control and protection system, and

(3) integrated in the HVDC circuit breaker control and self-protective system. Here, a standalone IED prototype is being used for testing.

This IED prototype shown in Figure 2-8 was developed in PROMOTiON WP4 [7] and has previously been tested low-voltage real-time simulator setups in WP 9 [8–10] with a purely simulated surrounding system. Now, this IED is used in a setup with real down-scaled MMCs, real short-circuits, and real hardware for DCCB emulation.

The IED is designed as platform for research and therefore the software and hardware is modular by design and easily adaptable to different purposes. The design is available open source [11]. The original design was adapted to be compatible with the MMC test-bench measurements and the emulated DCCB trip input level.



Figure 2-8: IED prototype

In particular, the IED has three independent functional units that each execute a set of protection algorithms. Since the damping of the pi-links in the down-scaled MMC test-bench is larger than in a full-scale HVDC system, the travelling wave behaviour of the faults can currently not be used for selective fault detection with e.g. dv/dt , or travelling wave extraction algorithm. However, in the presented test cases, selective fault detection was not required such that an undervoltage criterion was used. An example screenshot of the IED graphical user interface is shown in Figure 2-9.

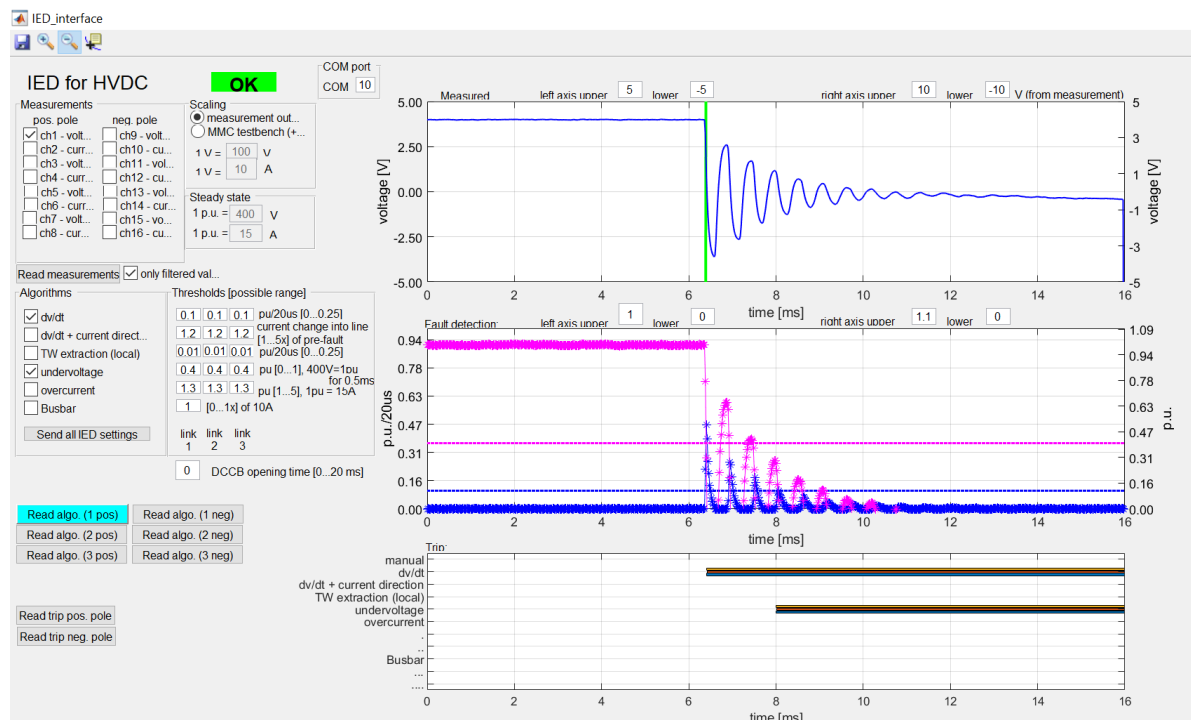


Figure 2-9: IED graphical user interface

2.2.5 DC CIRCUIT BREAKER

A dc circuit breaker model was prototyped at KTH according to the specifications of the MMC test bench at RWTH Aachen. A solid-state circuit breaker design was adopted which consists of two anti-series connected IGBTs with antiparallel diodes to allow stopping the current flow in both directions. During the on-state operation, a current path is provided through an IGBT and the freewheeling diode of the other semiconductor. In case of a fault in the line, the semiconductors are turned off. The stored energy in the line inductance however, increases rapidly until the metal oxide varistor (MOV, modelling a surge arrester) connected in parallel with the circuit breaker clamps the voltage to a certain level. Figure 2-10 demonstrates the solid-state circuit breaker with anti-series IGBT connection in a dc line.

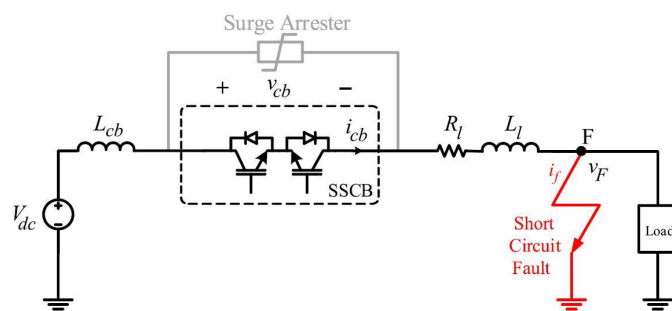


Figure 2-10: solid-state dc circuit breaker model in a dc line under fault.

The circuit breaker model is rated for 400 V, 15 A, also capable of stopping a peak current of 30 A. This is allowed mainly by using IGBT modules rated 1200 V and 51 A. IGBT drivers with sufficient protection circuits are selected which are powered by a switched-mode power supply. Custom-made adapter boards are designed to connect the gate signal coming from the protection control and logic circuit to the IGBT driver board. Figure 2-11 shows the circuit breaker prototype including its main components. The prototype is put into an enclosure box with IGBTs placed on a heat sink. The on/off signals to the IGBT driver should be provided by a protection mechanism which detects the fault in the line. In this case, the KTH designed protection intelligent electronic device (IED) was used to detect the faults and send gate signals to the circuit breaker.

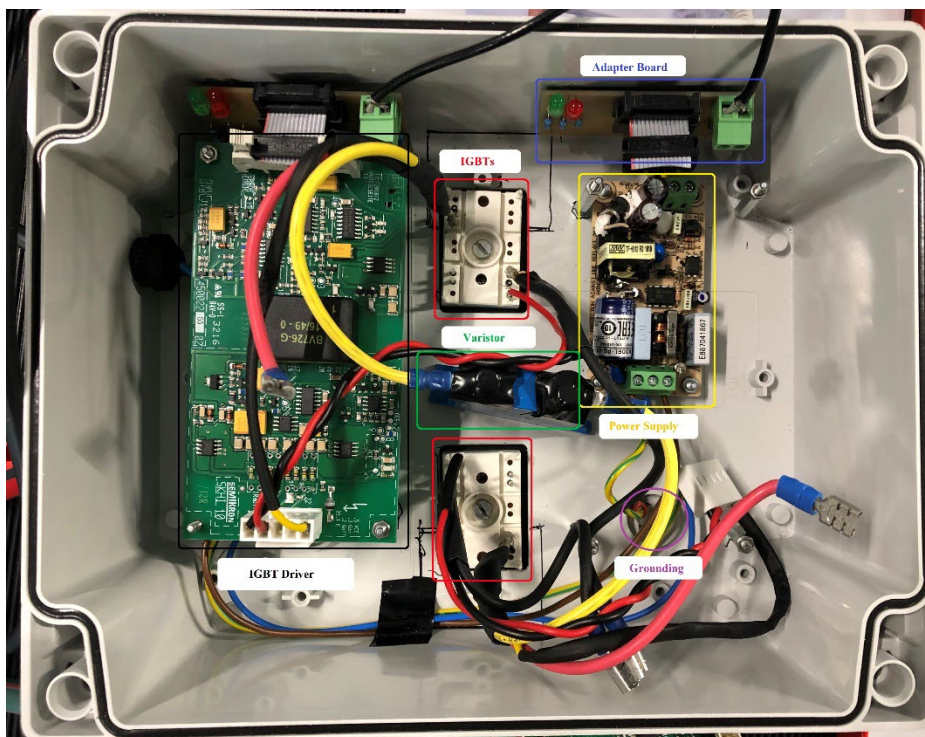


Figure 2-11: Main components of the mini circuit breaker model prototype

2.3 WIND POWER PLANT – CHIL TEST BENCH

2.3.1 SYSTEM DESCRIPTION

The real time simulation test bench is configured with the aim of CHIL testing of grid forming WTG and WPP strategies for both DRU connection and black-start operation. The CHIL consists of a real time simulation system based on OPAL-RT, which includes the converter, grid and part of the control system. It includes a link to open source Aeroelastic simulation software (NREL FAST). Interfaces to external converter and wind plant control and to differential and distance protection relays are also considered, using standard UDP and Ethernet connections. System configuration is shown in Figure 2-12.

Real-Time System: The eMegaSim OPAL-RT 5700 is the core of the system. It will simulate all the electrical components of every individual wind turbine (generator, machine side converter, DC-link, grid side converter, filters, transformer and breakers). The OPAL-RT 5700 will also simulate the off-shore AC-grid, DRU converter, HVDC cable and on-shore MMC-HVDC converter station (FPGA based simulation). The system can simulate up to 6000 submodules (Half-bridge, full-bridge, hybrid, mixed) at 250ns sampling time. The FPGA valve control can be either included in the FPGA or from an external controller by means of Aurora communication, following ENTSO-e standard for real time system HVDC controller communication. The pole controller is included in one core of the OPAL-RT 5700 system, although an external controller can also be used.

The individual wind turbine model includes PWM operation of both the grid side and the machine side converters. Due to the computational requirements of such converters, a maximum of 30 wind turbines is considered. Therefore, for each wind power plant, one string is simulated in detail and the others are simulated by means of aggregated models, which represent a reasonable level of aggregation for this kind of studies.

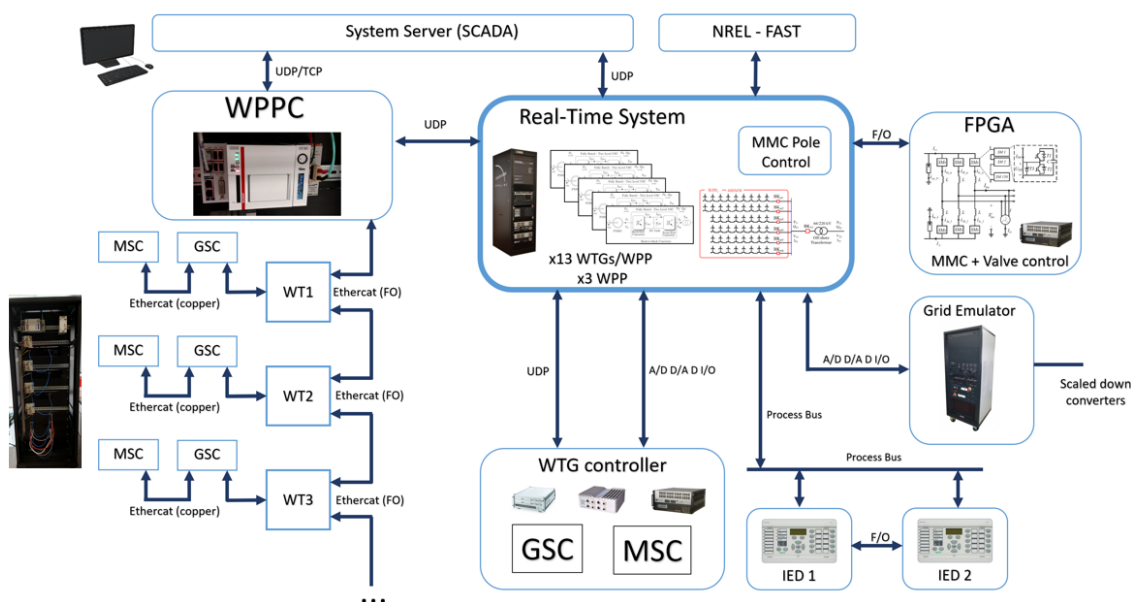


Figure 2-12: Set-up of the WPP CHiL test bench

Wind Turbine Generator Controller: It is implemented on a separated OPAL-RT 5600 system, which connects to the OPAL-RT 5700 system by means of digital and analogue channels. Due to the input/output limitation, only a limited number of WTGs will be controlled by the OPAL-RT 5600. The control of the remaining WTGs is carried out by one of two options:

1. Several cores of the OPAL-RT 5700
2. Several Ethercat connected DSP based converter control boards. The software development tool-chain guarantees that the control code used for real time simulation is exactly the same as that used for the EMT simulations.

Protection system: Two MiCOM P543 Easergy protection relays have been included in the CHiL set up. The chosen relays are designed for line/cable and transformer feeder applications. They include a high-speed current differential protection and distance option.

Grid emulator: Future extensions in test include the grid emulator to scale other elements in the system.

2.3.2 BASIC TEST SYSTEM

To check the operation of the system, a DRU-HVDC baseline case has been implemented in the OP5700, together with the wind farm controller and protection devices. For the basic test system, both system and controllers are included in the real-time simulation system (either in the DPU or the FPGA)

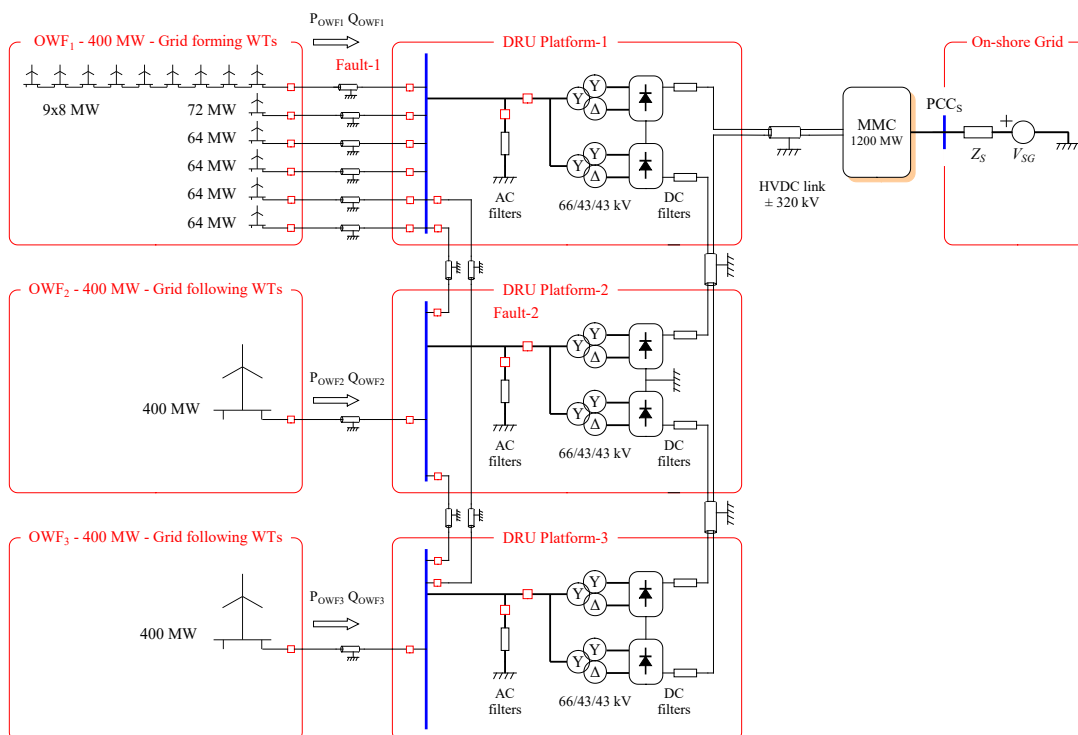


Figure 2-13 Base line scenario with three DRU platforms and on-shore VSC MMC station

The baseline scenario considers:

- **Off-shore Wind Farms (OWFs):** The system considers three OWFs of 400 MW each connected to a 66kV off-shore AC grid. Each OWF is composed of 50 x 8MW WT and WT are distributed in 6 strings (4 strings of 8 WTs and 2 of 9 WTs). Considered distances between WTs are 2 km, and the distances from an OWF to a DC platform are 4 km, as described in section 5.2 of Deliverable 3.1. (1 detailed string + 5 aggregated strings + 2 aggregated OWF)
- **Off-shore Transmission System (OTS):** The off-shore transmission system comprises the DRU stations, the HVDC cable, the HVAC auxiliary cable and on-shore converter station.
- **DRU platforms:** The DRU platforms contain two 200MW DRU, with the corresponding AC filters and harmonic compensators, (as described in 3.2 of Deliverable 2.1) and the corresponding switchgear. The umbilical off-shore side breaker and shunt compensator are also located on a DRU platform.
- **On-shore station:** It contains the on-shore MMC converter 1200MW (401 levels), on-shore transformer, on-shore OLTC transformer for the umbilical cable, a shunt compensator, and breakers for connection/disconnection of umbilical cable. For the baseline scenario, it is assumed ± 320 kV HVDC

cable 150km. Specific studies might use a different distance. The parameters for the different elements are included in PROMOTioN Deliverables D2.1 and D3.1.

2.4 MMC CHIL TEST BENCH

In addition to the investigations using the lab-scaled MTDC test bench (a small scale PHIL configuration), a CHIL systems is set up at DNV GL in Arnhem to investigate the interoperability between commercial WTG and MMC converters. The MMC CHIL test bench comprises the following key components:

1. An OPAL-RT real-time simulator consisting of OP5700 and an I/O-extension box OP7000.
2. Five controller cabinets from MMC vendor NR Electric:
 - a. HVDC Pole Control and Protection (PCP) Station 1, HVDC PCP Station 2, HVDC Valve Base Controller (VBC)
 - b. STATCOM PCP, STATCOM VBC
3. A 1-MW wind turbine controller replicas from MingYang Wind Power.

This test bench was developed to perform CHIL tests for the grid integration of offshore wind power plants, using AC or DC technology. Within WP16 two test cases are analysed – a direct AC connection of a WPP to shore including a STATCOM and a connection via HVDC. The schematic illustration of the AC and DC test cases are shown in Figure 2-14 and Figure 2-15, respectively.

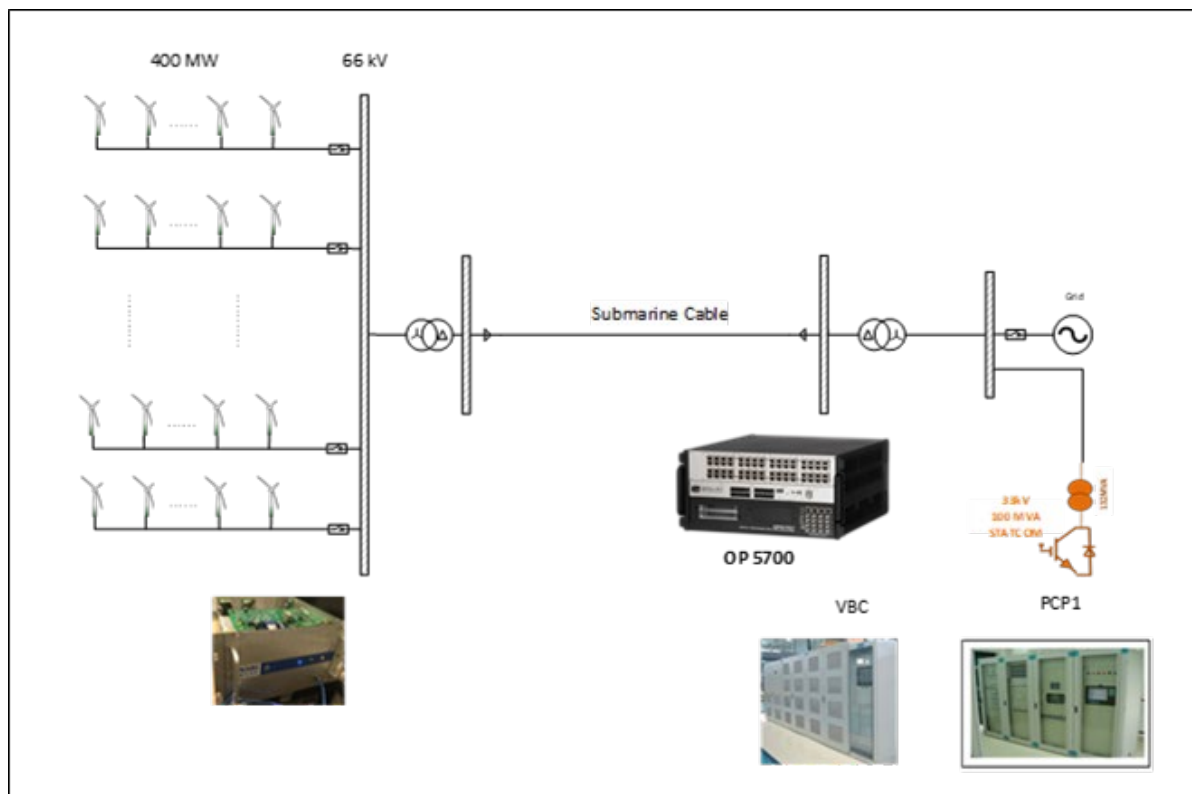


Figure 2-14 MMC CHIL test bench – AC connected offshore wind power plant with STATCOM onshore

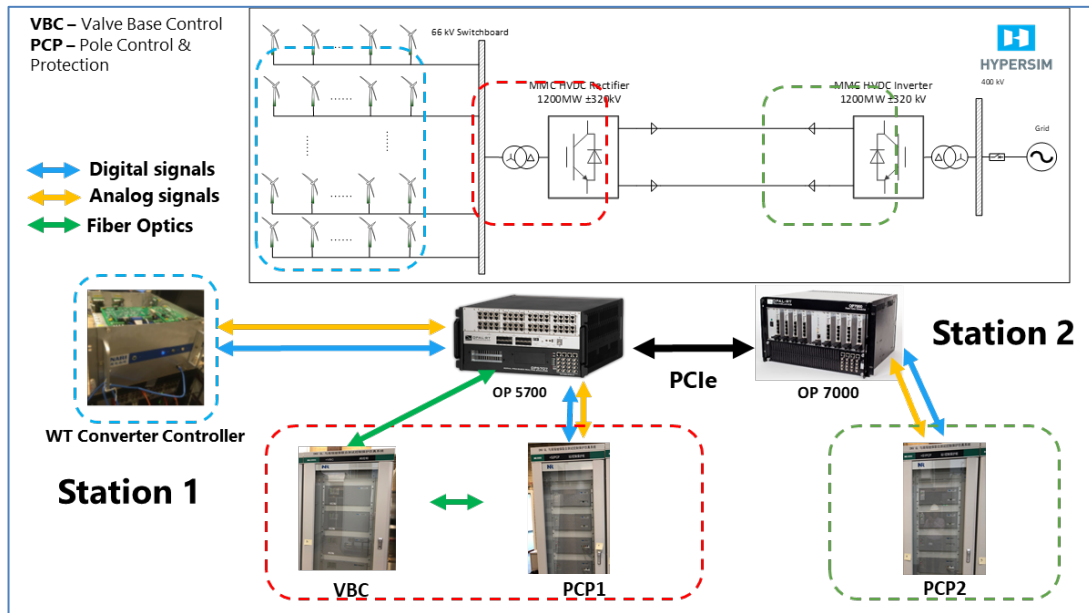


Figure 2-15 CHIL MMC testbench – VSC HVDC connected offshore wind power plants

The technical parameters for the DC case are as follows:

- Power: 1200 MW
- DC voltage: ± 320 kV, Half bridge VSC, symmetric monopole configuration
- Each of the six converter arms will consist of 292 sub-modules.
- Due to the relatively high number of cells per arm, two valve controls are needed for each arm (Valve Control)

The Human Machine Interface (HMI) implemented for the investigations is shown in Figure 2-16.

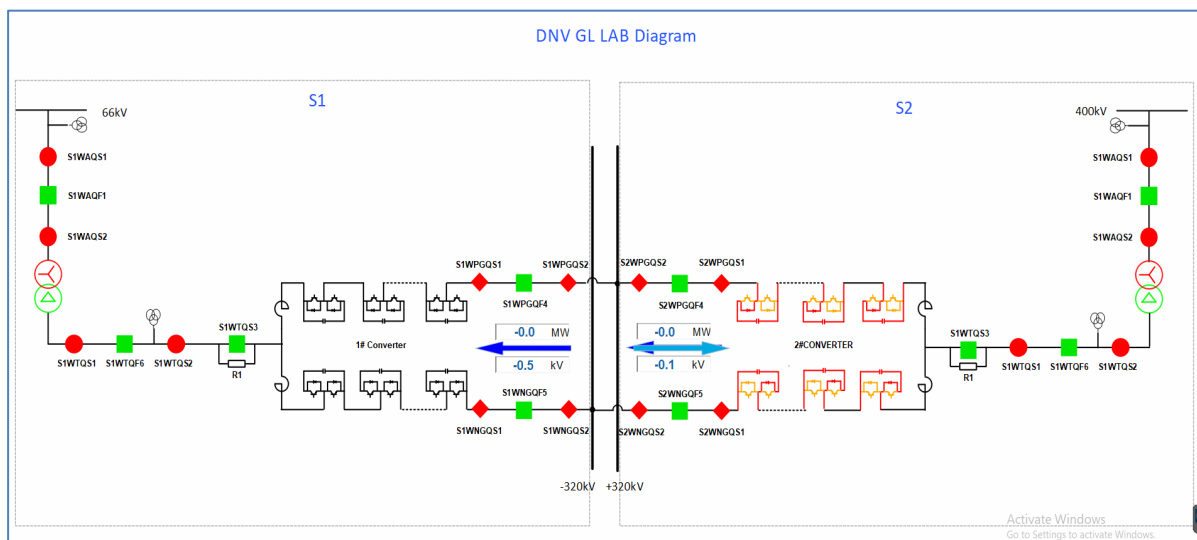


Figure 2-16 Human Machine Interface screenshot of the vendor's SCADA system

3 MTDC GRID DEMONSTRATION

3.1 INTRODUCTION

Following up the demonstration of the grid forming control MMC stations done in deliverable D16.3, where the 4-terminal network configuration developed in the PROMOTiON WP2 with two offshore wind farms (OWFs) and two AC grids was used, in this deliverable the 4-terminal network is implemented in a bipolar configuration in section 3.2. To do so, the bipolar configuration is initially implemented as a full-scale model. Then the bipolar configuration is scaled down such that the system parameter specifications correspond to the MMC Test Bench specifications and it is implemented as a full-scale model. Lastly, the simulated model is implemented using the MMC Test Bench. The results between the simulated models and the MMC Test Bench are compared and the differences are analysed.

After the demonstration of the MMC controls in a bipolar MTDC network, in section 3.3, two fault-handling strategies are demonstrated using the MMC Test bench: a fault-handling strategy based on fault blocking converters, where a bipolar point- to-point configuration is chosen for the demonstration purposes, and a fault-handling strategy based on fast DC circuit breakers, where a MTDC symmetrical monopole configuration is used. Afterwards, the demonstration of the frequency support concept developed in WP2 is shown in section 3.4. Finally, the results of the MMC/WTG-CHiL are presented in 3.5.

3.2 MTDC BIPOLAR NETWORK CONFIGURATION

3.2.1 NETWORK SETUP AND TEST CASE

The investigated bipolar configuration is shown in Figure 3-1.

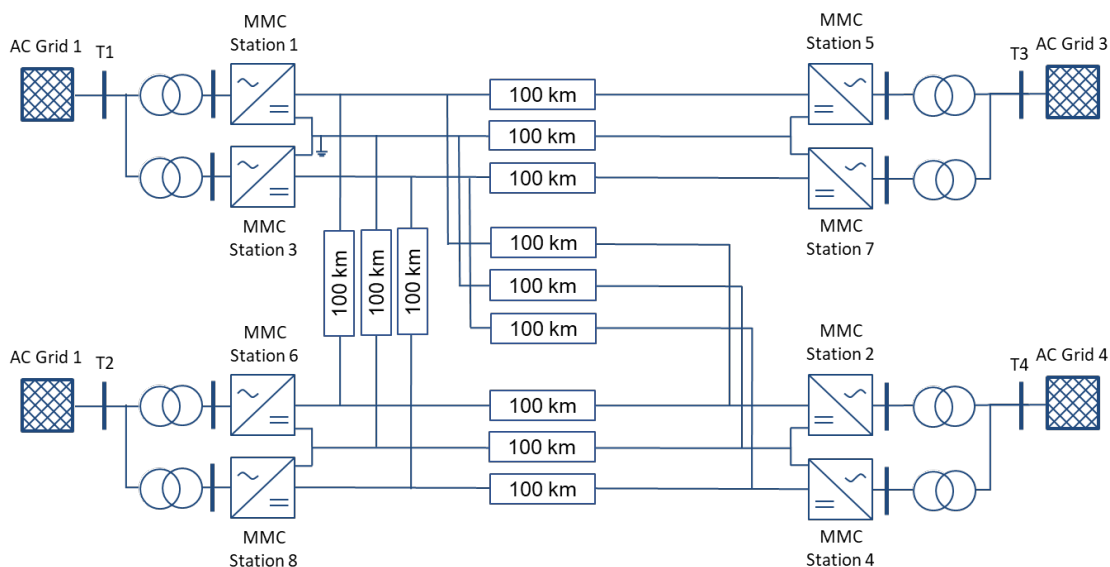


Figure 3-1: The investigated bipolar network configuration

START-UP-SEQUENCE OF THE MMC STATIONS

Depending on the control mode of the MMC stations, the start-up sequence is initiated either from the AC side or the DC side, respectively. At first, an MMC station must be activated as the DC voltage must be provided by the first activated MMC station. After a voltage is provided by the AC grid, the AC main contactor is closed and the submodules start to charge via a pre-charging resistance. After the submodules are charged close to their nominal voltage levels, the pre-charging resistors are bypassed by closing the ac bypass contactor. Here, the SM reach their nominal values and the DC main and bypass contactors are closed, so that a DC voltage can be measured. Finally, the MMC control is enabled and the DC voltage is controlled to its reference value. For the other MMC stations, the start-up sequence is analogous to the described start-up sequence for the grid following MMC station and is done starting from the DC side.

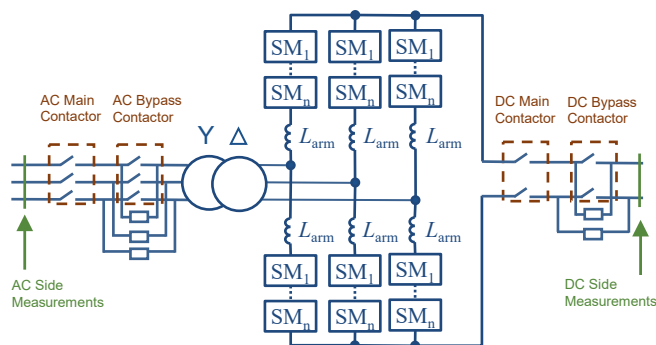


Figure 3-2: Schematic representation of an MMC station including the contactors

TEST CASE

MMC station 1 and MMC station 3 control the DC voltage to $V_{DC,p} = + 1$ p.u. and $V_{DC,n} = - 1$ p.u., respectively. MMC station 6 and MMC station 8 control the active power to $P_{ref} = - 0.5$ p.u. MMC station 5 and MMC station 7 control the active power to $P_{ref} = 0.5$ p.u. as well. MMC station 2 and MMC station 4 are initially configured to control the active power to $P_{ref} = 0.5$ p.u. At time $t = 1$ s, the active power reference of MMC station 2 and MMC station 4 changes to $P_{ref} = 1.0$ p.u. The DC voltages and active power measured at all MMC stations is compared for the simulated full-scale model, simulated lab-scale model and the MMC Test Bench.

3.2.1.1 RESULTS AND DISCUSSION

The MMC Test Bench in contrast to the offline simulation models has parasitic resistances such as the resistance of the cable connection from the MMC to the Pi-sections. In order to for the simulated lab-scale model to represent the MMC Test Bench more accurately, these additional resistances are implemented at the DC outputs of the MMC stations of the simulated lab-scale model. The cable resistances of the cable connection from the MMC stations to the Pi-sections is measured and has a value of approximately $R_{additional} = 0.2 \Omega$.

Figure 3-3 shows the DC voltage measured at the positive and negative poles of MMC station 1, MMC station 3, MMC station 5 and MMC station 7. At MMC station 1 and MMC station 3, the DC voltage is controlled to $V_{DC,p} = + 1$ p.u. and $V_{DC,n} = - 1$ p.u., respectively. The measured DC voltage of the simulated full-scale model

(green), the simulated lab-scale model (red) and the MMC Test Bench (blue) shows very similar and no significant difference between the models can be observed. At MMC stations 5 and 7, there is a very close match between the DC voltages measured for the simulated models and the MMC Test Bench. Compared to the DC voltage at MMC station 1 and 3, where it is controlled to exactly $V_{DC,p} = + 1.0$ p.u. and $V_{DC,n} = - 1.0$ p.u., respectively, the DC voltage at MMC station 5 and 7 has a value of $V_{DC,p} = + 1.013$ and $V_{DC,n} = - 1.013$ p.u. for the simulated lab-scale model and the MMC Test Bench. For the simulated full-scale model, the value of the DC voltage at MMC station 5 and 7 is $V_{DC,p} = + 1.002$ and $V_{DC,n} = - 1.002$ p.u., respectively. A higher DC voltage value at MMC station 5 and MMC station 7 is expected for the models, as an active power of $P = 0.5$ p.u is transferred into the DC grid. However, this difference in the DC voltage amplitude of the simulated full-scale model when compared to the simulated lab-scale model and the MMC Test Bench, leads to the conclusion that for the simulated lab-scale model and the MMC Test Bench, where the DC grid is represented by Pi-sections, the losses are higher. Here however, the additional resistances that come from the cable connections of the MMC stations to the Pi-sections must be taken in consideration as well.

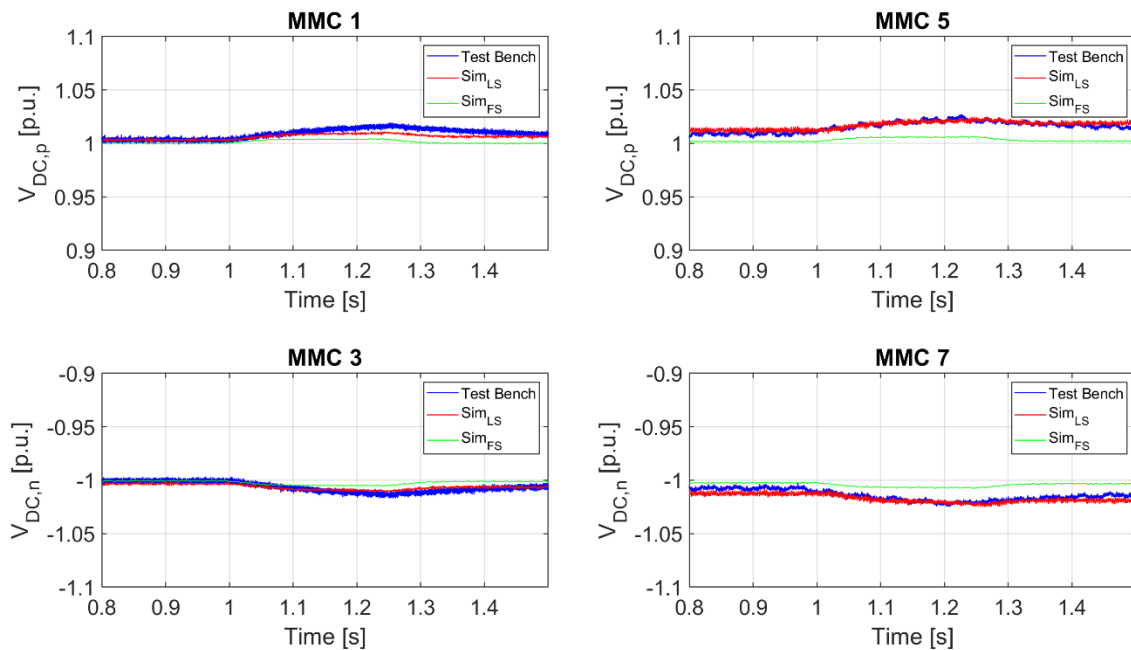


Figure 3-3: DC voltage in the bipolar network configuration for the investigated test case

Similar to the DC voltages measured in Figure 3-3, the DC voltages measured at MMC stations 6, 8 and MMC stations 2, 4 show very close match and no big difference. At MMC station 2 and MMC station 4, where at time $t = 1$ s, the active power that is transferred into the DC grid from the respective MMC stations is increased to $P = 1.0$ p.u. This leads to an increase in the DC voltage in the whole DC grid, and it can be observed at all MMC stations.

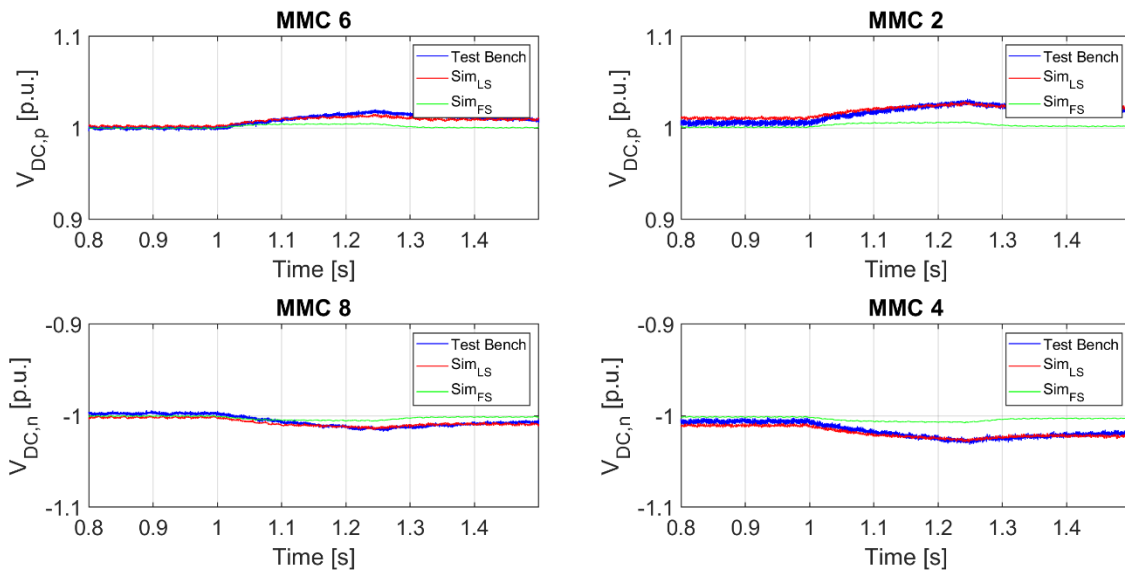


Figure 3-4: DC voltage in the bipolar network configuration for the investigated test case

Figure 3-5 shows the active power measured at MMC stations 6, 8 and MMC stations 2, 4. At MMC station 6 and 8, the active power is controlled to $P_{ref} = -0.5$ p.u. The simulated full-scale model, the simulated lab-scale model and the MMC Test Bench show no difference, as the active power is controlled to its reference value. At MMC station 2 and 4, the active power is initially controlled to $P_{ref} = 0.5$ p.u. and then at $t = 1$ s, it is increased to $P_{ref} = 1.0$ p.u. The simulated models and the MMC Test Bench show the same behaviour and no difference between them.

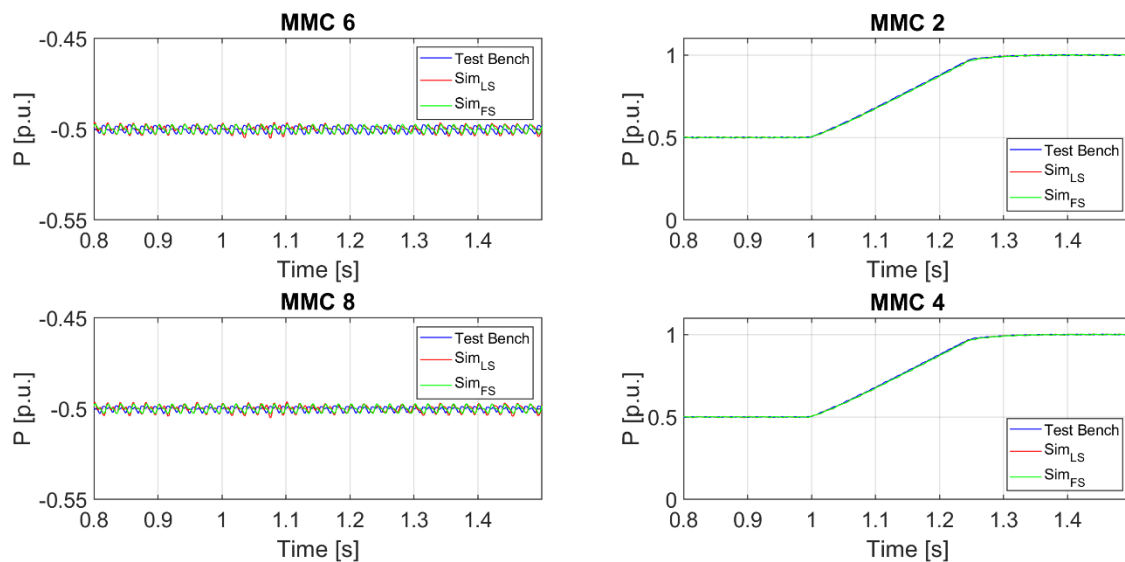


Figure 3-5: Active power in the bipolar network configuration for the investigated test case

Figure 3-6 shows the active power measured at MMC stations 1, 3 and MMC stations 5, 7. At MMC stations 5 and 7, the active power is controlled to $P_{ref} = 0.5$ p.u. and the simulated models compared to the MMC Test Bench

show no significant difference here as well. Compared to the other MMC stations, at MMC station 1 and 3, the active power of the simulated models and the MMC Test Bench show difference in their amplitudes. In comparison to the other MMC stations, at MMC station 1 and 3, the DC voltage is controlled and thus, MMC station 1 and 3 transfer the power difference that results as the difference of the power fed into the DC grid by MMC stations 5, 7 and MMC stations 2, 4. The simulated full-scale model serves as the reference signal and initially it shows an active power flow into AC grid 1 of approximately $P \approx -0.5$ p.u. The active power has initially a little higher amplitude than $P = -0.5$ p.u. since the losses of the DC lines represented by the ULM have to be taken into account. Compared to the simulated full-scale model, the active power at MMC stations 1 and 3 for the simulated lab-scale model shows a very close behaviour to the full-scale model. However, its amplitude is a little higher compared to the simulated full-scale model and this indicates that the system losses of the hardware components are higher. For the MMC Test Bench a similar pattern is observed, where the transferred active power has a higher amplitude compared to the simulated models, indicating even higher losses than the simulated lab-scale system. At time $t = 1$ s, the active power transfer at MMC station 1 and 3 changes according to the active power fed into the DC grid from MMC stations 2 and 4. The simulated models and the MMC Test Bench still show the same behaviour with the conserved amplitude difference of the active power measured at the corresponding simulated models and the MMC Test Bench.

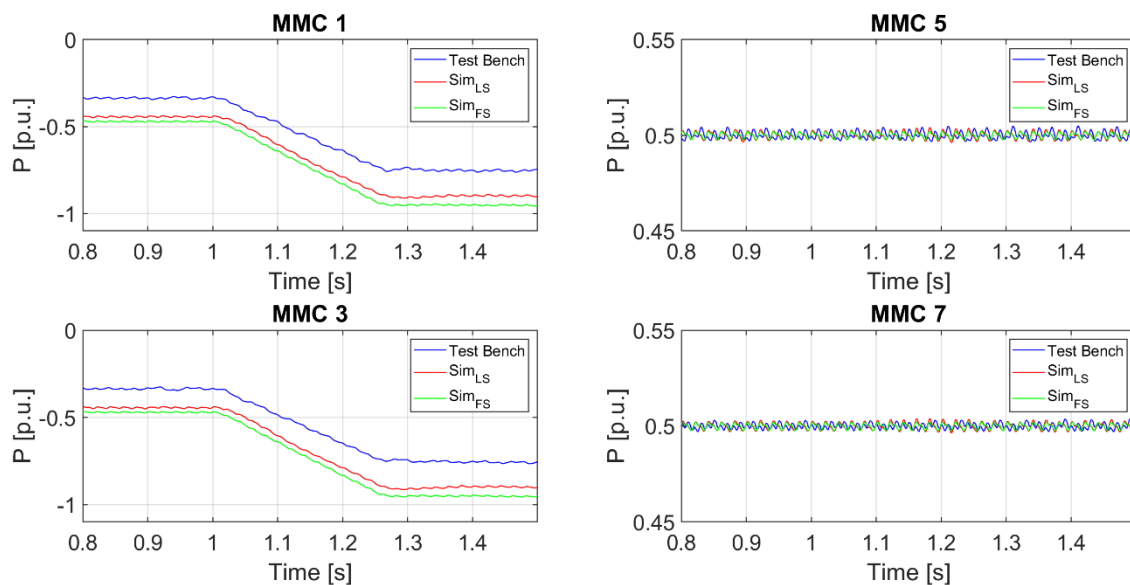


Figure 3-6: Active power in the bipolar network configuration test case

3.2.1.2 SUMMARY AND CONCLUSION

Following the demonstrations of the integration of offshore wind farms in a MTDC network consisting of symmetrical monopole configuration in deliverable D16.3, a demonstration of a bipolar MTDC configuration is the next step toward the demonstration of OWF in bipolar MTDC network configurations. In order to include OWF implementation with the MMC Test Bench in a bipolar configuration as well as to conduct fault studies regarding OWFs, a proper PHIL interface algorithm is needed to ensure a stable implementation of higher rating OWFs as well as AC faults and DC faults. However, detailed studies regarding possible proper PHIL interfaces will be

considered in future investigation, as the existing standard PHIL interface algorithms have proven to not provide the necessary stability and accuracy. In this deliverable, the MMC controls have been demonstrated with the MMC Test Bench for a 4-terminal bipolar configuration and the result comparison to the simulated full-scale models show close match of the converter control response. The differences in the amplitude between the models mainly come due to the higher system losses of the MMC Test Bench.

3.3 FAULT CLEARING IN HVDC NETWORKS

In meshed HVDC networks, fault handling is a key challenge. The fault handling needs to be reliable while providing fast separation of DC faults in order to limit the fault propagation within the transmission system as well as to protect the system's components. Considering also the surrounding AC grids, the DC faults must not endanger their stability. To achieve these goals, suitable protection concepts must be developed and thoroughly investigated, which has been a particular scope of the PROMOTiON project. The Technical Brochure 739 of Cigré divides grid protection concepts into three categories, these are:

1. Non-selective protection
2. Partially selective protection
3. Fully selective protection

A short overview of the main properties of the three categories is presented in Figure 3-7.

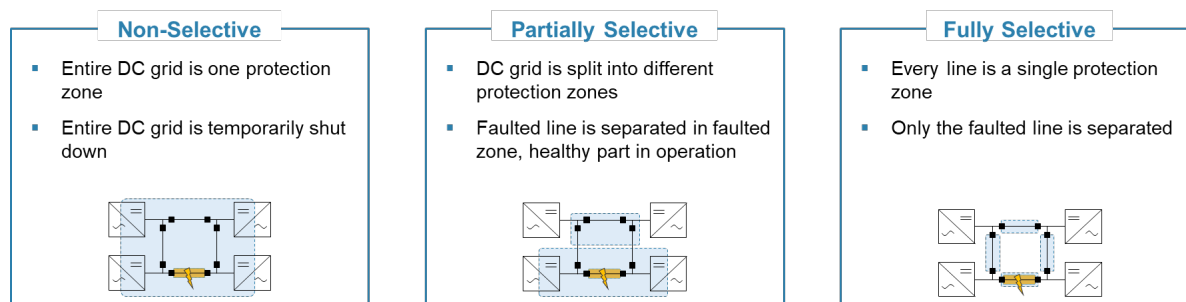


Figure 3-7: Fault Clearing Concepts

For the realisation of each of the concepts, various fault separation philosophies exist. Two promising philosophies are selected for the purpose of demonstration with the MMC Test Bench:

- Non-selective fault clearing based on fault blocking converters (cf. Chapter 3.3.1):
This concept promises reduced requirements towards the DC circuit breakers due to an active voltage and fault current control, enabling the full-bridge MMCs to enforce near-zero conditions before the DC circuit breakers are tripped (cf. Figure 3-8, left side).

- Fault separation based on fast DC circuit breakers (cf. Chapter 3.3.2):**
 This concept offers the fastest fault separation approach since it comes without the need for precedent control actions. Therefore, the DC circuit breakers are required to interrupt the full DC fault current once they are triggered (cf. Figure 3-8, right side).

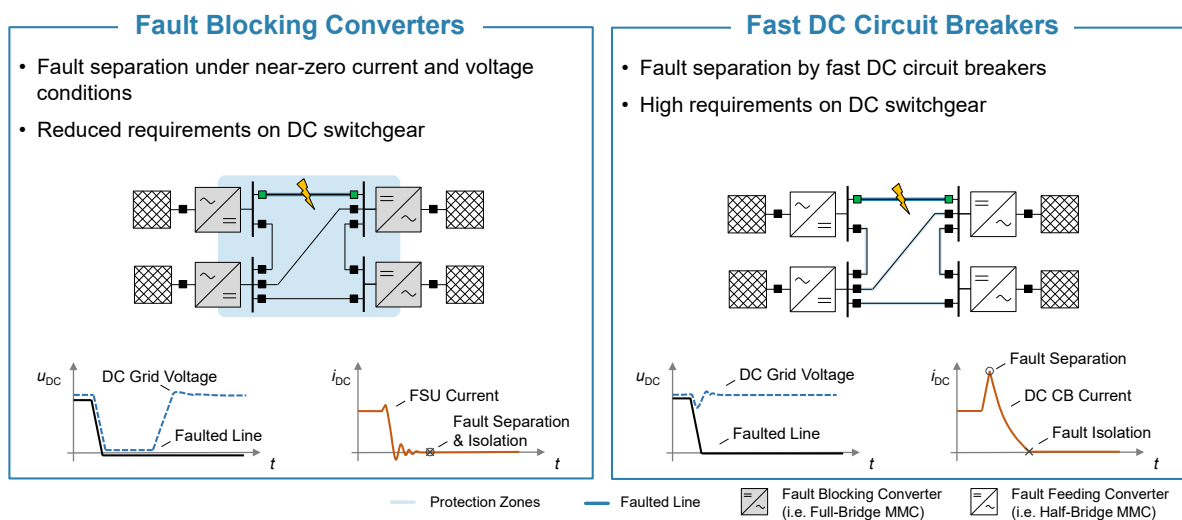


Figure 3-8: Fault Separation Philosophies

Methodology

For both demonstration cases, the Test Bench results are held against the results from equivalent offline simulation models. Through this step not only the test bench’s performance can be validated but also the confidence level of the method, described in chapter 2.2.2, is increased through the demonstrations. A high degree of similarity gives an indication that the demonstrated controls will also work in a real full-scale system, which, due to its size and the related costs, cannot be considered for laboratory demonstrators. However, the implemented controls in the test bench system and the offline simulations models are on the highest possible level and have been extensively tested to deliver the best match with a real full-scale system.

3.3.1 NON-SELECTIVE FAULT CLEARING BASED ON FB-MMC

3.3.1.1 SYSTEM SETUP AND FAULT CLEARING SEQUENCE

For this demonstration, the following two network configurations are under investigation:

- 4-terminal symmetrical monopole, analogous to the configuration developed in PROMOTiON WP2. It is shown in Figure 3-9
- Point-to-point bipolar link with dedicated metallic return, shown in Figure 3-10

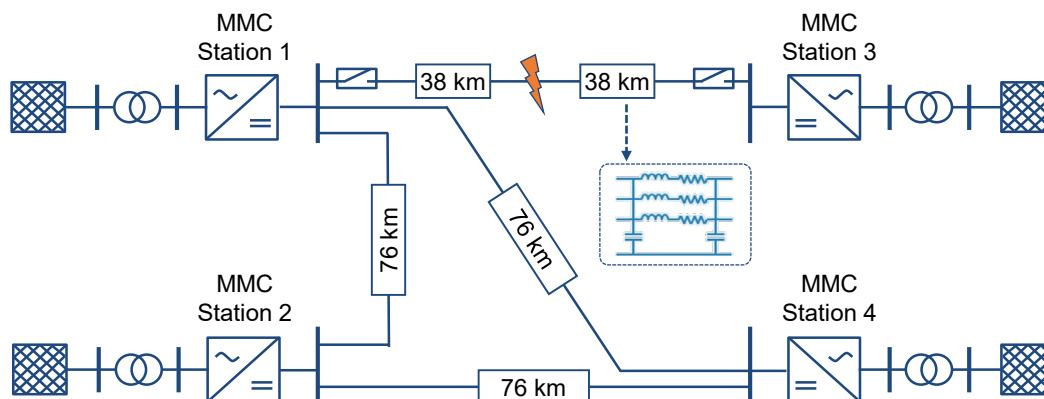


Figure 3-9: Multi-terminal grid as symmetrical monopole

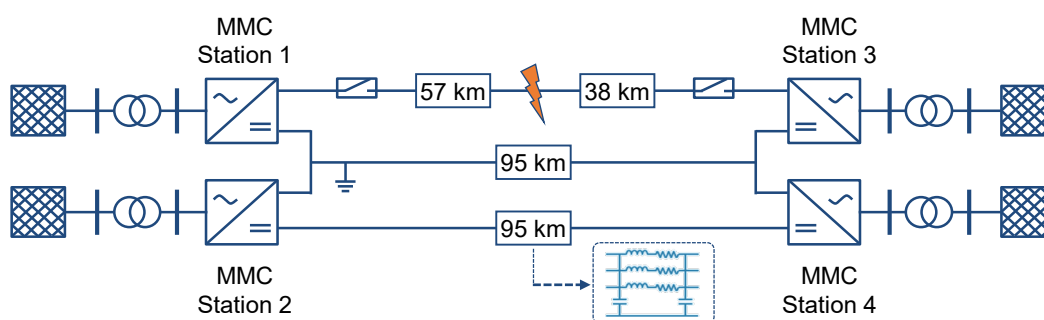


Figure 3-10: Bipolar point-to-point link with dedicated metallic return

The investigated networks are implemented in SIMULINK as simulated lab- and full-scale models. The results are compared to the MMC Test Bench implementation by an evaluation of the characteristic values in per-unit. While the lab-scale simulation and the MMC Test Bench use the Pi³-sections introduced in Chapter 2.2.1, the full-scale simulation uses a frequency dependent cable model designed in the EMT software tool PSCAD-EMTDC. The control mode and the set points of each converter are displayed in Table 3-1 and Table 3-2 respectively. The differences in the set points result from different line losses and are determined so that an equivalent DC terminal current flows at each MMC station. The reactive power control is set to zero.

Table 3-1: Converter control mode and set points for 4-terminal symmetrical monopole

MMC Station	Control Mode	Full-scale Model	Laboratory-scale Model	MMC Test Bench
MMC 1	V _{dc} Control	+ 1.00 p.u.	+ 1.00 p.u.	+ 1.00 p.u.
MMC 2	P Control	- 0.59 p.u.	- 0.62 p.u.	- 0.65 p.u.
MMC 3	P Control	+ 0.58 p.u.	+ 0.62 p.u.	+ 0.80 p.u.
MMC 4	P Control	+ 0.57 p.u.	+ 0.61 p.u.	+ 0.75 p.u.

Table 3-2: Converter control mode and set points for point-to-point bipolar link

MMC Station	Control Mode	Full-scale Model	Laboratory-scale Model	MMC Test Bench
<i>MMC 1</i>	V _{DC} Control	+ 1.00 p.u.	+ 1.00 p.u.	+ 1.00 p.u.
<i>MMC 2</i>	V _{DC} Control	+ 1.00 p.u.	+ 1.00 p.u.	+ 1.00 p.u.
<i>MMC 3</i>	P Control	+ 0.62 p.u.	+ 0.62 p.u.	+ 0.75 p.u.
<i>MMC 4</i>	P Control	+ 0.62 p.u.	+ 0.62 p.u.	+ 0.75 p.u.

The demonstration focusses on high impedance pole-to-ground faults, as these have been identified to be the most relevant and critical in terms of voltage recovery time in D4.1. Exemplarily, positive pole to ground faults between MMC 1 and MMC 3 have been chosen with a laboratory-scale resistance of 1 Ω for the multi-terminal system in symmetrical monopole configuration and 2 Ω for the bipolar point-to-point link. These resistances correspond to full-scale resistances of 12.8 Ω and 25.6 Ω respectively.

In the context of this demonstration, the fault detection and localisation is not determined by a dedicated IED. Fault detection is done using combined undervoltage and voltage derivative criteria, which is realized by a software implementation in each individual converter station. Fault localisation in the 4-terminal grid is defined manually before each test setup. However, this does not constitute a limitation, as it has already been shown in D9.4 and D4.6 how an IED can be constructed for fault detection and localisation. In the MMC Test Bench the fault separation is realised by four IGBT based DCCBs, as described in chapter 2.2.5.. The breakers are capable of interrupting the full rated current. However, the tripping command during the fault clearing sequence is only triggered below a voltage threshold of 0.025 p.u. and current threshold of 0.01 p.u. to simulate the functionality of a residual current breaker. The demonstrated fault clearing strategy is consistent to the non-selective fault clearing strategy with full-bridge MMC presented in D4.2. The flow chart of the primary protection sequence is shown in Figure 3-11. Corresponding to the fault clearing sequence described in D4.2 there is no communication between the individual converters.

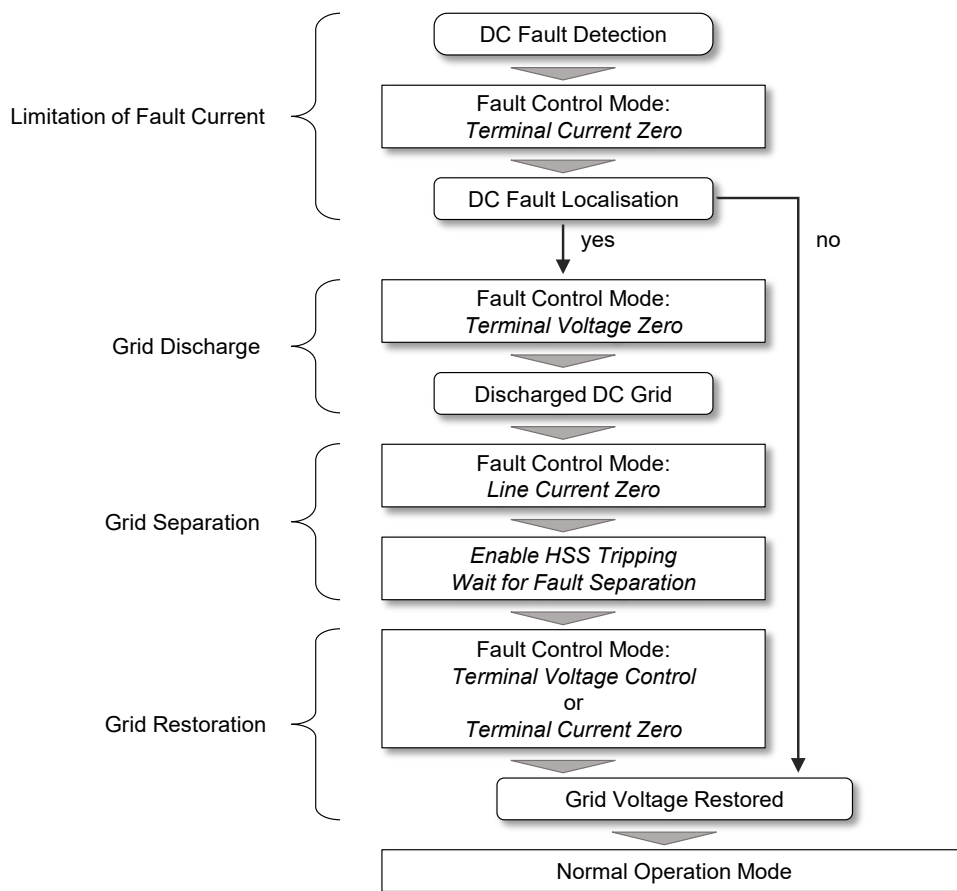


Figure 3-11: Flow chart diagram of fault clearing sequence with FB-MMC

3.3.1.2 RESULTS AND DISCUSSION - MONOPOLE

Figure 3-12 shows a comparison of the demonstration results obtained from the Test Bench and SIMULINK simulations. For each MMC the positive and negative pole voltage as well as the positive terminal current is displayed. At $t = 0$ s, the pole-to-ground fault is applied on the DC system. The DC voltage of each positive pole is pulled to ground. As a consequence, the capacitors of the respected line segments discharge and the DC current rises. Each converter detects the fault occurrence correctly and subsequently control the terminal current to zero.

Figure 3-13 shows exemplarily the voltage and current graph of the first 50 ms after fault occurrence at MMC 1 in more detail. After the terminal current has been controlled to zero at approx. 3 ms, converter 1 and 3 start to control the terminal voltage to zero. 28 ms after fault occurrence the grid is discharged. Converter 1 and 3 control the line current to zero. The respective residual current breakers are tripped after the voltage and current is below the abovementioned threshold at around $t = 30$ ms.

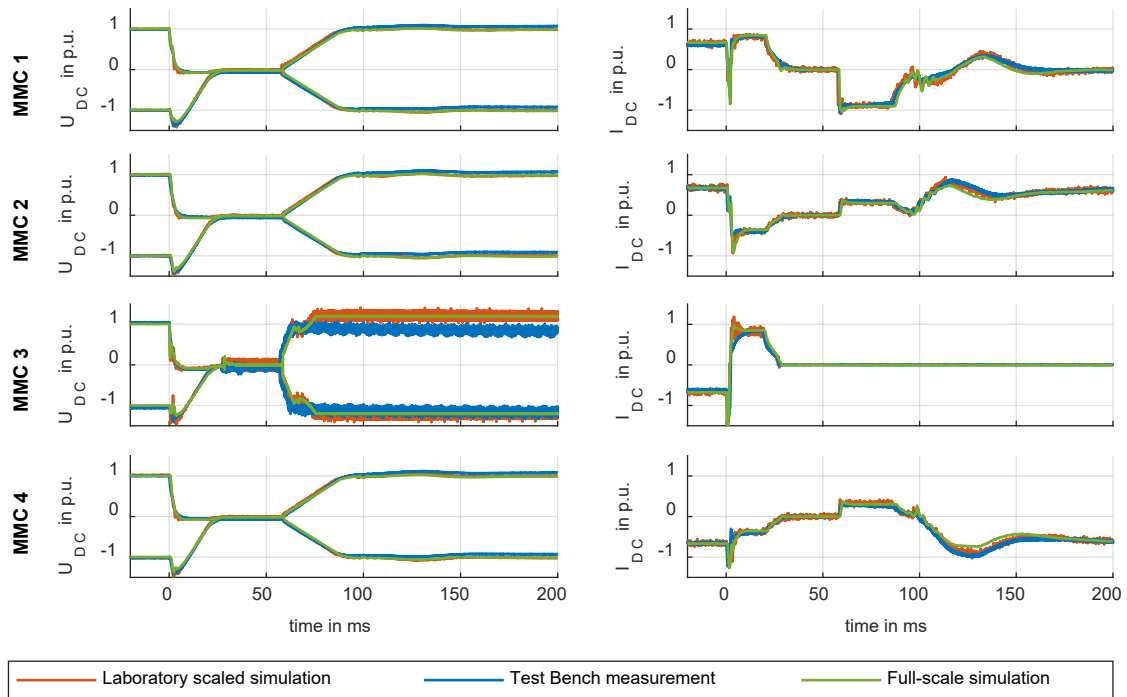


Figure 3-12: DC voltage and current of each converter after fault occurrence at $t = 0$ s in 4-terminal symmetrical monopole

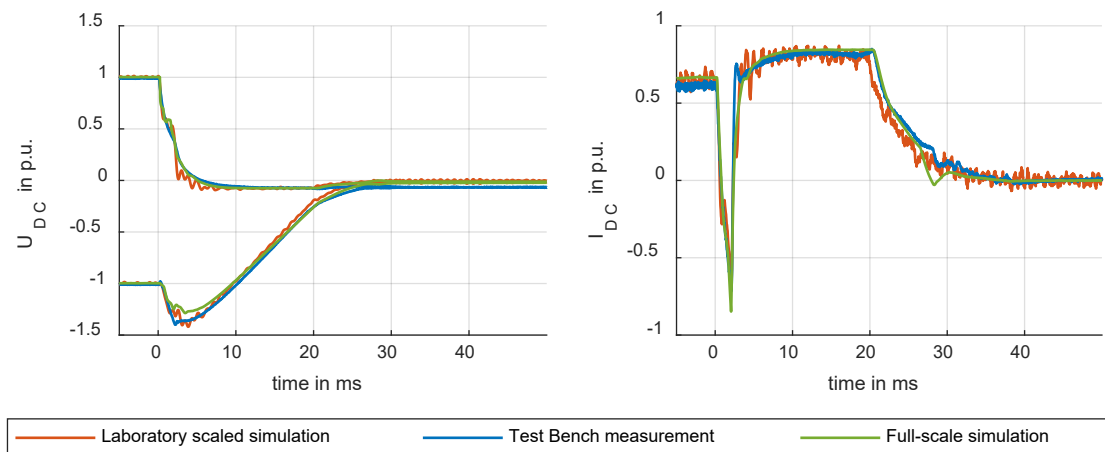


Figure 3-13: Zoomed display of DC voltage and current for MMC 1 after fault occurrence at $t = 0$ s in 4-terminal symmetrical monopole

After a safety waiting time of 10 ms converter 1 and 3 switch back to controlling the terminal current to zero and wait additional 20 ms for the restart of the grid. The safety waiting time has been chosen conservatively. It is to be expected that by setting up a communication line between the converters, the safety waiting time of 30 ms could be reduced to a few milliseconds. At $t = 60$ ms converter 1 starts to restore the grid voltage. The grid voltage is restored approx. 100 ms after fault occurrence and the power flow approx. 150 ms after fault occurrence. Converter 3 is disconnected from the grid. For this demonstration, converter 3 is set to voltage control after the

fault separation. Due to the missing reference point to ground the voltage at converter 3 oscillates. The terminal current at converter 1 adapts accordingly to the loss of power from converter 3. It can be seen, that after the voltage restoration, there is an imbalance between the Test Bench measurement and the simulation. This is explained by the fact that due to small differences in the discharge process of the grid, differences in grid voltage occur during grid separation. This imbalance can be seen in Figure 3-13 or $t > 30$ ms. Due to the missing ac-side star point reactor the imbalance is continued afterwards.

3.3.1.3 RESULTS AND DISCUSSION – BIPOLE

In Figure 3-14, a comparison between the simulation results and the Test Bench measurements for the bipolar configuration are displayed. Figure 3-14 focusses on the terminal DC voltage and current for MMC 1 and MMC 3 as the other two converters stay in operation during the fault clearing and do not interrupt the power flow. At $t = 0$ s, the pole-to-ground fault is applied on the DC system and thus the DC voltage of the positive pole is pulled to ground. However, the negative pole is not discharged into the fault.

As in the symmetrical monopole configuration, the fault occurrence is correctly detected and the terminal DC current is actively controlled to zero. After the subsequent discharge of the positive pole, the fault is separated. Due to the slightly increased measurement noise in the Test Bench and the low current threshold for the residual current breakers, the detection of falling below the set thresholds varies between $t = 10$ ms and $t = 18$ ms. However, compared to the symmetrical monopole configuration, the separation time is at least 12 ms earlier. This can be explained by the fact, that in a bipolar system, the healthy pole does not need to be discharged. After the separation, MMC stations 1 and 3 are disconnected from the grid, while MMC stations 2 and 4 continue operation.

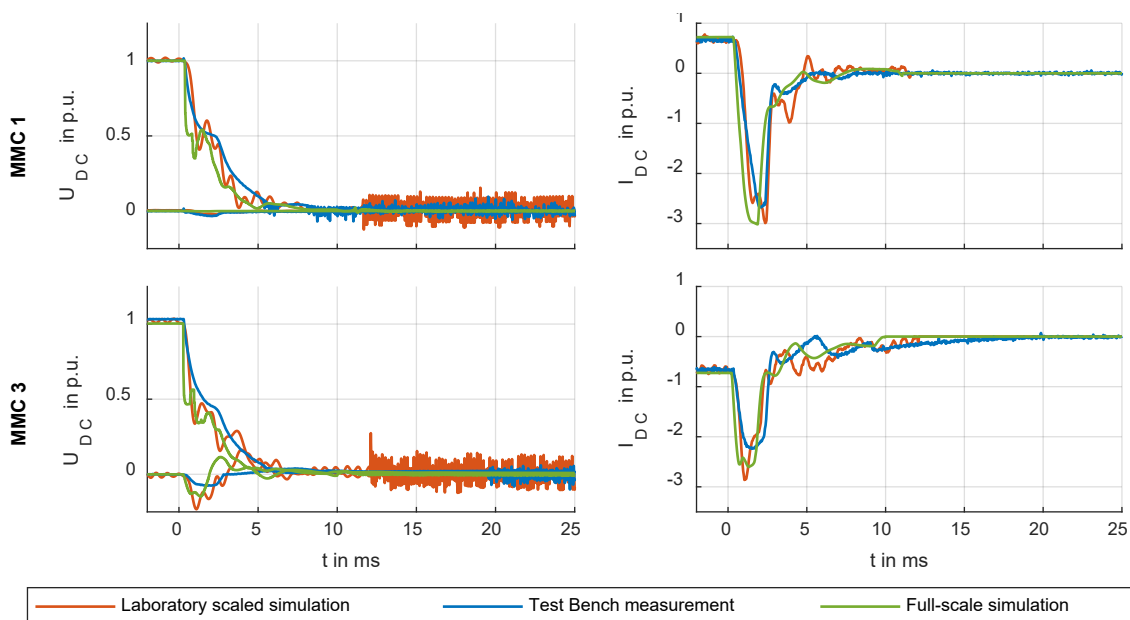


Figure 3-14: Terminal DC voltage and current after fault occurrence at $t = 0$ s in bipolar configuration

3.3.1.4 CONCLUSION

The feasibility of a non-selective fault clearing strategy using fault blocking converters and residual current breakers has been successfully demonstrated in a symmetrical monopole MTDC system and a bipolar point-to-point link. The demonstration is based on a comparison between laboratory-scaled as well as full-scaled simulations and measurements in the MMC Test Bench. The obtained results are physically plausible and show a high degree of consistency in the steady state as well as the transient time frame. Differences between the results are understood and have been discussed. The demonstration confirms the theoretical feasibility of the fault clearing strategy shown in WP4, thus further increasing the confidence that the fault clearing strategy can be successfully implemented in a multi-terminal HVDC system.

The demonstrated test configurations have a fault separation time of 30 ms in the symmetrical monopole configuration and less than 18 ms in the bipolar system. It is expected that the voltage recovery time of 100 ms in the symmetrical monopole configuration can be further reduced with a communication link between the converters.

3.3.2 DC-BYPASS

For the purpose of demonstration of a fully selective fault clearing strategy based on the application of fast DC circuit breakers, the DC-bypass concept is considered. The DC-bypass represents a promising application case for the future beneficial interconnection of similar HVDC systems without a negative on their reliability.

3.3.2.1 INTRODUCTION

The DC-bypass concept reflects the idea of a DC-side interconnection of two (or more) HVDC systems in order to achieve a (further) reduction in the overall transmission losses of HVDC power systems (cf. Figure 3-15). This is accomplished by avoiding the DC-to-AC-to-DC conversion for that power fraction that has to pass both HVDC systems as shown in Figure 3-15.

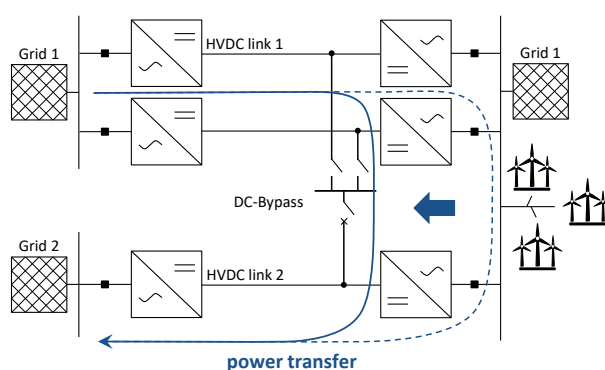


Figure 3-15: DC-bypass scheme

By the insertion of a DC-bypass link, the interconnected point-to-point HVDC systems form a common MTDC system. As single DC faults could lead to the outage of both HVDC systems within this system structure, an

extended DC system protection scheme must be thought of. A limitation of the fault mitigation within the MTDC system must be accomplished. Therefore, a selective protection strategy is required.

The demonstration of the DC-bypass concept focusses on a fully selective fault clearing strategy that is based on fast DC circuit breakers (cf. Figure 3-7 and Figure 3-15). With regard to the breakers' full fault current interruption capability, fast DC circuit breakers are able to almost instantaneously perform a fault separation once being triggered.

In the specific case of the DC-bypass demonstration, the interconnected HVDC links shall be disconnected through a fast opening of the DC circuit breakers which are therefore located on the bypass link. While the faulty HVDC link is then shut down, the other HVDC link has still the capability for a continued operation.

The following minimum requirements have to be fulfilled in order to successfully implement the DC-bypass and the according protection scheme:

1. Interoperability of HVDC systems, i.e. with regard to DC voltage levels and converter controls
2. Intelligent Electronic Device (cf. chapter 2.2.4)
3. Fast DC circuit breakers
4. Adapted control strategy assuring maintenance of the DC voltage and performing the power flow coordination

A selection of existing and/or planned point-to-point HVDC links, where the DC-bypass concept may be applicable, are given below:

- NordLink (± 525 kV) and SuedLink (± 525 kV)
- NorthConnect (± 525 kV) and the Eastern HVDC Link (± 525 kV)
- South-West Link (± 300 kV) and the Hansa PowerBridge (± 300 kV)

3.3.2.2 SYSTEM SETUP AND PROTECTION SCHEME

The simulated full-scale system setup considered in the demonstration is displayed in Figure 3-16. Its structure and electrical design are based on the South-West Link and the Hansa PowerBridge configuration as mentioned in chapter 3.3.2.1. As can be seen in the illustration, HVDC link 1 and 2 have a common AC connection point. Therefore, a DC-bypass link with fast DC circuit breakers for each pole can be additionally added. At the opponent ends, the links are connected to different non-synchronous AC grids.

While HVDC link 1 is a parallel connection of two symmetrical monopoles, HVDC link 2 represents a single symmetrical monopole system. The line lengths of both systems are 240 km and 300 km, respectively. The rated DC voltages are equally ± 300 kV. The DC-bypass link interconnects the three DC terminals of the nearby HVDC converters and comprises four disconnectors allowing a reconfiguration of HVDC link 1 when the system is not in operation. However, throughout this demonstration, all disconnectors remain closed. The MMC Test Bench is

configured based on the full-scale scheme shown in Figure 3-16. A detailed overview is of the final setup is given in Figure 3-17.

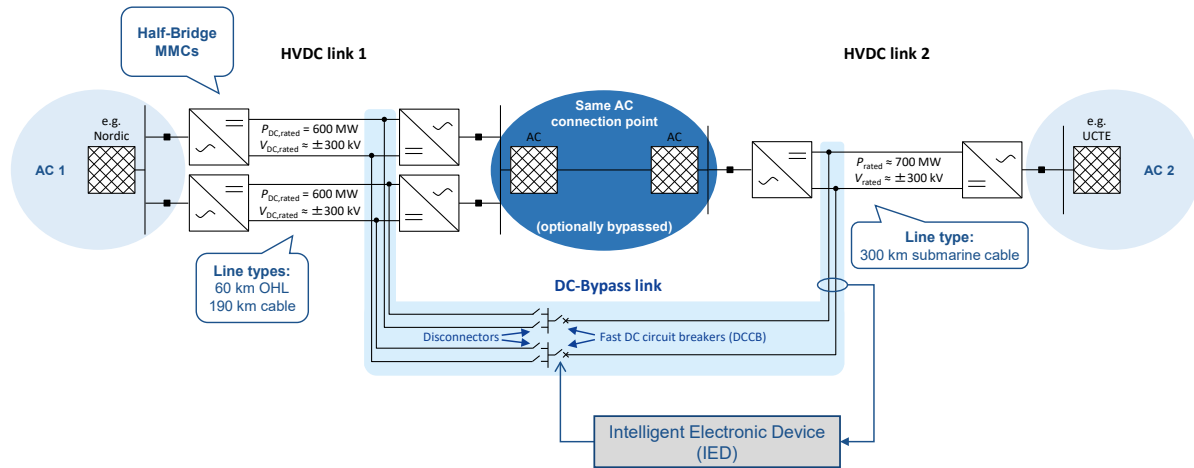


Figure 3-16: Principle System Scheme (full-scale system)

As displayed in Figure 3-17, there is no explicit DC-bypass line representation considered in the Test Bench setup. This is, because the bypass's line length is short in comparison with the rest of the transmission system and the influence of an electrical line of the DC-bypass link can be assumed to be negligible. However, a series DC inductor $L_{DC} = 5 \text{ mH}$ per pole is added to the bypass in order to limit the initial fault propagation between HVDC link 1 and HVDC link 2.

As part of the introduced methodology (cf. chapter 3.3), a lab-scaled offline simulation model is prepared in order to offer a reference for the demonstration results. A brief overview of the offline simulation model is given in Figure 3-18, which also shows the hardware components used in the corresponding laboratory setup. Furthermore, the control modes (power or voltage control) as well as the respective operation points are indicated for each converter. These settings are applied to both setups, the Test Bench and the simulation model, respectively.

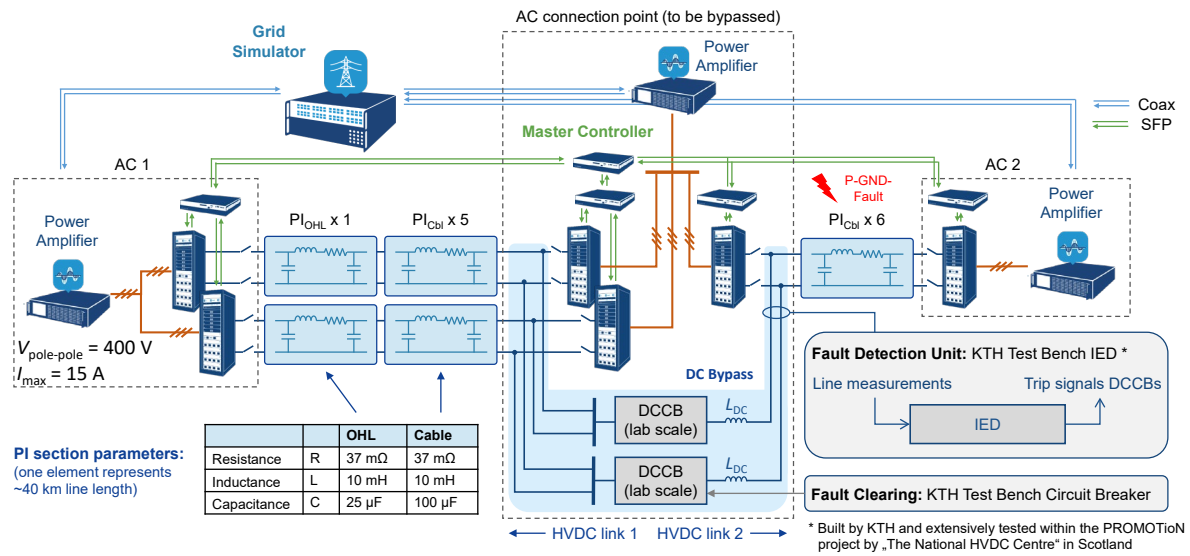


Figure 3-17: Laboratory Setup

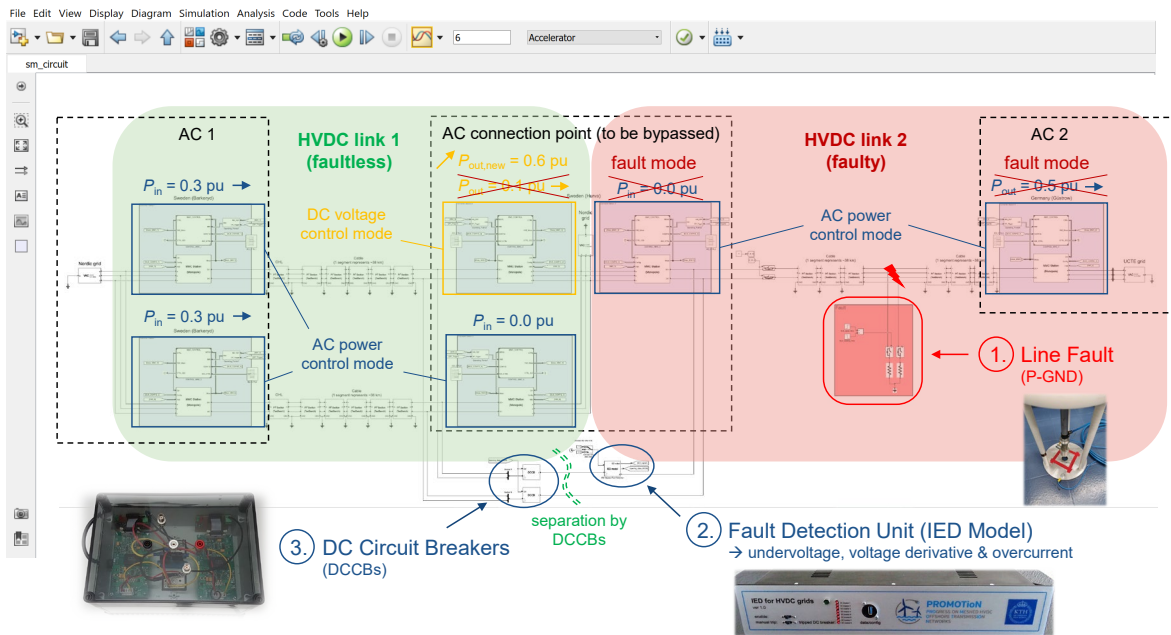


Figure 3-18: Offline Simulation Model in MATLAB Simulink

For the purpose of the demonstration, a severe fault event is considered. A metallic pole-to-ground¹ fault is chosen and positioned in the middle of HVDC link 2. The fault is triggered after the respective system, laboratory setup or offline simulation, has reached steady state and remained in stable operation for some time. The implemented protection scheme is as introduced earlier the fast² separation of HVDC link 1 and 2, so that the faultless HVDC

¹ Due to the symmetrical operation mode of the monopoles, the positive line (i.e. positive pole) is chosen without the loss of generality.

² A few milliseconds

link can remain in operation without the need of a restart. However, to match the resulting power imbalance it has to adopt a new operation point.

As indicated in Figure 3-18, the fault clearing strategy demonstration is divided into three main steps:

1. Applying the DC line fault (via a mechanical switch)
2. Detecting the DC line fault (via the IED)
3. Fault separation and power flow coordination (via the fast DC circuit breakers and control systems)

While the IED and the DC circuit breakers are comparatively simple components when they are implemented in Simulink, real hardware components require higher efforts in their design: The development of the IED and the IGBT-based DC circuit breakers was conducted by the KTH Stockholm and subsequent tests were conducted by The National HVDC Centre Scotland and the KU Leuven within PROMOTioN. The IED offers various algorithms to be individually parameterized for the real-time fault detection (cf. chapter 2.2.4). For the simplicity of the demonstration, a reduced set of algorithms is considered for the fault detection: the voltage derivative, the undervoltage and the overcurrent criteria are activated (cf. Figure 3-19). The derivative functions provide only an additional information to detect the occurrence of a fault and are not further analysed for any fault localisation. Measurements are taken at the positive pole of the DC-bypass as these are sufficient for this demonstration case (cf. Figure 3-16 - Figure 3-18).



Figure 3-19: Fault Detection Algorithms offered by the IED of the KTH Stockholm

3.3.2.3 RESULTS AND DISCUSSION

Figure 3-20 and Figure 3-21 display the results obtained from the conducted fault clearing sequence. At $t = 0$ s, the pole-to-ground fault is initiated. The DC pole voltage at the fault location is pulled down to zero as a result of the instantaneous discharge of the DC line. The voltage drop subsequently propagates as a steep travelling wave through the MTDC line system. In the consequence, the DC current along the affected MTDC line rises. When the changes reach the measurement units, the IED can safely detect the contingency based on pre-set threshold values. After a very short response time, a trip signal is sent to the fast DC circuit breakers which open. The interconnected HVDC links 1 and 2 become separated. Therefore, the fault cannot further propagate into the

healthy HVDC link 1. The short overall operation time of the DC protection system lets only slight voltage drops and current rises through reaching the MMC terminals of HVDC link 1 (cf. Figure 3-20).

Right after the fault has been cleared, a positive power imbalance of +0.5 p.u. results for the system due to the unchanged power setpoints of the power controlling MMCs (cf. Figure 3-18). Thus, the DC link voltage in the entire system begins to rise since the stray capacitances of the respective power lines become quickly charged. In order to balance out this disturbance, the voltage controlling MMC that is located in HVDC system 1 must increase its power export. This increase in exchanged power translates into a proportional rise of the current of the voltage controlling MMC (cf. Figure 3-20 and Figure 3-21, right), achieving a reversal of the rising voltage back to nominal after a few hundreds of milliseconds. Ascertaining the new steady state, the applicability of the fault separation via fast DC circuit breakers for a selective protection of the DC-bypass is successfully confirmed.

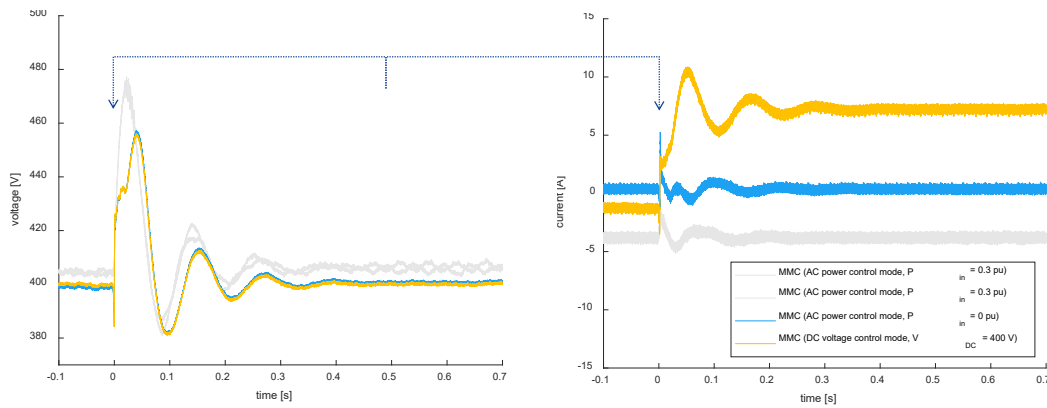


Figure 3-20: DC Voltages and Currents during Fault Clearance in the Faultless System (Laboratory Measurements)

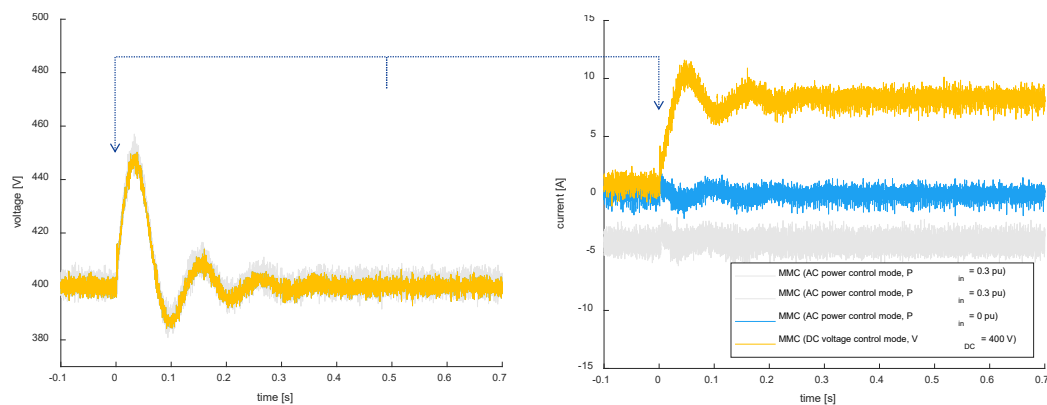


Figure 3-21: DC Voltages and Currents during Fault Clearance in the Faultless System (Offline Simulation)

Comparing the results obtained from the successful laboratory demonstration (Figure 3-20) with the results from the corresponding offline simulation (Figure 3-21), the very similar characteristics of the displayed curves become evident. However, also a few differences are observed, requiring some further discussion:

- Differences regarding steady state current of the voltage controlling MMC:
The voltage controlling MMC has to compensate the line losses of the entire DC transmission system. Since connection cables in the laboratory setup, e.g. connecting the pi sections with each other lead to a not negligible increase of the losses the operational current changes. As can be seen in Figure 3-20, the voltage controlling MMC has to inject power (recognizable by the negative current), despite an expected net export power of 0.1 p.u (if line losses in the MTDC grid could be neglected).
- Higher amount of noise in the data of the offline simulation model:
The sampling rate used for the evaluation of the internal converter quantities differs for both setup types, i.e. $T_{\text{sampling,simulation}} = 40 \mu\text{s}$ for the simulated lab-scaled model on one hand, and on the other hand, the MMC Test Bench utilizes hardware components, where the firing signals are provided by the FPGA of the corresponding real-time simulator with a time step of $T_{\text{sampling,Test-Bench}} = 5 \text{ ns}$. This results in a noisier output for the simulated lab-scale model.
- Initial voltage peaks have differing amplitudes:
For the offline simulation model, more accurate line models are used. At the time of the demonstration, only a part of the original PI sections in the laboratory environment had been fully upgraded to PI³ sections. Therefore, the little mismatch in the results is expected to be caused by the resulting differences between the laboratory and the offline simulation model, which will be confirmed in further experiments.

3.3.2.4 SUMMARY AND CONCLUSION

The applicability of a fully selective protection philosophy in a MTDC system using fast DC circuit breakers has been successfully demonstrated in two different approaches, a lab-scaled Test Bench system with real hardware components as well as a corresponding offline simulation model in MATLAB Simulink. As a basis for the demonstration, the DC-bypass concept has been chosen and has been applied to a realistic HVDC system configuration exemplary based on the South-West Link and the Hansa PowerBridge. The obtained demonstration results were understood and probable causes for identified deviations have been discussed. Overall, a high degree of consistency between both investigated approaches could be shown, proving not only that the demonstrated concepts work in reality but also indicating that the results may be very similar for a full-scale system.

3.4 FREQUENCY SUPPORT VIA MTDC NETWORKS

3.4.1 INTRODUCTION

Due to the increasing share of converter-based generation and less synchronous generation the system inertia decreases and therefore the rate of change of frequency increases in case of power imbalances. In case of point-to-point HVDC connections (between two asynchronous ac systems), the technical feasibility as well as regulatory

compliances (e.g. grid code requirements) related to frequency support have been widely investigated. Hence, frequency support provided by HVDC links can be regarded as a feasible ancillary service. However, when it comes to HVDC grid connections, providing frequency support to AC systems still merits investigation.

In the PROMOTiON project, the technical features, challenges, and solutions regarding frequency support from HVDC grids are investigated through analytical and numerical (digital simulations) approaches. In this chapter, the communication-less frequency support between asynchronous AC systems being investigated in Deliverable 2.3 is tested on the MMC Test Bench [12]. The applied MMC control system is the same as described in Chapter 2.2. The HVDC point to point connection interconnects different AC systems.

3.4.2 SYSTEM AND CONTROL SETUP

In this chapter the communication-less frequency support control presented in Deliverable 2.3 is summarized and an enhanced control is motivated and described. In Work Package 16 only the unidirectional frequency support has been investigated. To verify the functionality of the communication less frequency support control, a point to point connection in the EMT time-domain simulation environment HYPERSIM has been set up. The two synchronous AC systems are each represented by an IEEE 39 bus case.

The communication less frequency support control uses the dc voltage to communicate the demand of frequency containment reserves at the dc voltage controlling converter to the other converters of the dc system. In case of a demand of frequency containment reserves at an active power controlling converter the dc voltage controlling converter obtains the power balance of the dc system. The demand of frequency containment reserves is determined at each converter by measuring the ac grid frequency.

The control droop of the dc voltage controlling converters is shown in Figure 3-22. A detailed description including the formulas of the control droop at dc voltage controlling converters can be found in D2.3.

In case of frequency imbalances at the dc voltage controlling converter the control operates as follows:

- The frequency is measured locally at the converter terminal
- The frequency dead band (e.g. 10 mHz) and frequency maxima and minima can be set
- The dc voltage reference is changed to communicate the support demand to the active power controlling converter, in addition, the maximum dc voltage change can be set (e.g. to 0.1 pu) to avoid triggering of converter voltage protection.
- In addition, a rate limiter is implemented in WP16 to smooth the reaction of the MMC converter. This is only necessary in case of strong HVDC grids in combination with weak ac grids. For instance, when comparing the MMC rating of 1265 MVA to the 6 GW generation of the IEEE 39 bus case. In this case several power imbalances has been tested and a fixed rate limit is chosen which ensures an acceptable reference steepness.

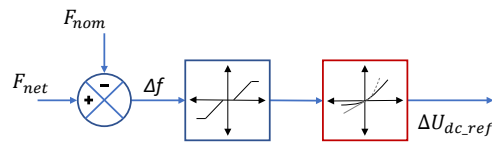


Figure 3-22: Control droop at dc voltage controlling converter

The control droop at active power controlling converters is shown in Figure 3-23. A detailed description including the formulas of the control droop at active power controlling converters can be found in D2.3.

In case of frequency imbalances at the active power controlling converter:

- The frequency is measured locally at the converter terminal
- The frequency dead band (e.g. 10mHz) and frequency maxima and minima can be set
- The maximum setpoint change of the active power reference by control can be defined
- In case of a fault at the dc voltage controlling converter, the dc voltage is used as communication medium and will therefore change. The active power controlling converter will sense this change and therefore adapt its active power reference.
- DC voltage deadband of ± 0.01 pu
- In addition, a rate limiter is implemented in WP16 to smooth the reaction of the MMC converter. This is only necessary in case of strong HVDC grids in combination with weak AC grids. For instance, when comparing the MMC rating of 1265 MVA to the 6 GW generation of the IEEE 39 bus case. In this case several power imbalances has been tested and a fixed rate limit is chosen which ensures an acceptable reference steepness.

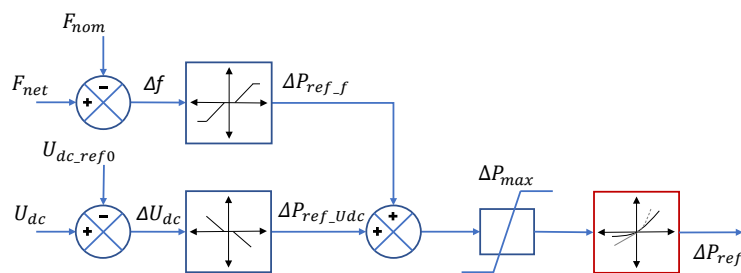


Figure 3-23: Control droop at active power controlling converter

The investigated point to point connection connects the two asynchronous systems grid A and grid B as shown in Figure 3-24. The HVDC connection injects 632 MW into grid A. The specifications of each MMC are shown in Table 2-1, Table 2-2 and Table 2-3.

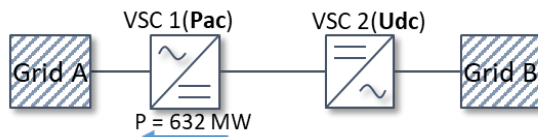


Figure 3-24: Point to Point HVDC connection between two synchronous grids A and B

Grid A and Grid B is each represented by the IEEE 39 bus system as represented in Figure 3-25. The point of connection to the HVDC system in both grids is bus 2.

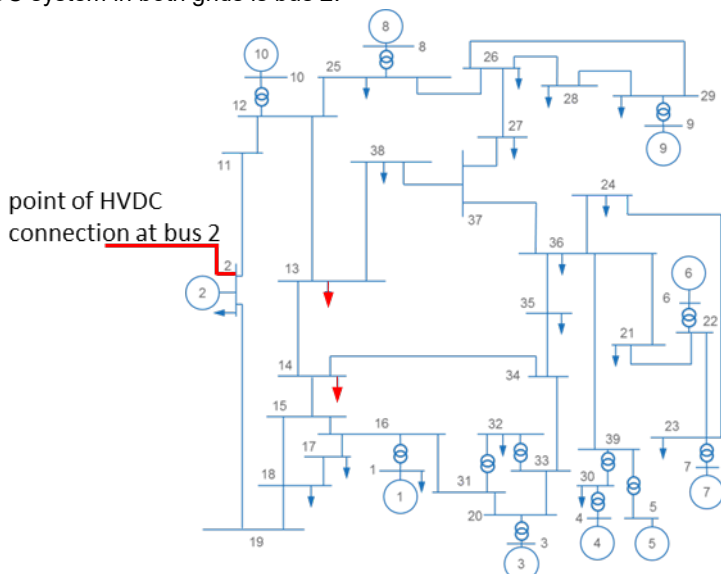


Figure 3-25: IEEE 39 bus system with HVDC connection point at bus 2 and changed loads at bus 13&14 [13–15]

The loads at bus 13 in grid A and at bus 13 and 14 in grid B have been changed in order to set the active power transport from grid B to grid A of 632 MW. Table 3-3 lists the new load values for the changed loads.

Table 3-3: IEEE 39 bus changed load values to achieve the specified loadflow between grid A and B

Grid A	P [MW]
Load Bus 13	904
Grid B	P [MW]
Load Bus 13	121.4
Load Bus 14	0

3.4.3 COMMUNICATION-LESS FREQUENCY SUPPORT

Two fault scenarios are investigated to show that the implemented unidirectional frequency support control is not interacting with any converter protection scheme and gives comparable behaviour to the investigations made in the frame of D2.3 using simplified average value models.

In the first scenario, the synchronous machine number 10 of grid A is disconnected in order to trigger an active power demand in grid A. As a result, the control droop at the power controlling converter connected to grid A

changes the active power reference in order to support grid A. In the second scenario, the synchronous machine number 10 of grid B is disconnected in order to trigger an active power demand in grid B. As a result, the control droop at the dc voltage controlling converter connected to grid B changes the dc voltage reference. This communicates the active power demand to the active power controlling converter.

SCENARIO 1

In Figure 3-26 the fault location of scenario 1 is highlighted.

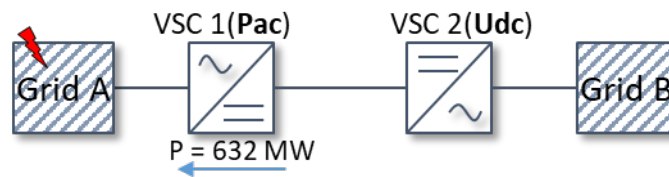


Figure 3-26: Point to Point HVDC connection between two synchronous grids A and B with synchronous generator #10 disconnection in grid A

At $t = 2$ s, synchronous generator #10 (250 MW) is disconnected in Grid A. Figure 3-27 shows the frequency and the sum of the synchronous generator active power injection of each grid after the outage with and without activated frequency support.

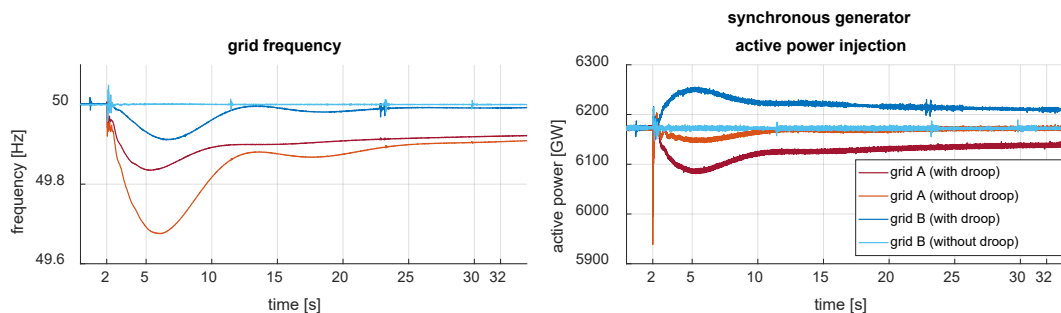


Figure 3-27: Frequency and total generator power of grid A and B after outage of synchronous machine #10 (250 MW) in grid A at $t = 2$ s with and without activated frequency support

Without activated frequency support control, the frequency and the injected active power of the synchronous generators in grid B is not affected by the generator disconnection in grid A. In grid A the frequency drops within 4 s to its minimum of 49.68 Hz and stabilizes due to the activation of frequency containment reserves in grid B at 49.9 Hz.

When the frequency support control is activated, grid B is supporting grid A. In this case the frequency in grid A drops within 3.2 s to its minimum of 49.83 Hz, the frequency in grid B drops within 4.7 s to its minimum of 49.91 Hz. Due to the activation of frequency containment reserves in grid A and grid B, the frequency in grid A stabilizes at 49.92 Hz and the frequency in grid B stabilizes at 49.99 Hz.

Figure 3-28 shows the active power and dc voltage of both MMC converters after the outage with and without activated frequency support.

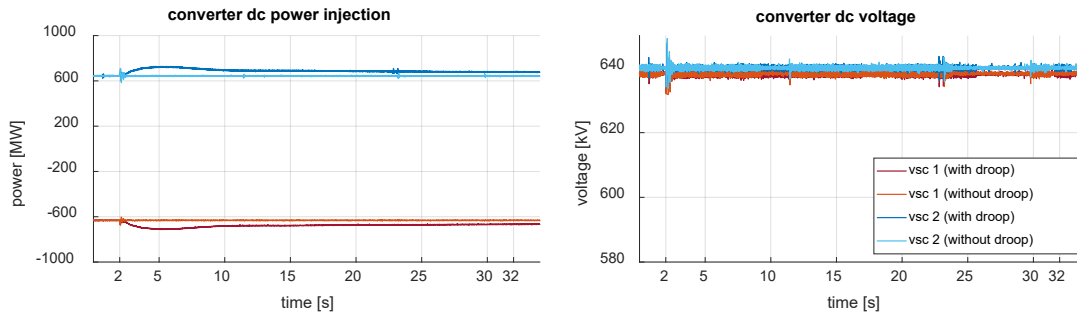


Figure 3-28: Active power and dc voltage of both MMC converters after outage of synchronous machine #10 (250MW) in grid A at t = 2 s with and without activated frequency support

Without activated frequency support control, the transmitted active power and the dc system voltages are not affected by the generator outage.

When the frequency support control is activated, the active power controlling MMC converter VSC 1 increases its active power injection into the ac system by a maximum of 78 MW at t = 5.2 s. During the fault, the dc voltage controlling MMC converter VSC 2 keeps the dc voltage constant.

SCENARIO 2

In scenario 2 the synchronous machine #10 in grid B is disconnected at t = 2 s. In Figure 3-29 the fault location of scenario 1 is highlighted.

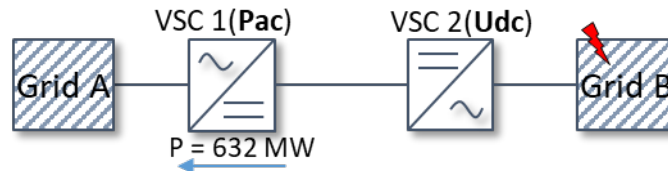


Figure 3-29: Point to point HVDC connection between two synchronous grids A and B with synchronous generator #10 disconnection in grid B

At t = 2 s, synchronous generator #10 (250 MW) is disconnected in Grid B. Figure 3-30 shows the frequency and the sum of the synchronous generator active power injection of each grid after the outage with and without activated frequency support.

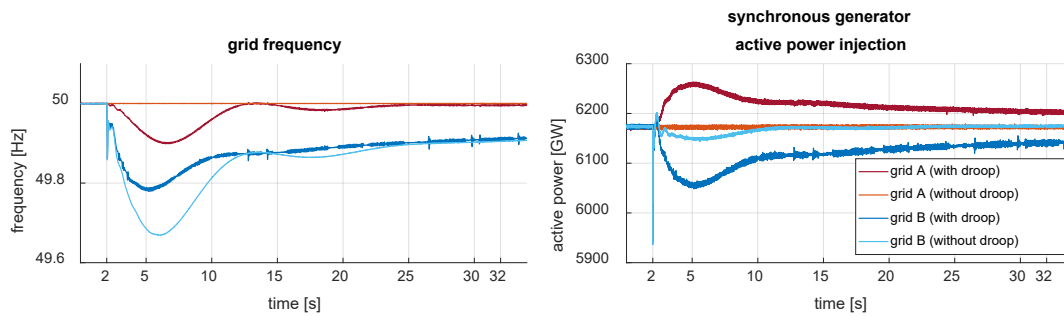


Figure 3-30: Frequency and total generator power of grid A and B after outage of synchronous machine #10 (250 MW) in grid B at t = 2 s with and without activated frequency support

Without activated frequency support control, the frequency and the injected active power of the synchronous generators in grid A is not affected by the generator disconnection in grid B. In grid B the frequency drops within 4 s to its minimum of 49.68 Hz and stabilizes due to the activation of frequency containment reserves in grid A at 49.9 Hz.

When the frequency support control is activated, grid A is supporting grid B. In this case the frequency in grid B drops within 3.2 s to its minimum of 49.78 Hz, the frequency in grid A drops within 4.7 s to its minimum of 49.9 Hz. Due to the activation of frequency containment reserves in grid A and grid B, the frequency in grid B stabilizes at 49.91 Hz and the frequency in grid A stabilizes at 50 Hz.

Figure 3-31 shows the active power and dc voltage of both MMC converters after the outage with and without activated frequency support.

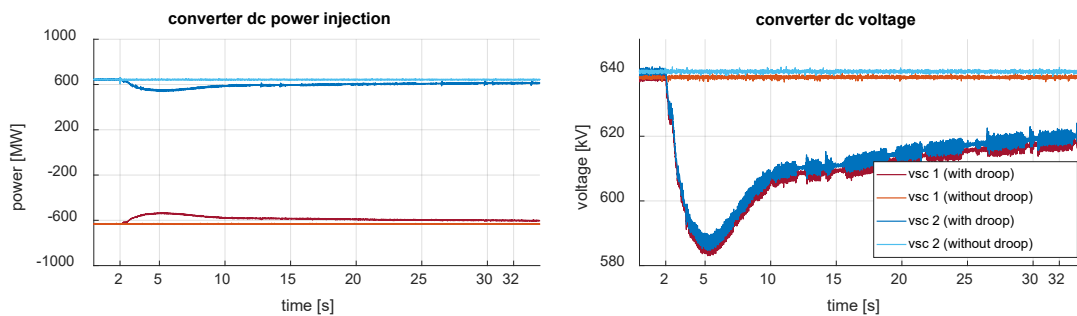


Figure 3-31: Active power and dc voltage of both MMC converters after outage of synchronous machine #10 (250MW) in grid B at t=2s with and without activated frequency support

Without activated frequency support control, the transmitted active power and the dc system voltages are not affected by the generator outage.

When the frequency support control is activated, the dc voltage controlling MMC converter VSC 2 reduces the dc voltage in order to communicate the active power demand to the active power controlling MMC converter VSC 1 to a minimum of 585 kV at 5.2 s. Due to the changing dc voltage the active power controlling MMC VSC 1 is reducing the loadflow from grid B to grid A by a maximum of 100 MW at t = 5.2 s.

3.4.4 CONCLUSION

The focus of the investigations made in the frame of WP 16 was to examine, whether the communication less unidirectional frequency support control interacts unintended with any control part of the MMC control. The MMC control, which has been developed for the converter control of the MMC Test Bench has been extended by the unidirectional communication less frequency support.

In both considered scenarios, the expected unidirectional frequency support could be examined. No internal converter protection as over current protection or over voltage protection has been triggered. Therefore, the investigations using simplified average value models in the frame of WP 2 in the context of unidirectional communication less frequency support can be confirmed.

Using a setup as the MMC Test Bench, (commercial) external frequency support controllers can be tested regarding their functionality and interaction with MMC controls.



3.5 FAULT-RIDE-THROUGH AND FREQUENCY RESPONSE TESTS IN MMC CHIL TEST BENCH

Using the MMC CHIL test bench as described in section 2.4, two categories of performance tests were conducted for the DC connection case using the test set-up as shown Figure 2-15 :

1. Fault-ride-through (FRT) for a three-phase-to-ground shore-circuit fault at the high voltage terminal of the onshore station.
2. Frequency response for sudden frequency changes at one of the connected AC grids.

3.5.1 FAULT-RIDE-THROUGH TEST

The FRT test was conducted using the following grid configuration, where a three-phase-to-ground fault happened at the high voltage AC bus of the onshore converter stations. The fault lasted 200 milliseconds.

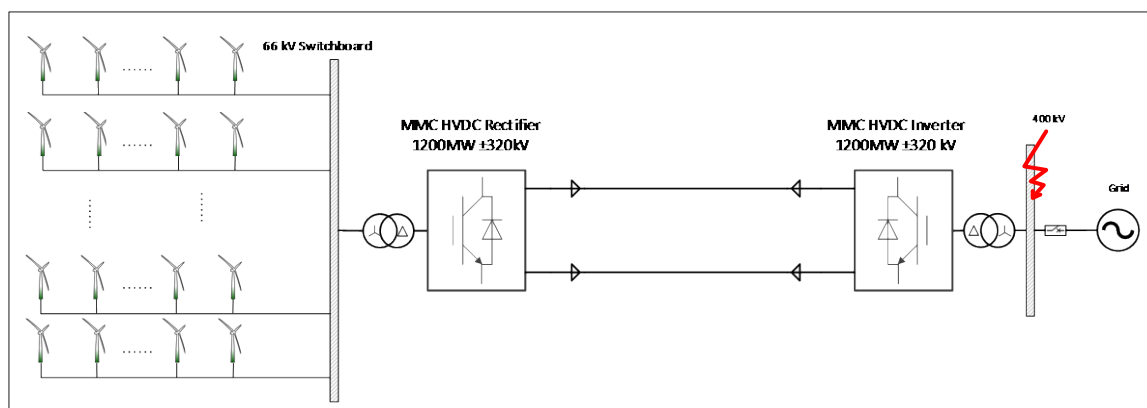


Figure 3-32 Single line diagram of FRT test for the DC connection offshore wind power plant

The results of the FRT test, as recorded from the MMC controller replicas, are shown in Figure 3-33 and Figure 3-34, respectively.

During the fault period, the AC voltage on the onshore converter dropped to almost zero and the active power also reduced to a very low level. In the meantime, the active power export from the offshore wind power plant was kept at its pre-fault level (1200 MW). The excessive power caused the DC link to be charged and DC voltage increased rapidly, until the DC chopper engaged and helped to keep the DC voltage from rising too much. After about 200 milliseconds, the fault was cleared, and the system resumed its normal operation. The system demonstrated that it can ride through the most severe fault in the AC grid.

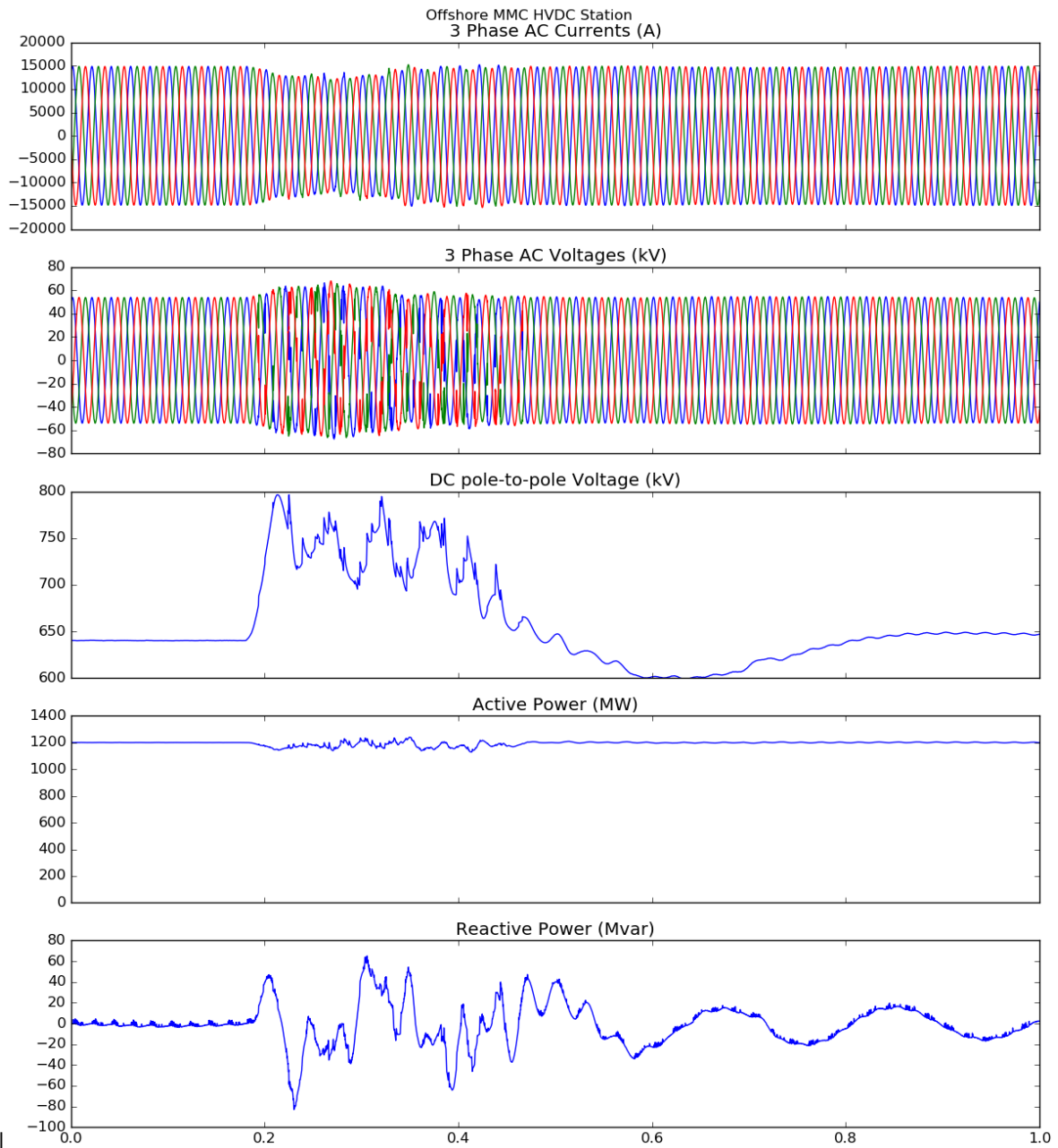


Figure 3-33 FRT test results of offshore converter station following a 200 ms 3phase-to-ground failure at the high voltage AC bus of the onshore converter station.

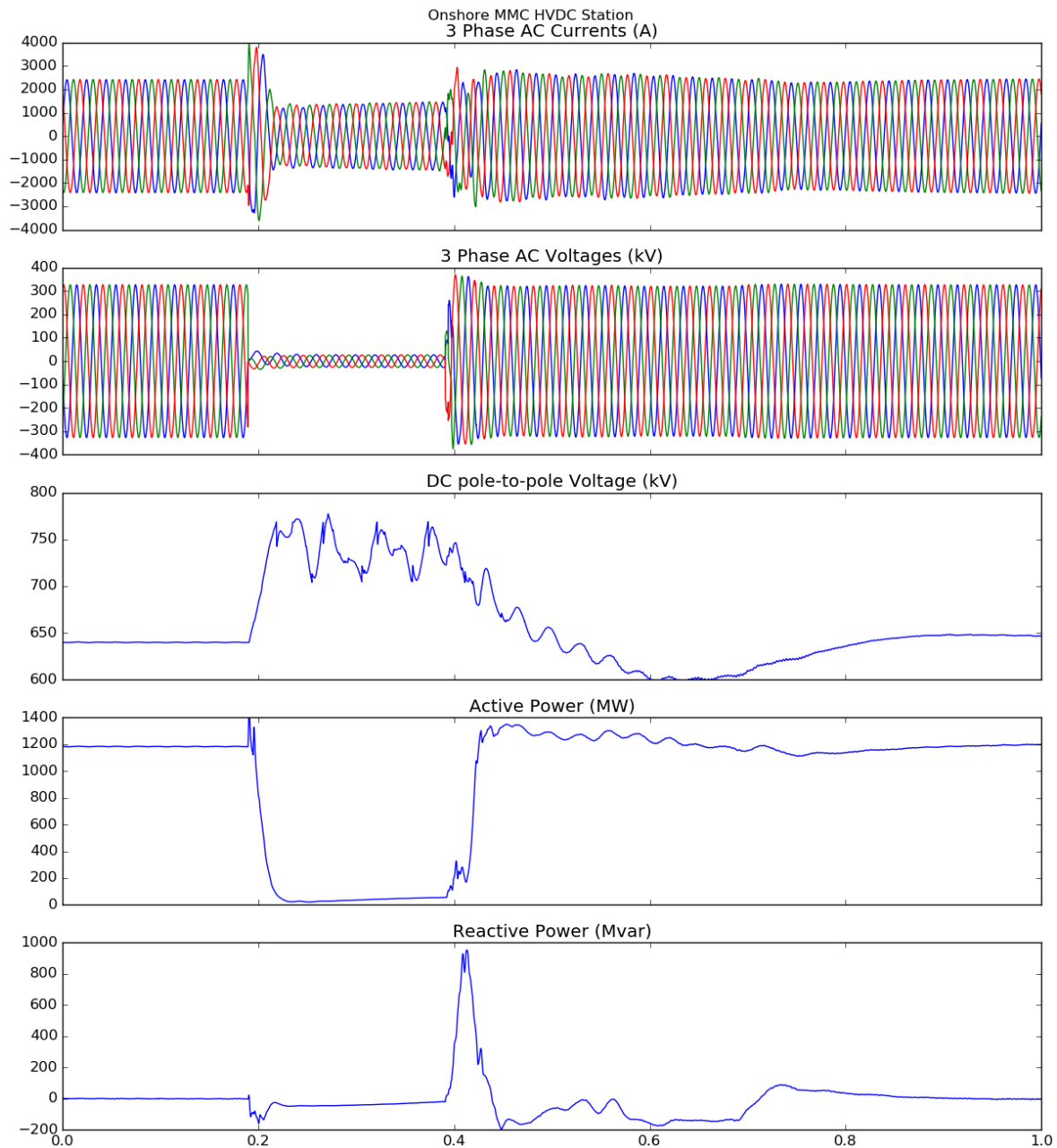


Figure 3-34 FRT test results of the onshore converter station, following a 200 ms 3phase-to-ground failure at the high voltage AC bus of the onshore converter station.

3.5.2 FREQUENCY RESPONSE

The frequency response tests were carried out using the grid topology as shown in Figure 3-35, where two onshore grids are connected through an HVDC interconnector with the rating of 1200 MW @ ± 320 kV. In the initial condition, the power flow is from the left to the right with a loading of 1000 MW, i.e. the converter to the left operates in rectifier mode whereas the one to the right in inverter mode.

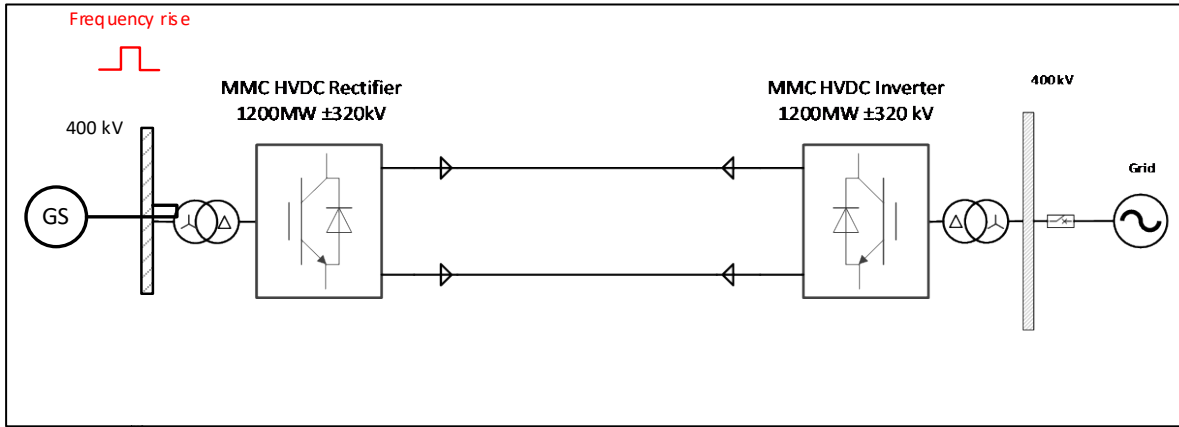


Figure 3-35 Single line diagram of the frequency response test system

At 1.8 second, a synthetic signal was injected into the frequency measurement (Phase Locking Loop, PLL) of the rectifier (left), which experienced a square wave rise of its frequency measurement. The magnitude of the rise was 1% (0.5 Hz) and lasted 500 millisecond. The results are shown in Figure 3-36, where we plotted various variables of the rectifier. With measure frequency rise, the rectifier acted to increase the power extraction from AC grid on the left in order to balance the active power such that the frequency can restore to normal value (50 Hz).

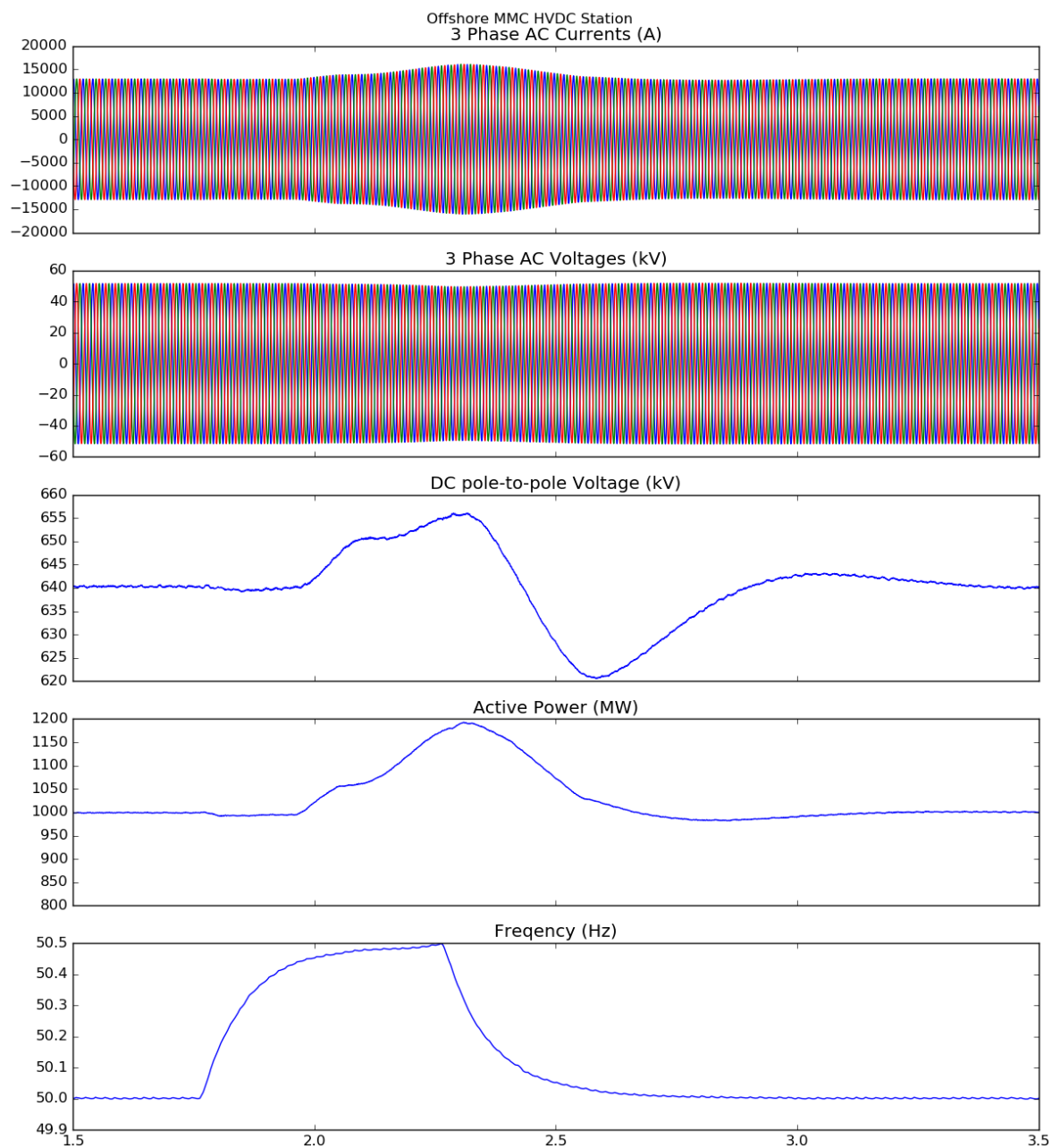


Figure 3-36 Results of the frequency response

A number of CHIL tests were also performed for the AC connection case, among others,

1. Active Filtering by STATCOM
2. Sub-synchronous Oscillation Suppression by STATCOM
3. Harmonic impedance measurement of STATCOM

Those tests results are less relevant in this deliverable therefore not included here.

4 GRID FORMING WPP DEMONSTRATION

4.1 INTRODUCTION

The CHiL demonstrator is used for compliance evaluation wind turbine and wind park controllers in realistic scenarios. The scenarios and functional requirements have been defined in D3.7 [16] “Compliance evaluation results using simulations”. In this document two main scenarios were set up to assess system performance:

- HVAC black start operation
- Point-to-point DRU connection

The functional requirements for both HVAC black start operation and for point-to-point DRU connection were defined in WP3. The functional requirements and test cases are defined in D3.1, D3.2 and D3.7 [16–18]. Functional requirements are in D3.1 for DRU connections and in D3.7 for black-start operation. Test cases and sensitivity analysis to be performed are included in D3.2 and D3.7 for DRU and black-start operation, respectively. The compliance evaluation of different WT and WPP controllers using EMT simulations was carried out in WP3.

To increase the TRL of the considered controllers, this section includes the results of the compliance evaluation results using the control hardware-in-the-loop demonstrator shown in section 2.4. Therefore, the considered scenarios, test cases and functional requirements for CHiL compliance evaluation will be those defined in WP3.

4.2 CHIL COMPLIANCE EVALUATION OF OFFSHORE WT AND WPP CONTROLLERS FOR HVAC BLACK START OPERATION

4.2.1 SYSTEM DESCRIPTION

The real-time simulation set-up physical set up is based around an OPAL RT-5700 simulator and is shown in Figure 2-12. The detailed characteristics are explained in section 2.4.

The system considered for black-start test is as follows:

- OWF of 400 MW, consisting of 50 x 8 MW WTGs connected to a 66kV ac collector (1 detailed string + 5 aggregated strings)
- 460 MVA off-shore transformer with a ratio of 66/220 kV.
- 75 km HVAC copper cable with a cross section of 1000 mm².
- Shunt compensators at the on-shore end of the cable. Off-shore compensation is not connected.
- 460 MVA on-shore transformer with a ratio of 220/400 kV.

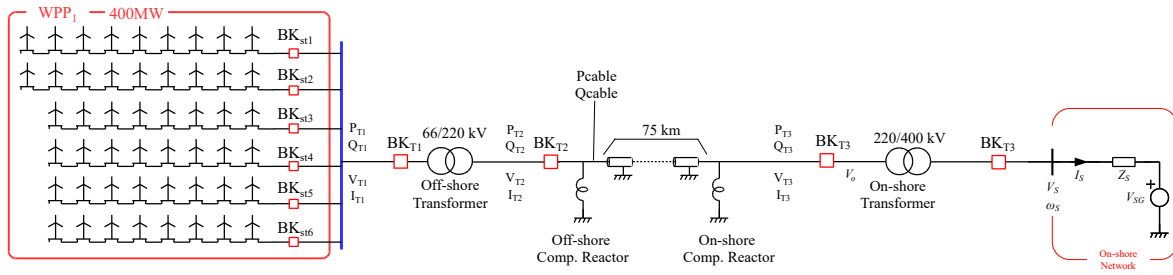


Figure 4-1: Schematic for HVAC black start operation

4.2.2 SEQUENTIAL BLACK START PROCEDURE

The sequential black start procedure considers the following steps:

- One wind turbine WTG-1,1 is powered up.
- WTG-1,1 energizes its transformer and the string 1 (soft energization).
- One by one all transformers and WT are connected in string 1 (8WT).
- Synchronization of WTGs connected to string 1.
- Breakers are closed.
- Connected WTGs energize the string n.
- Synchronization of WTGs connected to string n.
- The Offshore Wind Power Plant energizes the offshore substation.
- The Offshore Wind Power Plant energizes the transport cable.
- The Offshore Wind Power Plant energizes the onshore substation.
- Synchronization to onshore grid.
- Power block delivery.
- Synchronise to an adjacent island.

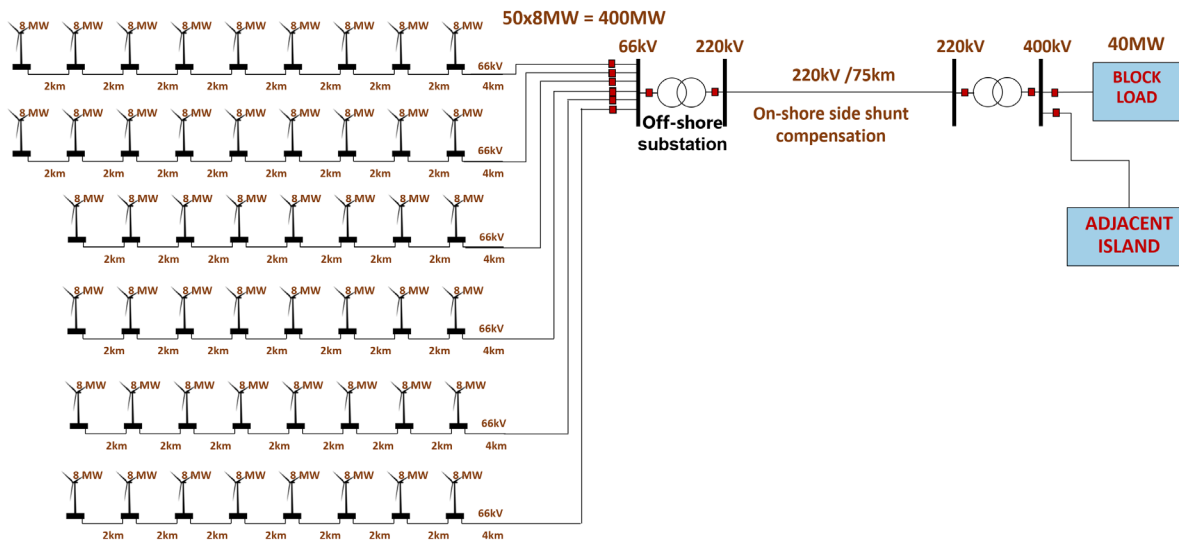


Figure 4-2: Diagram for the sequential black start

For the sequential black start, all the considered functional requirements must be met. The connection of the HVAC cable and the big substation transformers is particularly challenging as residual magnetisation and ferro-resonance between transformers and export cable can cause large over-currents and over-voltages that could trip the wind turbines. Therefore, Point of Wave switching is considered for these elements, with the test cases considering a relatively large spread error on each pole switching to consider ageing and wrong estimates of closing times and residual flux.

Another important issue is the response to load transients. A relatively large block load of 40MW (0.1pu) has been assumed. The load is DOL connected, which represents the worst-case scenario. Nevertheless, the wind turbines can keep the voltage within their limits during such a large block load. The sequential connection of smaller loads would therefore be also within the voltage limits, whereas the impact on the wind turbine mechanical components would be greatly reduced.

Finally, fault response and fault recovery are of particular importance, as the wind turbines should supply enough fault current for the protections to act, and, at the same time, keep it below the operational limits of the wind turbine converters. Moreover, once the fault has been cleared, the grid forming wind turbines should be able to carry out the voltage recovery of the complete system.

The test cases, defined in D3.7 and used also here, allow for the compliance evaluation of the wind turbine controllers during the aforementioned situations [16].

4.2.3 MACHINE SIDE CONVERTER CONTROL

The machine side controller is based on a vector-oriented control with the active current controlling the dc-link voltage, with the following assumptions:

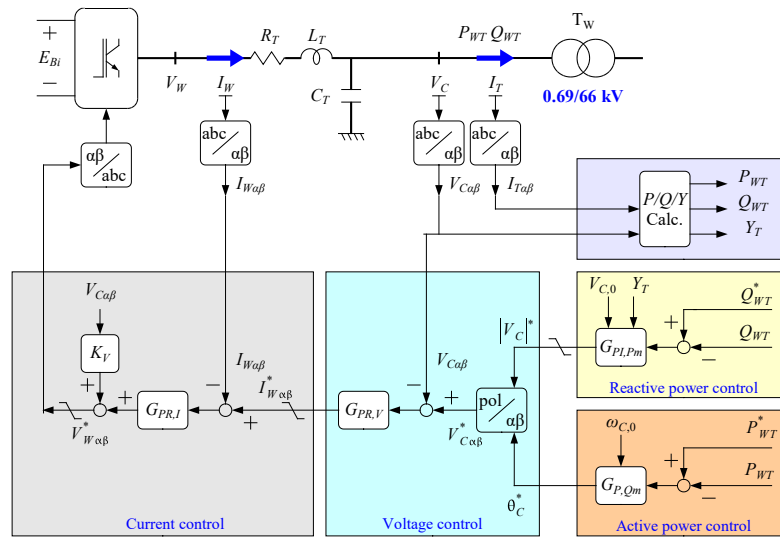


Figure 4-4: Grid side converter control

4.2.5 START UP AND SYNCHRONIZATION OF THE WTGS CONNECTED TO THE FIRST STRING

This test case begins with the connection of the first WTG and ends when all WTGs are connected. A sensitivity analysis for this case is not required, as the test itself includes the operation of a different number of wind turbines during each stage of the connection process.

D3.7 Test case	2.4.1. OFF-SHORE AC-GRID START-UP OPERATION		
	Configuration (connected strings)	Compliance	Comments
Simulations (sensitivity analysis)	6 Strings	pass	$P_{TOT} = 400 \text{ MW};$ WTG (max values): $V = 1.09 \text{ pu}; I = 0.81 \text{ pu};$ $P_{WT} = 0.04 \text{ pu}; Q_{WT} = -0.65 \text{ pu};$ PCC (max values): $V = 1.09 \text{ pu}; I = 0.0 \text{ pu};$ $P = 0 \text{ pu}; Q = 0 \text{ pu};$
Comments	The start-up process consists on the following basic steps: <ul style="list-style-type: none"> • WTG-1,1 energizes its transformer and the string cable. • Synchronisation of WTGs connected to string 1. • Connected WTGs energize the string n. • Synchronisation of WTGs connected to string n. 		

4.2.5.1 SOFT START OF WTG_{1,1}, ITS TRANSFORMER AND THE STRING CABLE

WTG_{1,1} is the first wind turbine to start, since only 5.2MVAR are required to energize the whole string cable, a single wind turbine can be used for this purpose. In the case of the string cable requires more reactive power than

one WTG can provide, the procedure has to be split into several steps, energizing the string cable section by section.

In order to avoid the harmonics and inrush currents that appear during transformer and cable energisation, the transformer and string cable are soft started by WTG_{1,1}.

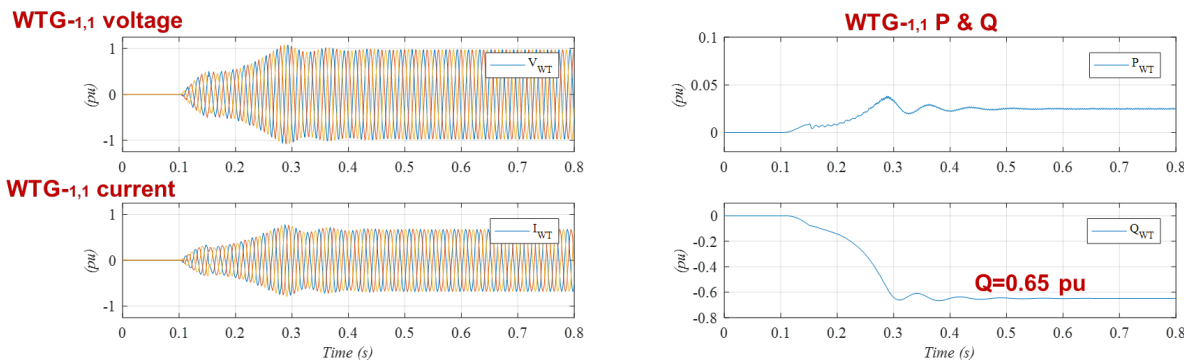


Figure 4-5: WTG_{1,1} start up.

Figure 4-5 shows the results of the soft energization of WTG_{1,1} transformer and the corresponding string cable. As commented before, the string cable energisation can be carried out with just a single WTG because the required reactive power is lower than the rated WTG power. Moreover, as the figure shows, the voltage exceeds 1pu during a short time without exceeding the 1.1 pu voltage limit.

4.2.5.2 CONNECTION OF THE SECOND WT (WTG-1,2) TRANSFORMER AND SYNCHRONIZATION

In the second step the second wind turbine must be energized. Hence, WTG_{1,2} transformer is connected at 3.45 seconds. For the individual wind turbine transformers, no POW is used, however transformer residual flux is considered. The in-rush currents produced by the transformer appear at WTG_{1,1} as shown in Figure 4-6. Once the transformer of the second wind turbine is energised, WTG_{1,2} begins its synchronization, which is finished at t=3.9 seconds (0.45 seconds after the transformer energization). Then, active and reactive power sharing between the connected WTGs begins. The active power oscillations arise, in part due to the start of the sharing control before the transformer connection has died out, and in part due to a fast transition from open to closed loop control on WTG-1.2. In any case, active power oscillations are well below 0.05pu and disappear in less than 500ms. At the end of the connection transient, both wind turbines share the total active and reactive power requirements.

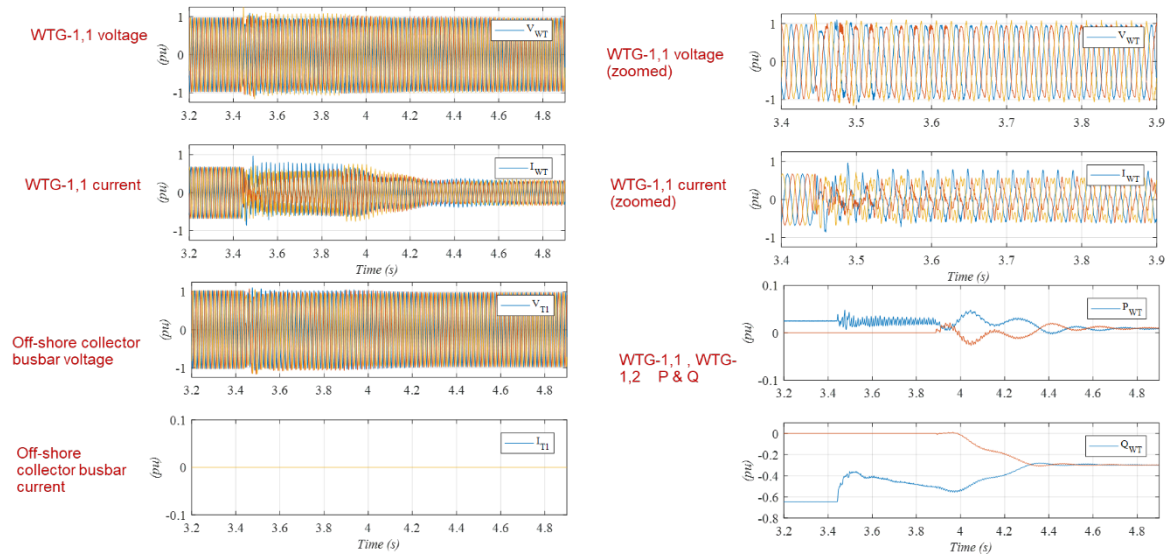


Figure 4-6: WTG1,2 energization and synchronization.

4.2.6 OFF SHORE SUBSTATION ENERGISATION USING POW

The off-shore substation is now energized, after all the wind turbines have been energized. The substation transformer is connected using point of wave switching (POW) with a random **error with a 2σ deviation of 2.5ms** in each pole (as in [16]). Moreover, off-shore substation energisation has been tested with different number of connected WTGs (6 cases considering the number of connected strings).

D3.7 Test case	2.4.6. OFF-SHORE HVAC SUBSTATION ENERGISATION		
	Configuration (connected strings)	Compliance	Comments
Simulations (sensitivity analysis)	6 Strings	pass	$P_{TOT} = 400$ MW; WTG (max values): $V = 0.95$ pu; $I = 0.11$ pu; $P_{WT} = 0.002$ pu; $Q_{WT} = -0.068$ pu; PCC (max values): $V = 0.95$ pu; $I = 0.03$ pu; $P = 0$ pu; $Q = 0$ pu;
	5 Strings	pass	$P_{TOT} = 328$ MW; WTG (max values): $V = 0.95$ pu; $I = 0.11$ pu; $P_{WT} = 0.004$ pu; $Q_{WT} = -0.068$ pu; PCC (max values): $V = 0.95$ pu; $I = 0.03$ pu; $P = 0$ pu; $Q = 0$ pu;
	4 Strings	pass	$P_{TOT} = 256$ MW; WTG (max values): $V = 0.95$ pu; $I = 0.13$ pu; $P_{WT} = 0.006$ pu; $Q_{WT} = -0.068$ pu; PCC (max values): $V = 0.95$ pu; $I = 0.03$ pu; $P = 0$ pu; $Q = 0$ pu;

	3 Strings	pass	$P_{TOT}= 192 \text{ MW};$ WTG (max values): $V= 0.95\text{pu}; I= 0.14\text{pu};$ $P_{WT}= 0.008 \text{ pu}; Q_{WT}= -0.068 \text{ pu};$ PCC (max values): $V= 0.95\text{pu}; I= 0.03\text{pu};$ $P =0\text{pu}; Q = 0 \text{ pu};$
	2 Strings	pass	$P_{TOT}= 128 \text{ MW};$ WTG (max values): $V= 0.95\text{pu}; I= 0.14\text{pu};$ $P_{WT}= 0.01 \text{ pu}; Q_{WT}= -0.068 \text{ pu};$ PCC (max values): $V= 0.95\text{pu}; I= 0.03\text{pu};$ $P =0\text{pu}; Q = 0 \text{ pu};$
	1 Strings	pass	$P_{TOT}= 64 \text{ MW};$ WTG (max values): $V= 0.95\text{pu}; I= 0.15\text{pu};$ $P_{WT}= 0.018 \text{ pu}; Q_{WT}= -0.068 \text{ pu};$ PCC (max values): $V= 0.95\text{pu}; I= 0.03\text{pu};$ $P =0\text{pu}; Q = 0 \text{ pu};$
Comments	<p>The obtained results are similar to the presented in deliverable D3.7 of WP3 [16]. The energisation of the off-shore substation can be carried out with at least 1 connected string. The smaller the number of connected WTGs, the larger active power each one has to produce. In any case produced active power is smaller than 0.02 pu. The same applies to the reactive power requirements.</p>		

The case of all strings connected is shown in Figure 4-7.

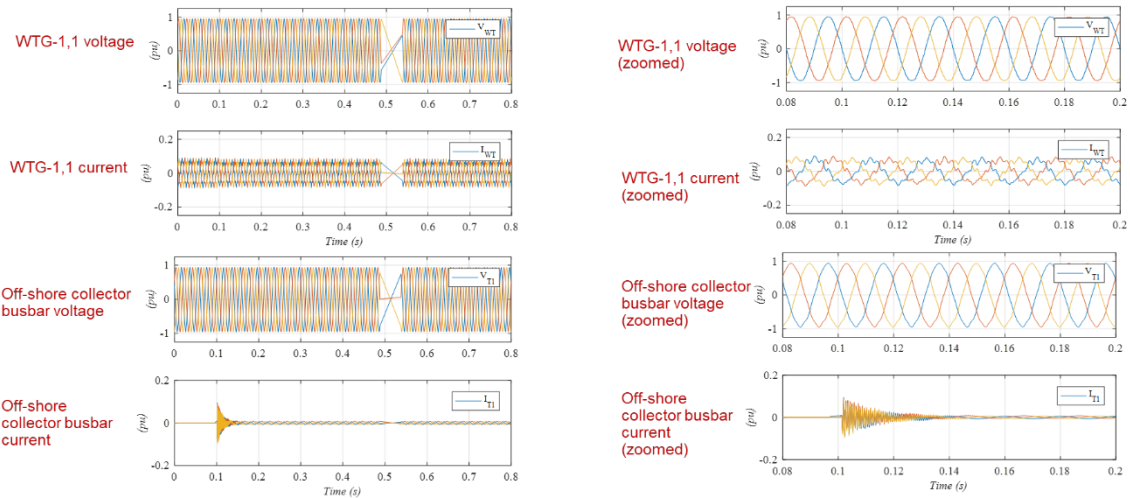


Figure 4-7: Substation energization (3 phase voltages and currents)

The gaps in the graphs are due to the process of data capture, as the real time system prioritizes real time calculations over supervisory communication.

Figure 4-7 shows that the use of POW (with the previously explained random error to achieve more realistic results) allows for a reduction on inrush currents. The off-shore transformer current IT1 shows the low level of inrush current that appear (less than 10% of the transformer nominal current). Even though relatively large POW pole switching errors are considered, the use of POW is advisable as DOL connection would, in many cases, lead to over-currents and over-voltages that would trip the wind turbines.

Figure 4-8 shows the rms voltage and currents at off-shore transformer terminals. Clearly, the current rms is smaller than 0.03 pu during the complete transient.

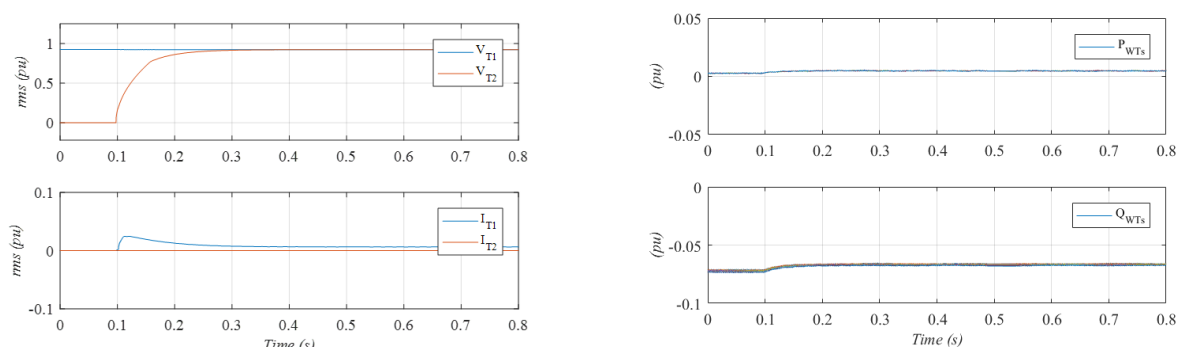


Figure 4-8: Substation energization (rms voltage and current at the off-shore substation and WTGs active and reactive power).

4.2.7 EXPORT CABLE ENERGIZATION (DIRECT CONNECTION)

The most challenging part could be probably energizing the 75 km export cable. The export cable is energised with just 40% of reactive power compensation (the energisation is carried out with just the on-shore shunt reactor connected). If the export cable reactive power is over compensated, a current zero miss can appear. Therefore, protection breakers may take a very long time to clear eventual faults.

With just the 40% of reactive power compensation, the reactive power required is around 108 MVAR. It means that the export cable energisation cannot be carried out with just 1 string connected (64MVAR).

Moreover, POW switching is used to close the breaker to reduce over-currents and over-voltages during cable connection. The POW switching includes a random error of 2.5 ms on the closure of each pole (the same as in [16]).

D3.7 Test case	2.4.7. HVAC EXPORT CABLE ENERGISATION		
	Configuration (connected strings)	Compliance	Comments
Simulations (sensitivity analysis)	6 Strings	pass	$P_{TOT} = 400$ MW; WTG (max values): $V = 0.96$ pu; $I = 0.42$ pu; $P_{WT} = 0.08$ pu; $Q_{WT} = -0.81$ pu; PCC (max values): $V = 1.07$ pu; $I = 0.52$ pu; $P = 0.06$ pu; $Q = -0.24$ pu;
	5 Strings	pass	$P_{TOT} = 328$ MW; WTG (max values): $V = 0.97$ pu; $I = 0.48$ pu; $P_{WT} = 0.12$ pu; $Q_{WT} = -0.67$ pu; PCC (max values): $V = 1.09$ pu; $I = 0.60$ pu; $P = 0.06$ pu; $Q = -0.24$ pu;

	4 Strings	pass	$P_{TOT} = 256 \text{ MW}$; WTG (max values): $V = 0.97 \text{ pu}$; $I = 0.51 \text{ pu}$; $P_{WT} = 0.18 \text{ pu}$; $Q_{WT} = -0.78 \text{ pu}$; PCC (max values): $V = 1.08 \text{ pu}$; $I = 0.55 \text{ pu}$; $P = 0.06 \text{ pu}$; $Q = -0.24 \text{ pu}$;
	3 Strings	pass	$P_{TOT} = 192 \text{ MW}$; WTG (max values): $V = 0.98 \text{ pu}$; $I = 0.64 \text{ pu}$; $P_{WT} = 0.22 \text{ pu}$; $Q_{WT} = -0.79 \text{ pu}$; PCC (max values): $V = 1.08 \text{ pu}$; $I = 0.48 \text{ pu}$; $P = 0.06 \text{ pu}$; $Q = -0.23 \text{ pu}$;
	2 Strings	pass	$P_{TOT} = 128 \text{ MW}$; WTG (max values): $V = 0.98 \text{ pu}$; $I = 0.96 \text{ pu}$; $P_{WT} = 0.28 \text{ pu}$; $Q_{WT} = -0.9 \text{ pu}$; PCC (max values): $V = 1.08 \text{ pu}$; $I = 0.61 \text{ pu}$; $P = 0.06 \text{ pu}$; $Q = -0.24 \text{ pu}$;
	1 Strings	not tested	$P_{TOT} = 64 \text{ MW}$; Not enough capacity to compensate the reactive power produced by the export cable.
Comments	As the results presented in deliverable D3.7 of WP3 [16], the export cable energisation cannot be carried out with 1 string because of insufficient reactive power generation.		

Figure 4-9, Figure 4-10 and Figure 4-11 show the results of the export cable energisation with all the WTGs connected. The harmonics disappear in about 4 seconds (similar than the presented results in [16]).



Figure 4-9: Voltages and currents during the export cable energization (WTG1,1 Voltage and current).

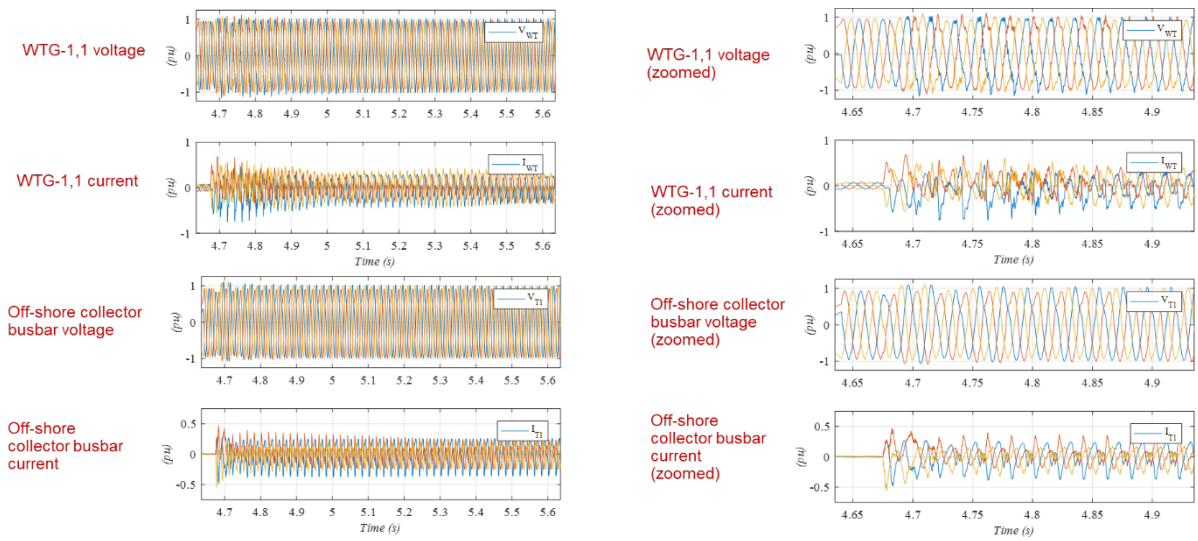


Figure 4-10: Export cable energization.

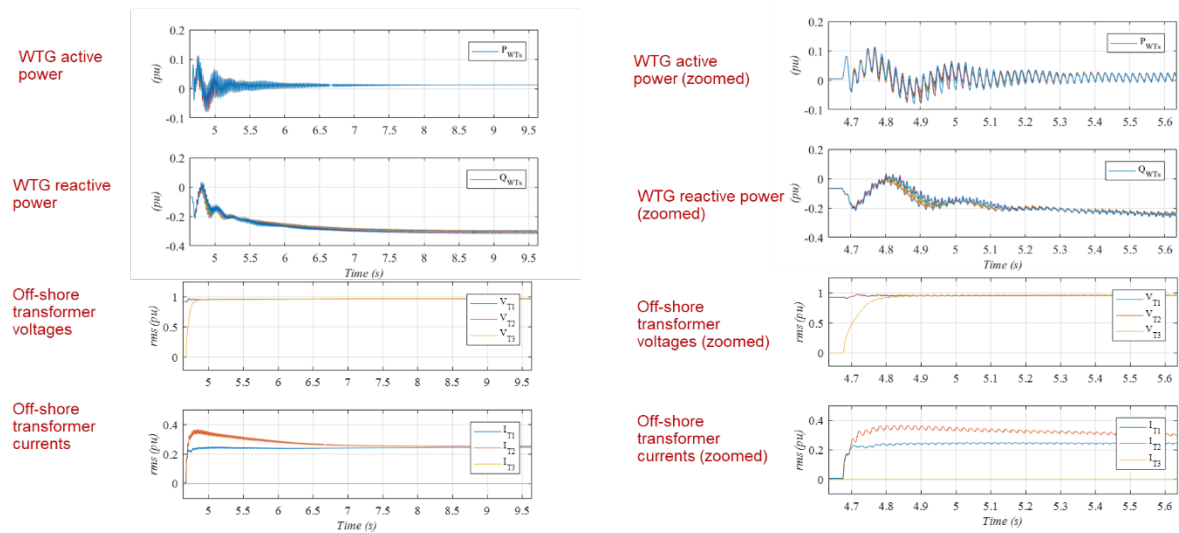


Figure 4-11: Export cable energization (WTGs active and reactive powers). V_{T1} , I_{T1} are the 66kV collector busbar voltage and current, whereas V_{T2} , I_{T2} , V_{T3} , I_{T3} are the voltages and currents at the off-shore and on-shore side of the 220kV export cable, respectively

Figure 4-11 shows the WTGs active and reactive powers and on-shore and off-shore substations rms voltages and currents. The voltage and current ripple do not exceed 15%, again thanks to the use of POW switching to energise the export cable.

4.2.8 ON SHORE SUBSTATION ENERGISATION (POW)

A POW switching with a random error of 2.5 second in each breaker pole is used for the on-shore substation energization, to obtain more realistic results. Moreover, as the export cable requires a minimum of 2 strings connected, the on-shore substation energisation cannot be carried out using just 1 string.

D3.7 Test case	2.4.11. ON-SHORE HVAC SUBSTATION ENERGISATION		
	Configuration (connected strings)	Compliance	Comments
Simulations (sensitivity analysis)	6 Strings	pass	$P_{TOT}= 400$ MW; WTG (max values): $V= 0.96pu$; $I= 0.49pu$; $P_{WT}= 0.02$ pu; $Q_{WT}= -0.31$ pu; PCC (max values): $V= 1.0pu$; $I= 0.45pu$; $P =0.01pu$; $Q = -0.22$ pu;
	5 Strings	pass	$P_{TOT}= 328$ MW; WTG (max values): $V= 0.96pu$; $I= 0.7pu$; $P_{WT}= 0.02$ pu; $Q_{WT}= -0.41$ pu; PCC (max values): $V= 1.01pu$; $I= 0.24pu$; $P =0.01pu$; $Q = -0.22$ pu;
	4 Strings	pass	$P_{TOT}= 256$ MW; WTG (max values): $V= 0.97pu$; $I= 0.72pu$; $P_{WT}= 0.02$ pu; $Q_{WT}= -0.42$ pu; PCC (max values): $V= 1.01pu$; $I= 0.35pu$; $P =0.01pu$; $Q = -0.25$ pu;
	3 Strings	pass	$P_{TOT}= 192$ MW; WTG (max values): $V= 0.96pu$; $I= 0.61pu$; $P_{WT}= 0.04$ pu; $Q_{WT}= -0.54$ pu; PCC (max values): $V= 1.02pu$; $I= 0.25pu$; $P =0.01pu$; $Q = -0.23$ pu;
	2 Strings	pass	$P_{TOT}= 128$ MW; WTG (max values): $V= 0.97pu$; $I= 0.91pu$; $P_{WT}= 0.06$ pu; $Q_{WT}= -0.81$ pu; PCC (max values): $V= 1.01pu$; $I= 0.25pu$; $P =0.01pu$; $Q = -0.25$ pu;
	1 Strings	not tested	$P_{TOT}= 64$ MW; Not enough capacity to compensate the reactive power produced by the export cable.
Comments	As the results presented in deliverable D3.7 of WP3 [16], the export cable energisation cannot be carried out with 1 string because there is not enough reactive power to do it. This result is similar to the presented in [16].		

The results shown in Figure 4-12 correspond with the on-shore substation energisation using the complete WPP. Transients during the onshore substation energization are smoother than the ones during cable energization, as expected. Active and reactive power, currents and voltages are well within the considered operational limits. The in-rush currents (see Figure 4-12) die away in about 5 seconds as shown in Figure 4-13.

As in the previous cases, POW with random pole closing error has been used for on-shore transformer energization.

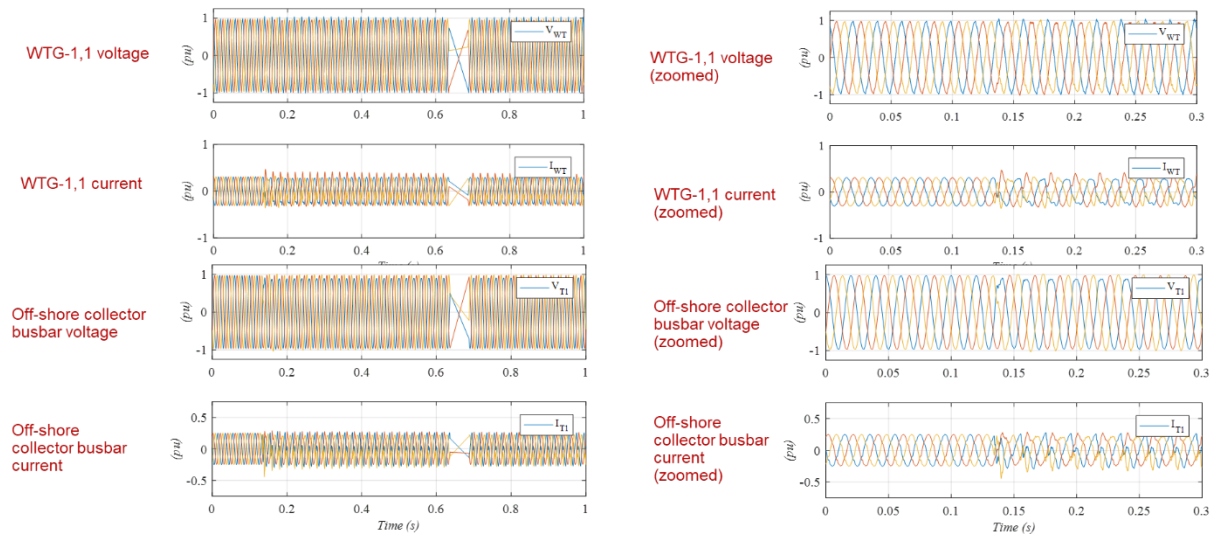


Figure 4-12: Voltage and Currents in WTG1-1 and offshore collector during on shore substation energization.

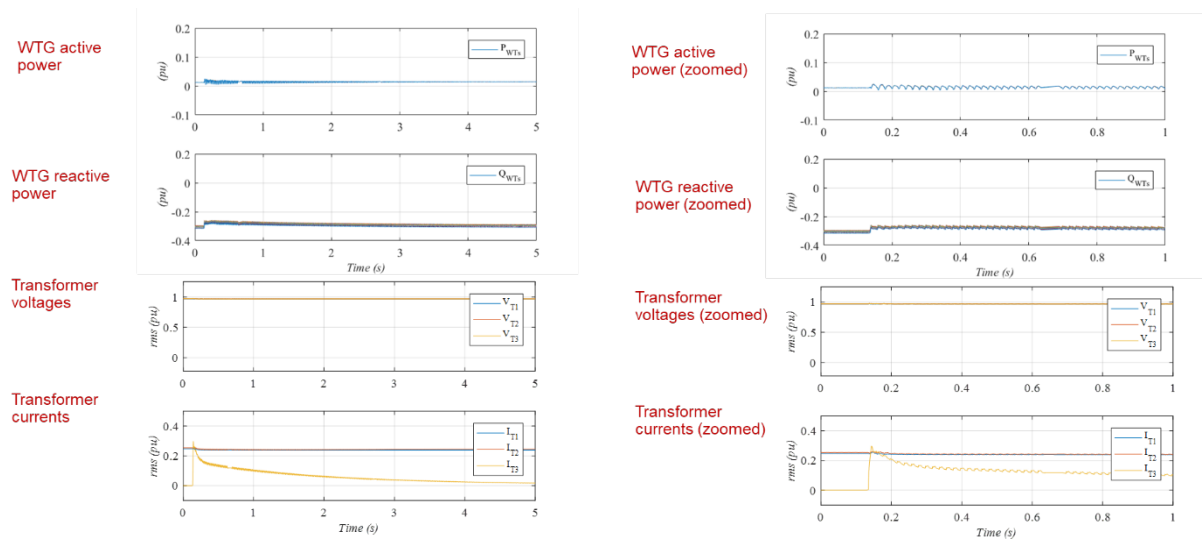


Figure 4-13: RMS Voltage and Currents in WTG1-1 and offshore collector during on shore substation energization. V_{T1} , I_{T1} are the 66kV collector busbar voltage and current, whereas V_{T2} , I_{T2} , V_{T3} , I_{T3} are the voltages and currents at the off-shore and on-shore side of the 220kV export cable, respectively

4.2.9 40 MW POWER BLOCK CONNECTION / DISCONNECTION

This test case shows the connection/disconnection of a 10% (40MW) on-shore block load. It is important to ensure that the available active power in the WTG is enough to connect the load.

D3.7 Test case	2.4.13.a POWER BLOCK DELIVERY (HVAC)		
	Configuration (connected strings)	Compliance	Comments
Simulations (sensitivity analysis)	6 Strings	pass	$P_{TOT} = 400$ MW; WTG (max values): $V = 0.96$ pu; $I = 0.39$ pu; $P_{WT} = 0.12$ pu; $Q_{WT} = -0.31$ pu; PCC (max values): $V = 1.01$ pu; $I = 0.29$ pu; $P = 0.11$ pu; $Q = -0.15$ pu;
	5 Strings	pass	$P_{TOT} = 328$ MW; WTG (max values): $V = 0.96$ pu; $I = 0.45$ pu; $P_{WT} = 0.13$ pu; $Q_{WT} = -0.36$ pu; PCC (max values): $V = 1.01$ pu; $I = 0.3$ pu; $P = 0.11$ pu; $Q = -0.15$ pu;
	4 Strings	pass	$P_{TOT} = 256$ MW; WTG (max values): $V = 0.97$ pu; $I = 0.52$ pu; $P_{WT} = 0.17$ pu; $Q_{WT} = -0.44$ pu; PCC (max values): $V = 1.02$ pu; $I = 0.29$ pu; $P = 0.12$ pu; $Q = -0.16$ pu;
	3 Strings	pass	$P_{TOT} = 192$ MW; WTG (max values): $V = 0.96$ pu; $I = 0.66$ pu; $P_{WT} = 0.24$ pu; $Q_{WT} = -0.56$ pu; PCC (max values): $V = 1.03$ pu; $I = 0.29$ pu; $P = 0.12$ pu; $Q = -0.16$ pu;
	2 Strings	pass	$P_{TOT} = 128$ MW; WTG (max values): $V = 0.97$ pu; $I = 0.98$ pu; $P_{WT} = 0.4$ pu; $Q_{WT} = -0.81$ pu; PCC (max values): $V = 1.03$ pu; $I = 0.31$ pu; $P = 0.13$ pu; $Q = -0.16$ pu;
	1 Strings	not tested	$P_{TOT} = 64$ MW; Not enough capacity to compensate the reactive power produced by the export cable.
Comments	As the results presented in deliverable D3.7 of WP3 [16], the export cable energisation cannot be carried out with 1 string because there is not enough reactive power to do it.		

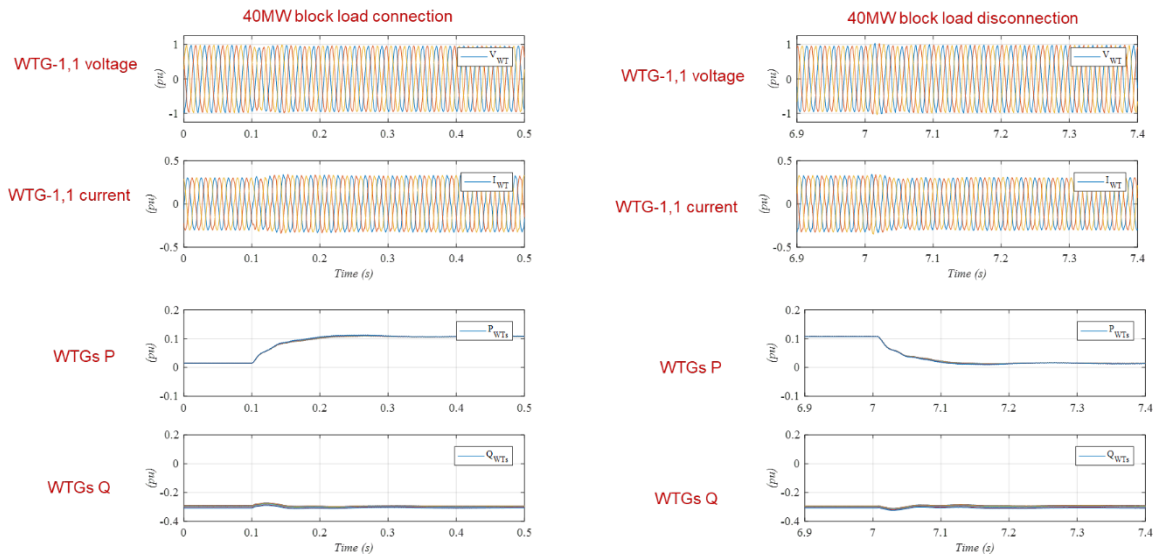


Figure 4-14: 40 MW block connection and disconnection.

Figure 4-14 shows the WTG-1,1 voltage and current, as well as all the WTGs active and reactive power, during block load connection. The block load is DOL connected, so it represents a worst-case scenario. Wind turbines react to the block load connection or disconnection in less than 50ms. The voltage dip during block load connection and the voltage surge during disconnection are always within the $\pm 10\%$ allowed voltage variation. Active and reactive power are shared adequately by all the wind turbines during both block load connection and disconnection.

4.2.10 SYNCHRONISATION TO EXISTING ON-SHORE HVAC GRID

Sequential black start is completed once the system is synchronised to an adjacent island. The considered procedure for synchronisation is as follows:

- Synchronisation relay measures voltage phase and magnitude difference and sends them to the WPP controller every second.
- The WPP controller changes off-shore wind farm voltage and frequency set point accordingly, aiming to reduce angle and magnitude difference at the connection point.
- Local synchronising relay closes when voltage phase / magnitude are below the pre-defined threshold.

Therefore, this system allows for adequate synchronisation without using relatively slow communication.

D3.7 Test case	2.4.12. SYNCHRONISATION TO AN ON-SHORE GRID		
	Configuration (connected strings)	Compliance	Comments
Simulations (sensitivity analysis)	6 Strings	pass	$P_{TOT} = 400$ MW; WTG (max values): $V = 0.96$ pu; $I = 0.38$ pu; $P_{WT} = 0.01$ pu; $Q_{WT} = -0.35$ pu; PCC (max values): $V = 0.99$ pu; $I = 0.15$ pu; $P = 0.01$ pu; $Q = -0.14$ pu;
	5 Strings	pass	$P_{TOT} = 328$ MW; WTG (max values): $V = 0.96$ pu; $I = 0.43$ pu; $P_{WT} = 0.01$ pu; $Q_{WT} = -0.42$ pu; PCC (max values): $V = 0.99$ pu; $I = 0.15$ pu; $P = 0.01$ pu; $Q = -0.15$ pu;
	4 Strings	pass	$P_{TOT} = 256$ MW; WTG (max values): $V = 0.97$ pu; $I = 0.52$ pu; $P_{WT} = 0.02$ pu; $Q_{WT} = -0.47$ pu; PCC (max values): $V = 1.01$ pu; $I = 0.16$ pu; $P = 0.01$ pu; $Q = -0.16$ pu;
	3 Strings	pass	$P_{TOT} = 192$ MW; WTG (max values): $V = 0.96$ pu; $I = 0.66$ pu; $P_{WT} = 0.02$ pu; $Q_{WT} = -0.64$ pu; PCC (max values): $V = 1.01$ pu; $I = 0.16$ pu; $P = 0.01$ pu; $Q = -0.16$ pu;
	2 Strings	pass	$P_{TOT} = 128$ MW; WTG (max values): $V = 0.97$ pu; $I = 0.92$ pu; $P_{WT} = 0.04$ pu; $Q_{WT} = -0.91$ pu; PCC (max values): $V = 1.01$ pu; $I = 0.16$ pu; $P = 0.13$ pu; $Q = -0.16$ pu;
	1 Strings	not tested	$P_{TOT} = 64$ MW; Not enough capacity to compensate the reactive power produced by the export cable.
Comments	As the results presented in deliverable D3.7 of WP3, the export cable energisation cannot be carried out with 1 string because there is not enough reactive power to do it.		

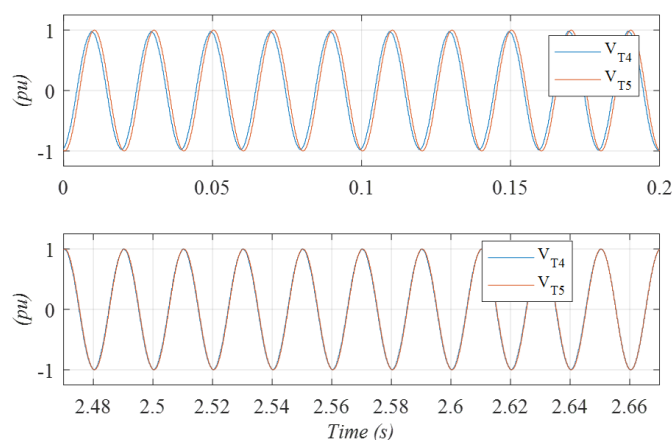


Figure 4-15: Voltages in different WT during synchronization.

Figure 4-15 shows the voltages at both sides of the breaker connecting to the adjacent island. The top graph shows the initial phase and magnitude difference, whereas the bottom graph shows that both voltage magnitude and phase are the same at both sides of the breaker. At this point, the synchronisation relay closes the corresponding breaker. The complete process usually takes less than 1 minute to complete.

4.2.11 HVAC EXPORT CABLE FAULT

This test case aims at checking the system behaviour during a HVAC export cable symmetrical fault.

The grid forming wind turbines must provide enough current for the relays to detect the fault. It is assumed that the export cable fault is non-recoverable and hence, active power production cannot be resumed after the fault is cleared. Nevertheless, when the fault is cleared the OWPP reverts to islanding operation in order to supply both WPP and off-shore substation auxiliaries.

D3.7 Test case	2.5.1. HVAC EXPORT CABLE FAULTS		
	Configuration (connected strings)	Compliance	Comments
Simulations (sensitivity analysis)	6 Strings	pass	$P_{TOT} = 400 \text{ MW}$; WTG (max values): $V = 1.02 \text{ pu}$; $I = 1.38 \text{ pu}$; $P_{WT} = 0.16 \text{ pu}$; $Q_{WT} = -0.32 \text{ pu}$; PCC (max values): $V = 1.0 \text{ pu}$; $I = 1.52 \text{ pu}$; $P = 0.16 \text{ pu}$; $Q = -0.25 \text{ pu}$;
	5 Strings	pass	$P_{TOT} = 328 \text{ MW}$; WTG (max values): $V = 1.03 \text{ pu}$; $I = 1.41 \text{ pu}$; $P_{WT} = 0.22 \text{ pu}$; $Q_{WT} = -0.39 \text{ pu}$; PCC (max values): $V = 1.0 \text{ pu}$; $I = 1.55 \text{ pu}$; $P = 0.16 \text{ pu}$; $Q = -0.25 \text{ pu}$;

	4 Strings	pass	$P_{TOT}= 256 \text{ MW};$ WTG (max values): $V= 1.02\text{pu}; I= 1.39\text{pu};$ $P_{WT}= 0.28 \text{ pu}; Q_{WT}= -0.48 \text{ pu};$ PCC (max values): $V= 1.0\text{pu}; I= 1.52\text{pu};$ $P =0.16\text{pu}; Q = -0.25 \text{ pu};$
	3 Strings	pass	$P_{TOT}= 192 \text{ MW};$ WTG (max values): $V= 1.02\text{pu}; I= 1.37\text{pu};$ $P_{WT}= 0.32 \text{ pu}; Q_{WT}= -0.58 \text{ pu};$ PCC (max values): $V= 1.0\text{pu}; I= 1.49\text{pu};$ $P =0.16\text{pu}; Q = -0.25 \text{ pu};$
	2 Strings	pass	$P_{TOT}= 128 \text{ MW};$ WTG (max values): $V= 1.03\text{pu}; I= 1.44\text{pu};$ $P_{WT}= 0.45 \text{ pu}; Q_{WT}= -0.91 \text{ pu};$ PCC (max values): $V= 1.0\text{pu}; I= 1.58\text{pu};$ $P =0.16\text{pu}; Q = -0.25 \text{ pu};$
	1 Strings	not tested	$P_{TOT}= 64 \text{ MW};$ Not enough capacity to compensate the reactive power produced by the export cable.
Comments	As the results presented in deliverable D3.7 of WP3 [16], the export cable energisation cannot be carried out with 1 string because there is not enough reactive power to do it.		

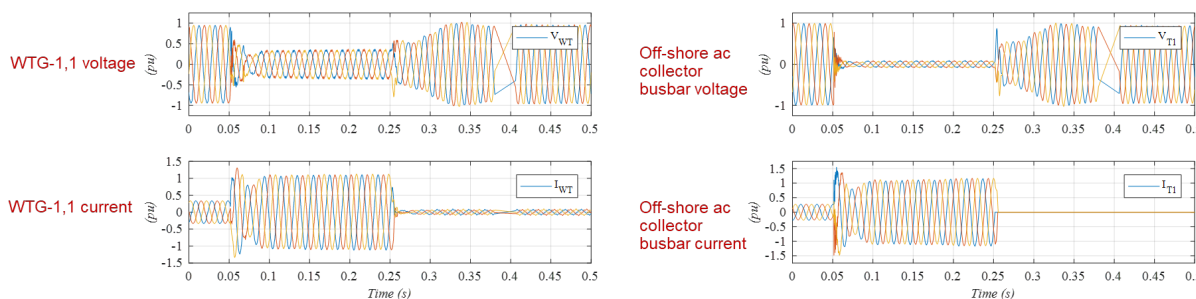


Figure 4-16: Voltages and currents during an HVAC cable fault.

Figure 4-16 shows the voltages and currents at WTG-1,1 and at the 66kV off-shore collector busbar. The wind turbines limit the total current during the fault. Once the fault is cleared, the wind turbines recover the collector array voltage in less than 50 ms. At this stage, the current through the export cable is zero and the wind turbines are in islanding mode of operation.

4.2.12 SOFT START ENERGISATION

The final test case includes the soft-start energisation of the system up to the on-shore substation. For the soft start energisation, initially, all breakers up to the on-shore substation are closed. Then, the WPP controller ramps up the reference voltage set-point to 1 pu, which is reached in less than 2 seconds. The ramping up time is selectable and can be made slightly longer to avoid any current transients if it is suspected that the transformers

have relatively large residual flux. Figure 4-17 shows the complete soft start process, where the voltage and current oscillations in all parts of the system are avoided.

D3.7 Test case	2.4.14.a SOFT ENERGISATION (FROM HOUSELOAD TO POWER BLOCK) HVAC		
	Configuration (connected strings)	Compliance	Comments
Simulations (sensitivity analysis)	6 Strings	pass	$P_{TOT} = 400$ MW; WTG (max values): $V = 0.98$ pu; $I = 0.38$ pu; $P_{WT} = 0.08$ pu; $Q_{WT} = -0.35$ pu; PCC (max values): $V = 1.01$ pu; $I = 0.17$ pu; $P = 0.05$ pu; $Q = -0.16$ pu;
	5 Strings	pass	$P_{TOT} = 328$ MW; WTG (max values): $V = 0.98$ pu; $I = 0.43$ pu; $P_{WT} = 0.1$ pu; $Q_{WT} = -0.42$ pu; PCC (max values): $V = 1.03$ pu; $I = 0.17$ pu; $P = 0.08$ pu; $Q = -0.15$ pu;
	4 Strings	pass	$P_{TOT} = 256$ MW; WTG (max values): $V = 0.97$ pu; $I = 0.59$ pu; $P_{WT} = 0.14$ pu; $Q_{WT} = -0.51$ pu; PCC (max values): $V = 1.01$ pu; $I = 0.17$ pu; $P = 0.05$ pu; $Q = -0.17$ pu;
	3 Strings	pass	$P_{TOT} = 192$ MW; WTG (max values): $V = 0.96$ pu; $I = 0.72$ pu; $P_{WT} = 0.19$ pu; $Q_{WT} = -0.64$ pu; PCC (max values): $V = 1.01$ pu; $I = 0.17$ pu; $P = 0.05$ pu; $Q = -0.17$ pu;
	2 Strings	pass	$P_{TOT} = 128$ MW; WTG (max values): $V = 0.97$ pu; $I = 0.99$ pu; $P_{WT} = 0.32$ pu; $Q_{WT} = -0.94$ pu; PCC (max values): $V = 1.01$ pu; $I = 0.18$ pu; $P = 0.05$ pu; $Q = -0.18$ pu;
	1 Strings	not tested	$P_{TOT} = 64$ MW; Not enough capacity to compensate the reactive power produced by the export cable.
Comments	As the results presented in deliverable D3.7 of WP3 [16], the export cable energisation cannot be carried out with 1 string because there is not enough reactive power to do it.		

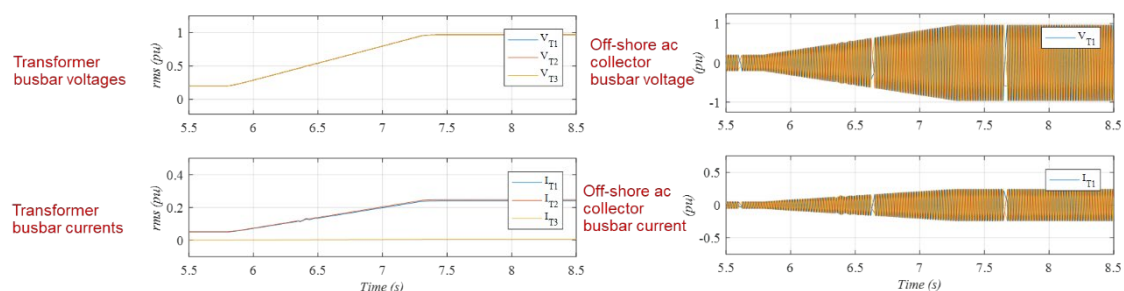


Figure 4-17: Soft start operation.

4.2.13 DISCUSSION

This section has shown the CHIL compliance evaluation of wind turbine and wind power plant controllers for black start operation of a HVAC connected wind power plant. The results largely agree with those obtained in [16]. The following conclusions can be made:

- Grid Forming WTG control using CHIL compliance evaluation has to be carried out with a sufficient number of WTGs to ensure WT interaction effects are considered. In this way, interaction, resonance and protection coordination issues can be identified at an early stage.
- The proposed scheme can cater for DLL based controllers, DSP based controller and full control cabinets. For the previous results, the controller of one of the WTs is external and the rest are DLL based.
- Sequential black start procedure might lead to overvoltage/overcurrent due to inrush currents, ferromagnetic oscillations and takes a relatively long time. Can be done with careful studies and tests (including POW switching with pole spread analysis).
- Soft start leads to much faster energization time and minimises inrush current and oscillations.
- Fault response and fault recovery is very important with a large number of grid forming WTGs. The considered results show adequate fault response and fault recovery.

4.3 CHIL COMPLIANCE EVALUATION OF OFFSHORE WT AND WPP CONTROLLERS FOR POINT-TO-POINT DIODE RECTIFIER UNIT (DRU) CONNECTIONS

4.3.1 SYSTEM DESCRIPTION

The considered systems and test cases are based on D3.1 “Detailed functional requirements to WPPs” and D3.4 “Results on control strategies of WPPS connected to DR-HVDC” [17, 19]. A summary of the considered system for DRU-enabled wind turbine and wind power plant controller compliance evaluation is as follows (Figure 4-18):

- 3 x OWF of 400MW, consisting of 50 x 8MW WTGs connected to a 66kV ac collector (1 detailed string + 5 aggregated strings + 2 aggregated OWF)
- 3 DRU platform (DRU + ac filters + dc filters) 66kV on the ac side.
- ± 320 kV HVDC cable 150km.

- Onshore MMC 1200MW (401 levels) half bridge.

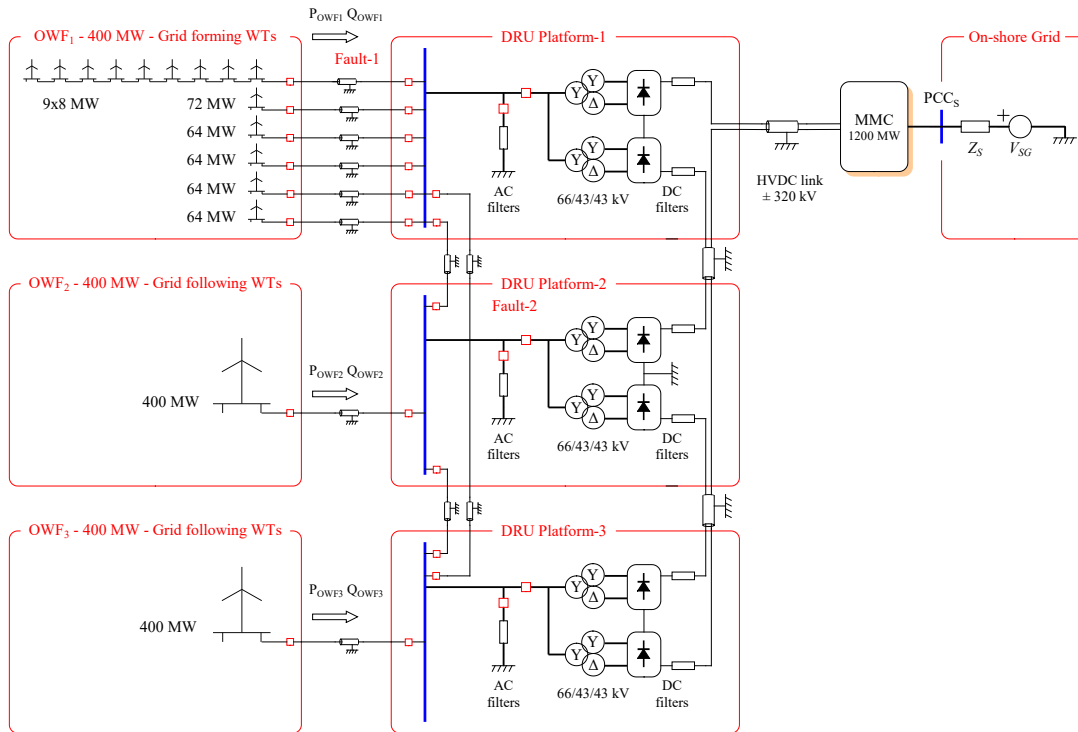


Figure 4-18: System considered with DRUs, grid forming WTs and on-shore MMC

4.3.2 GRID SIDE CONVERTER CONTROL

The machine side control is exactly the same as in previous black start test. However, the grid side converter control is different, now is based on P/V, Q/ ω droops. It considers internal stationary frame voltage and current loops and does not use a PLL (Figure 4-19).

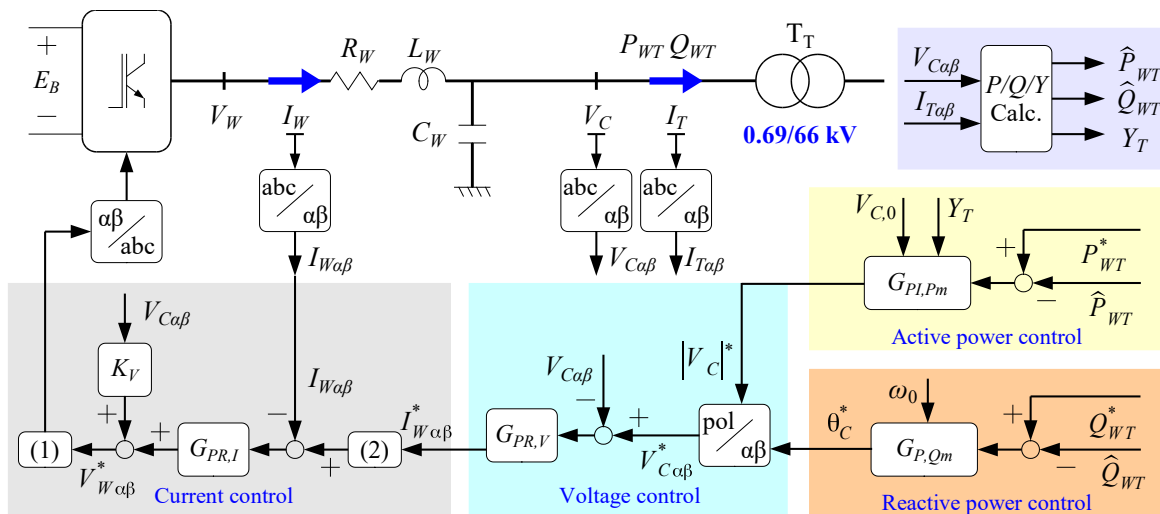


Figure 4-19: Control diagram for the grid side converter

4.3.3 DYNAMIC VOLTAGE CONTROL DURING ISLANDING OPERATION (DRU NOT CONDUCTING)

This test case is used to test the response of the islanded wind power plant to changes on off-shore ac grid voltage set-point. Therefore, it is used to validate the capability of the WPP to control the off-shore ac grid voltage and demonstrates that the WPP remains stable during islanding operation.

D3.7 Test case	4.2.4. DYNAMIC VOLTAGE CONTROL		
	Configuration (connected strings)	Compliance	Comments
Simulations (sensitivity analysis)	6 Strings +1 OWF + 1 OWF	pass	$P_{TOT}= 1200$ MW; WTG (max values): $V= 0.92pu$; $I= 0.12pu$; $P_{WT}= 0.005 pu$; $Q_{WT}= -0.08 pu$;
	6 Strings +1 OWF + 0 OWF	pass	$P_{TOT}= 800$ MW; WTG (max values): $V= 0.92pu$; $I= 0.17pu$; $P_{WT}= 0.005 pu$; $Q_{WT}= -0.12 pu$;
	6 Strings +0 OWF + 0 OWF	pass	$P_{TOT}= 400$ MW; WTG (max values): $V= 0.92pu$; $I= 0.27pu$; $P_{WT}= 0.01 pu$; $Q_{WT}= -0.24 pu$;
	3 Strings +0 OWF + 0 OWF	pass	$P_{TOT}= 192$ MW; WTG (max values): $V= 0.92pu$; $I= 0.58pu$; $P_{WT}= 0.01 pu$; $Q_{WT}= -0.52 pu$;
Comments	The results are similar to the ones presented in deliverable D3.7 of WP3 [16].		

In this test case, the DRUs are not conducting. Therefore, the off-shore ac-grid voltage has to be controlled by the WTs. Reactive power contribution is shared amongst wind turbines. Figure 4-20 shows the response to a change on grid voltage set-point from 0.9pu to 0.8pu and then back to 0.9pu. The WPP remains stable during the complete transient. Note the active power is near to zero since the WPP is operating in islanding mode and hence only supplying losses and wind turbine ancillaries. Moreover, the reactive power increases/decreases when the voltage increases/decreases that validates that the WPP is operating as expected.

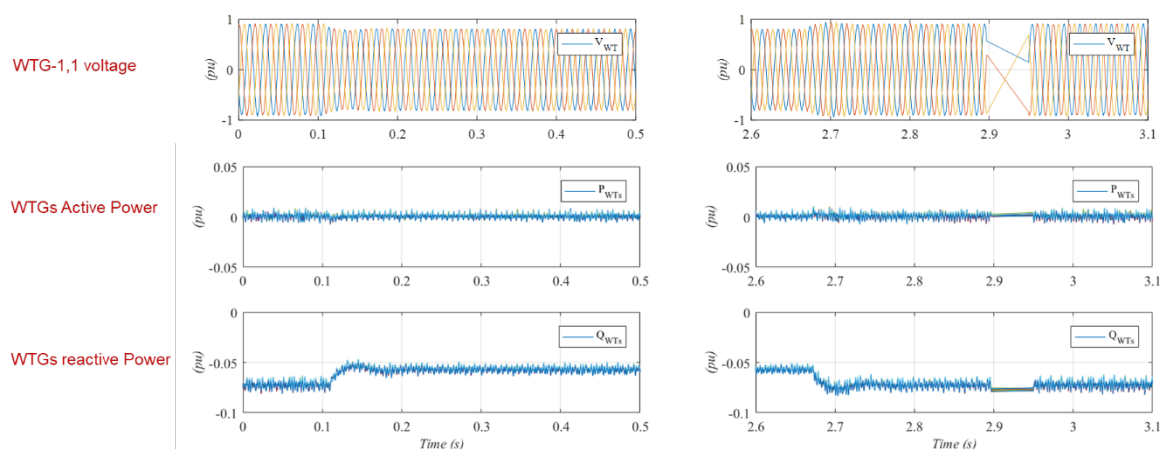


Figure 4-20: Islanded operation of WPP

4.3.4 FILTER CONNECTION AND CHANGE FROM ISLANDED TO CONNECTED OPERATION

This test case is the last step of the test case “4.2.1. HVDC LINK AND OFF-SHORE AC-GRID START-UP OPERATION” defined in [16]. The first part consists of the start-up and synchronisation of the WPP, leading to results that are basically the same as those in section 4.2.5, which will not be repeated here. This test case includes the transition from islanding operation to DR operation. Hence, the WPP is initially in islanding operation, then the DRU ac-filters are connected and finally the off-shore ac voltage is ramped-up until the DRU starts conducting and rated power is delivered through the HVDC link.

D3.7 Test case	4.2.1. HVDC LINK AND OFF-SHORE AC-GRID START-UP OPERATION		
	Configuration (connected strings)	Compliance	Comments
Simulations (sensitivity analysis)	6 Strings +1 OWF + 1 OWF	pass	$P_{TOT}= 1200$ MW; WTG (max values): $V= 1.0pu$; $I= 1.0pu$; $P_{WT}= 1.05 pu$; $Q_{WT}= -0.45 pu$;
	6 Strings +1 OWF + 0 OWF	pass	$P_{TOT}= 800$ MW; WTG (max values): $V= 1.0pu$; $I= 1.0pu$; $P_{WT}= 1.05 pu$; $Q_{WT}= -0.52 pu$;
	6 Strings +0 OWF + 0 OWF	pass	$P_{TOT}= 400$ MW; WTG (max values): $V= 1.0pu$; $I= 1.0pu$; $P_{WT}= 1.05 pu$; $Q_{WT}= -0.49 pu$;
	3 Strings +0 OWF + 0 OWF	pass	$P_{TOT}= 192$ MW; WTG (max values): $V= 1.0pu$; $I= 1.0pu$; $P_{WT}= 1.05 pu$; $Q_{WT}= -0.43 pu$;
Comments	The results are similar to the presented in deliverable D3.7 of WP3 [16]. The main difference is that in this case the filters are connected automatically depending of the power demand by the WPP control.		

To deliver active power to the DC link, the following steps are carried out:

As a first step, the DR passive filters are connected (capacitor and harmonic filter banks), introducing a demand of reactive power that the wind turbines automatically compensate. Once the filters are connected, the off-shore ac-grid voltage is ramped up and rated active power transmission is reached in about 200ms. Ramping up time would be much longer in an actual system. However, such a fast ramp rate allows to check possible interaction between wind turbine and on-shore MMC converter control. In this case, the fast active power ramp rate causes the MMC voltage controller to inject a large amount of reactive power during the transient. Nevertheless, both MMC voltage and current remain within its operation limits.

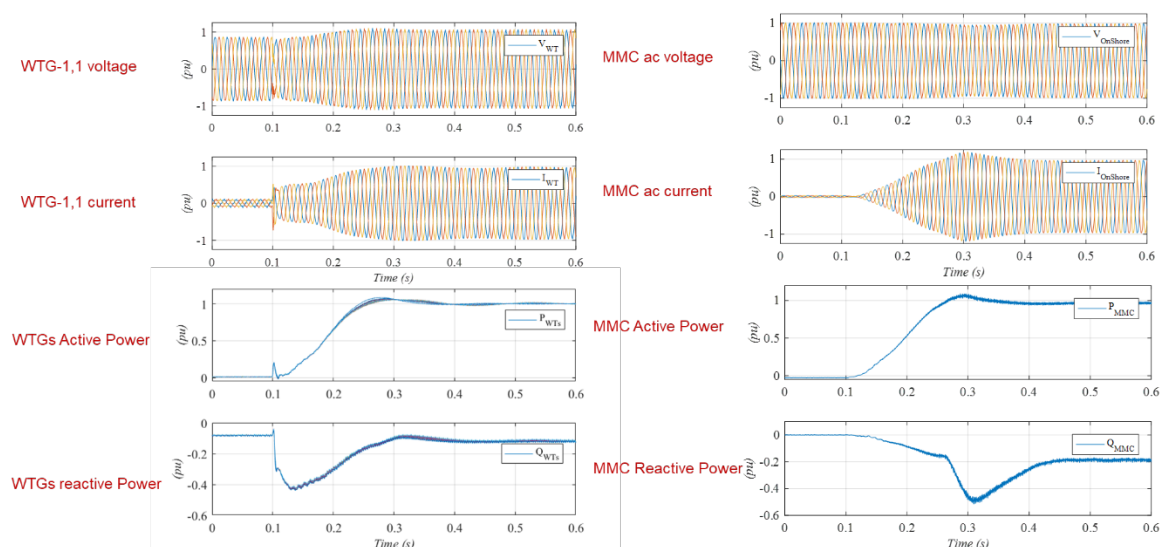


Figure 4-21: Filter connection and operation.

4.3.5 INTENTIONAL ISLANDING

This test case validates the capability of the WPP to stop power transmission. Initially, it is assumed that the diode rectifier is conducting, and active power is being delivered through the HVDC link. At the end of this test case, the WPP is operating in island mode. In this test case the disconnection of the DRU filters is also validated.

D3.7 Test case	4.2.3.a INTENTIONAL ISLANDING		
	Configuration (connected strings)	Compliance	Comments
Simulations (sensitivity analysis)	6 Strings +1 OWF + 1 OWF	pass	$P_{TOT} = 1200$ MW; WTG (max values): $V = 1.03$ pu; $I = 1.0$ pu; $P_{WT} = 1.01$ pu; $Q_{WT} = 0.32$ pu;
	6 Strings +1 OWF + 0 OWF	pass	$P_{TOT} = 800$ MW; WTG (max values): $V = 1.01$ pu; $I = 1.0$ pu; $P_{WT} = 1.0$ pu; $Q_{WT} = 0.19$ pu;
	6 Strings +0 OWF + 0 OWF	pass	$P_{TOT} = 400$ MW; WTG (max values): $V = 1.01$ pu; $I = 1.0$ pu; $P_{WT} = 1.0$ pu; $Q_{WT} = 0.11$ pu;

	3 Strings +0 OWF + 0 OWF	pass	$P_{TOT}= 192$ MW; WTG (max values): $V= 1.02$ pu; $I= 1.0$ pu; $P_{WT}= 1.0$ pu; $Q_{WT}= 0.11$ pu;
Comments	The results are similar to the presented in deliverable D3.7 of WP3 [16]. The main difference is that in this case the filters are disconnected automatically depending on the active power generation by the WPP control.		

Figure 4-22 shows a result corresponding to the case with all wind turbines connected. Once the WPP receives the command to stop power transmission, the DRU ac-side filters are disconnected. The reactive power produced by the filters is initially delivered by the wind turbines. When the ac-grid voltage is reduced, the diode rectifiers stop conducting. The complete transient lasts for about 150ms. Once the diode rectifiers are not conducting, the reactive power demand is reduced to less than 0.1pu.

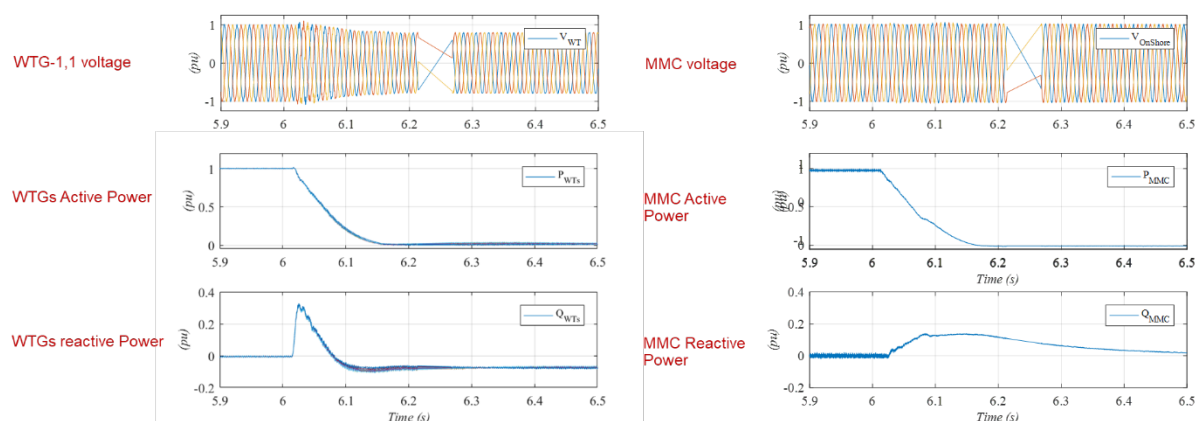


Figure 4-22: From connected to islanded operation.

4.3.6 OFF-SHORE AC FAULTS (RING BUS FAULT)

This test case validates the performance of the WPP when a ring bus fault occurs. The fault is cleared after 200ms.

D3.7 Test case	4.3.3.a SYMMETRICAL OFFSHOREAC FAULT		
	Configuration (connected strings)	Compliance	Comments
Simulations (sensitivity analysis)	6 Strings +1 OWF + 1 OWF	pass	$P_{TOT}= 1200$ MW; WTG (max values): $V= 0.98$ pu; $I= 0.38$ pu; $P_{WT}= 0.08$ pu; $Q_{WT}= -0.35$ pu;
	6 Strings +1 OWF + 0 OWF	pass	$P_{TOT}= 800$ MW; WTG (max values): $V= 0.98$ pu; $I= 0.43$ pu; $P_{WT}= 0.1$ pu; $Q_{WT}= -0.42$ pu;
	6 Strings +0 OWF + 0 OWF	pass	$P_{TOT}= 400$ MW; WTG (max values): $V= 0.97$ pu; $I= 0.59$ pu; $P_{WT}= 0.14$ pu; $Q_{WT}= -0.51$ pu;

	3 Strings +0 OWF + 0 OWF	pass	$P_{TOT}= 192 \text{ MW};$ WTG (max values): $V= 0.96\text{pu}; I= 0.72\text{pu};$ $P_{WT}= 0.19 \text{ pu}; Q_{WT}= -0.64 \text{ pu};$
Comments	As the results presented in deliverable D3.7 of WP3 [16], the export cable energisation cannot be carried out with 1 string because there is not enough reactive power to do it.		

Figure 4-23 shows the behaviour of the WPP during a ring-bus fault. Wind turbine converter current reaches about 1.5pu for less than 2 ms, which is within the overcurrent capability of many standard high power IGBTs. Once the fault is cleared, the wind turbines recover full power production in about 30ms. The on-shore MMC controllers are slower than the wind turbine controllers and there is a small dc-link overvoltage (0.15pu) that takes about 100ms for the MMC to reduce back to 1.pu. During the interval the MMC cannot control the dc-link voltage due to the fast active power rate, the HVDC cable voltage is indirectly limited by the wind turbines. In any case, fault recovery ramp rate can be selected for a smoother recovery, where the MMC controls are capable of controlling the HVDC voltage during the complete transient.

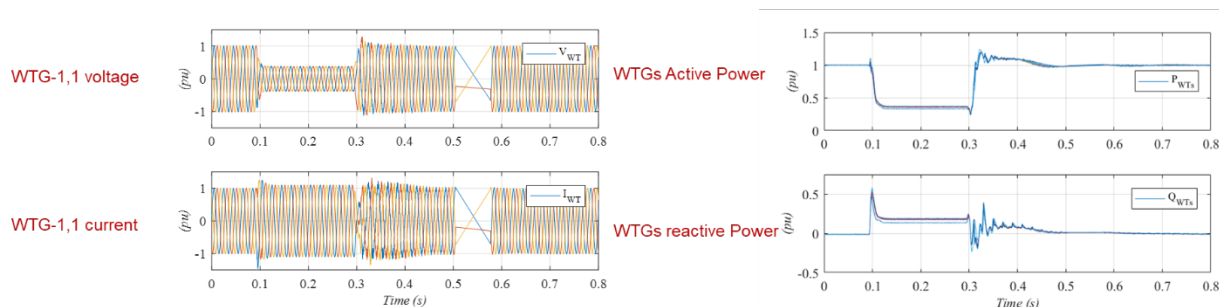


Figure 4-23: Response to a ring bus cable fault.

4.3.7 DISCUSSION

This section has included the Control Hardware-in-the-loop compliance evaluation of grid forming controllers for DRU operation. The requirements and test cases are based on those included in D3.1 and D3.4 [17, 19]. The procedure has been used to validate generic DRU controllers in normal operation, transition between operational modes and during faults.

Interactions between wind turbines have been identified, particularly during synchronisation or during fault recovery. To identify such interactions, a sufficiently large number of wind turbine generators need to be considered for real time controller compliance evaluation.

The test cases include relatively large active power ramp-rates, to highlight possible interactions between the wind power plant controllers and the on-shore MMC converter.

Relatively fast fault recovery has been shown, even when using a large number of wind turbines.

Finally, the CHIL compliance evaluation procedure carried out on the considered controllers has contributed towards increasing the TRL of grid forming wind turbine and wind power plant controllers for diode rectifier and black start applications.



5 STABILITY ANALYSIS IN OFFSHORE NETWORKS

5.1 INTRODUCTION

Being dominated by power electronics and components relying on complex control systems, offshore networks have been proven to be prone to control-system induced oscillations, threatening the system stability in non-fault situations [20, 21]. While in the literature the term harmonic stability is often used to describe this phenomena [21, 22], the importance and the impact of power electronics on system stability in general is also recognized by the IEEE, resulting in an extension of the stability classification in which the stability phenomena is referred to as converter-driven stability and fast interactions [23].

A promising approach is to investigate this stability phenomenon in the frequency domain, having significantly lower computation times and less modelling effort compared to EMT time-domain simulations [22, 24]. Frequency-domain investigations require to model the converter as frequency-dependent impedance which can be either derived analytically or directly measured. Published analytical AC-side impedance models have been investigated in [25]. While analytical models provide great insight into the converter behaviour and potential instabilities, they require detailed knowledge of the converter and its control system. In addition, analytically modelling MMC impedances can be challenging when investigating pre-existing MMC control systems consisting of numerous control loops and discrete control behaviour. As a result, for the AC side measurement-based impedance models are derived in PROMOTioN for the MMC and wind turbine converter. The models are used for the stability test cases defined in [1] and subsequently presented in this deliverable. In addition, a linear frequency-domain analytical model based on harmonic linearization is derived to represent the DC side impedance of a MMC. The model allows for a direct insight on how the different controls affect the impedance of the MMC.

Two test cases are conducted in this chapter, assessing the stability in offshore networks due to converter control interactions in the frequency domain by means of the impedance-based stability criterion [26]. While the offshore test case assesses the stability of a grid forming MMC and an offshore wind farm in the frequency domain, the onshore test case determines the stability of a grid following MMC and AC grid both in time and frequency domain. In addition to the stability assessment, the two test cases serve two different objectives:

- Demonstrating how the impedance-based stability criterion can be used to facilitate a stability assessment when potentially interacting components are not owned by the same party and internal information of the components cannot be shared. For this purpose, the offshore test case utilizes the scaled up impedance measurement of the MMC Test Bench by RWTH Aachen University and that of the 1 MW wind turbine control replica by DNVGL.
- Validating the impedance-based stability criterion along with the measurement-based approach used in this deliverable. The full-scale model of the MMC Test Bench is used in the onshore test case and the stability prediction by the impedance-based stability criterion is verified by comparing the results with those of time-domain simulations in Matlab Simulink.



A comparison of the MMC-Test Bench impedance with the simulated lab-scale as well as full-scale MMC impedance can be found in [2] and [27].

5.2 MMC IMPEDANCE DERIVATION METHOD

5.2.1 DC SIDE IMPEDANCE

Using a combination of the harmonic linearization method and the frequency domain representation, a method is developed in [28] to derive the ac-side admittance of an MMC. The method analyses a sufficient number of perturbation frequency components of the individual converter variables while keeping the mathematical complexity of the admittance model at a reasonable amount. Using the developed method, the impact of the produced perturbation frequency components of the converter variables and the control variables (set by the control loops) on the ac-side admittance of the converter is investigated.

By virtue of the method, an analytical model is derived which captures the dc-side impedance of an MMC, seen in Figure 5-1, while incorporating current control strategies. The impedance shaping effect of each control element is then assessed and conclusions are drawn based on the observed impacts. The validity of the mathematical model is verified by experiments on a laboratory-scale MMC prototype at KTH [29].

In order to calculate the dc-side impedance of the converter, a small-signal perturbation is superimposed on the dc-side voltage, i.e.,

$$v_{dc}(t) = v_{du}(t) + v_{dl}(t) + v_p \cos(\omega_p t) \quad (5.1)$$

such that the Fourier coefficient of v_{dc} at the perturbation frequency $V_{dc}(f_p)$ is negligible compared to the dc component of the dc voltage $V_{dc}(0)$.

The dc-side impedance of the converter can then be calculated as $Z_{dc}(f_p) = V_{dc}(f_p)/I_{dc}(f_p)$, i.e., the ratio between the current response to the applied voltage perturbation. To calculate the current response $I_{dc}(f_p)$, the harmonic linearization method is used to evaluate a linear system of equations describing the system at a combination of the perturbation frequency and the steady-state components as seen in Table 5-1 in grey. As steady-state frequencies 0 and $\pm f_1$ are considered (first row), while frequencies $f = (f_p, f_p \pm f_1, f_p \pm 2f_1)$ are assumed as perturbation components (first column).

Table 5-1: Considered frequency components: Perturbation frequencies (first column) are combined with the steady-state components (first row) through addition and subtraction.

	$-f_1$	0	f_1
$f_p - 2f_1$	$f_p - 3f_1$	$f_p - 2f_1$	$f_p - f_1$
$f_p - f_1$	$f_p - 2f_1$	$f_p - f_1$	f_p
f_p	$f_p - f_1$	f_p	$f_p + f_1$
$f_p + f_1$	f_p	$f_p + f_1$	$f_p + 2f_1$
$f_p + 2f_1$	$f_p + f_1$	$f_p + 2f_1$	$f_p + 3f_1$

As for the MMC model, a time averaged dynamic model is adopted which assumes balanced cell capacitances within the arm and neglects the switching operation. Thus, the dynamic equations describing the arm currents are

$$L \frac{di_u}{dt} + Ri_u = v_{du} - v_u - e \quad (5.2)$$

$$L \frac{di_l}{dt} + Ri_l = v_{dl} - v_l + e \quad (5.3)$$

the arm voltages

$$v_{u,l} = n_{u,l} v_{Cu,l}^\Sigma \quad (5.4)$$

and the sum capacitor voltages

$$v_{Cu,l}^\Sigma = \frac{1}{C} \int n_{u,l} i_{u,l} dt + v_{C0}^\Sigma \quad (5.5)$$

where C is the arm capacitance, v_{C0}^Σ the average sum capacitor voltage and $n_{u,l}$ the insertion indices of the upper and lower arms.

Ac-side current control (per-phase based on proportional-resonant controllers and in the dq -frame based on PI controllers) and circulating current control strategies are implemented as seen Figure 5-1, generating respectively, the reference voltages driving the ac-side current and the circulating current. The upper and lower arm insertion indices then, are computed in an open-loop manner considering the control system time delay T_d as

$$n_u(t - T_d) = \frac{v_c^* - v_s^*}{v_d^*} \quad (5.6)$$

$$n_l(t - T_d) = \frac{v_c^* + v_s^*}{v_d^*} \quad (5.7)$$

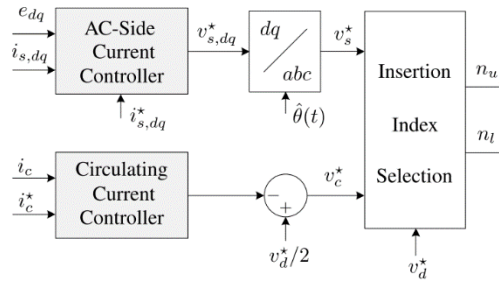


Figure 5-1: Block diagram of an MMC control scheme, dq-frame ac-side current control and circulating current control are applied.

The perturbation components of the MMC variables, i.e., i_u , v_u , $v_{Cu,l}^\Sigma$ and n_u are obtained in linear form at frequencies highlighted in Table 5-1. Due to the symmetry of the MMC topology, it suffices to consider only one arm of one of the phases (in this case upper arm of the phase a). As an example, the perturbation component of the upper arm voltage at f_p is calculated as

$$V_u(f_p) = V_{Cu}^\Sigma(f_p) N_u(0) + N_u(f_p) V_{Cu}^\Sigma(0) + V_{Cu}^\Sigma(f_p - f_1) N_u(f_1) + N_u(f_p - f_1) V_{Cu}^\Sigma(f_1) + V_{Cu}^\Sigma(f_p + f_1) \overline{N_u(f_1)} + N_u(f_p + f_1) \overline{V_{Cu}^\Sigma(f_1)} \quad (5.8)$$

where the overbar denotes the complex conjugate of the said variable.

This process is iterated for all MMC variables i_u , v_u , $v_{Cu,l}^\Sigma$ at frequencies highlighted in Table 5-1, as well as the control variables v_c^* and v_s^* to compute the equations describing the insertion index n_u in the frequency domain at the aforementioned frequencies. Thereafter, a linear system of equations in form of $Ax = B$ is built with A and B

containing the coefficient and constant terms in the derived equations, respectively. Solving the linear system of equations yields $I_u(f_p)$ which due to symmetry of the MMC topology can be utilized to compute $I_{dc}(f_p)$ as $I_{dc}(f_p) = 3I_u(f_p)$. Thus, the dc-side impedance of the converter can be determined by

$$Z_{dc}(f_p) = \frac{V_{dc}(f_p)}{I_{dc}(f_p)} = \frac{V_{dc}(f_p)}{3I_u(f_p)} \quad (5.9)$$

The parameters of the experimental setup and the controller parameters are summarized in Table 5-2 and Table 5-3.

Table 5-2: Parameters of the Experimental Setup

PCC voltage amplitude	e_1	24 V
Fundamental frequency	f_1	50 Hz
Arm inductance	L	3.3 mH
Arm resistance	R	0.55 Ohm
Arm capacitance	C	0.54 mF
Perturbation amplitude	v_p	2 V
Perturbation frequency	f_p	1.67 Hz – 1 kHz

Table 5-3: Controller Parameters

Carrier frequency	f_c	763 Hz
Control system time delay	T_d	65.5 μ s
DC-bus voltage reference	v_d^*	48 V
Active power reference	P^*	-46 W
Reactive power reference	Q^*	0 VAR
AC-side current closed-loop system bandwidth	α_s	1200 rad/s
AC-side current resonant/integral gain	α_1	100 rad/s
PCC voltage feedforward filter bandwidth	α_f	1000 rad/s
Circulating current closed-loop system bandwidth	α_c	500 rad/s
Circulating current resonant controller gain	α_2	100 rad/s

Figure 5-2 shows the Bode diagrams of the dc-side impedance of the MMC for various control schemes. As seen in the figure, the analytical model (solid lines) matches the measurements (dots), proving that the derived analytical model is valid. The following conclusions, e.g., are drawn based on the observations:

- In high frequency region, the arm inductances are the dominant entities setting the converter impedance, whereas in the low frequency region it is the current control loops which shape the impedance;
- The resonant part of the circulating current controller is designed such that it eliminates the second order harmonic component in the circulating current. Therefore, the dc-side impedance of the MMC contains a resonance and phase rotation at 100 Hz;
- The addition of the resonant part of the ac-side current controller (black) significantly increases the impedance magnitude and decreases the phase angle in below fundamental frequencies;

- The addition of the circulating current controller (green) increases the impedance magnitude and phase between 20 Hz and 100 Hz.

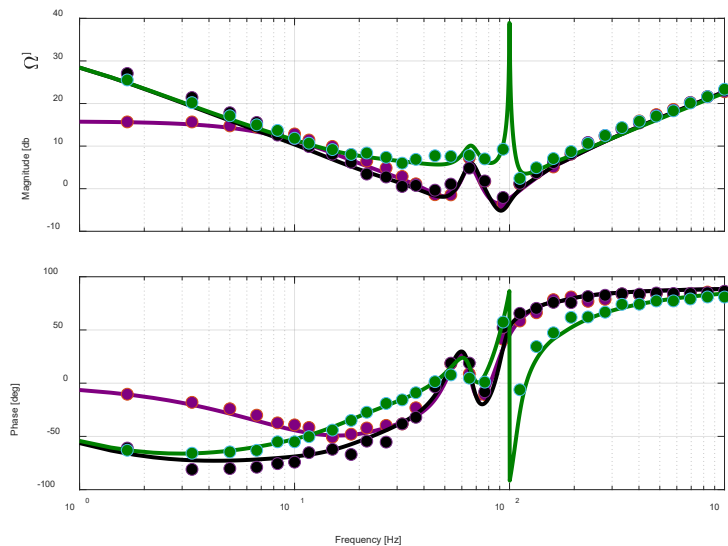


Figure 5-2: Bode diagram of the MMC dc-side impedance for different control schemes: per-phase ac-side current proportional controller (purple); addition of ac-side current resonant controller (black); addition of circulating current PR controller (green). The analytical models are indicated by the solid lines and the measurements with dots

5.2.2 AC SIDE IMPEDANCE

Within WP 16 the frequency-dependent AC side impedances are derived by means of a measurement-based approach so that impedance models can be obtained based on (black-box) time-domain converter models without knowledge of the system under investigation.

A frequency scan method is, thus, developed to measure the MMC impedance in real-time over a specific frequency range. The same method can be applied both to the simulated (without its analytical model knowledge) and to the hardware replica of MMC control systems. The measurement method is developed in such a way that the impedance is determined in real-time at the moment the measurements are taken, without further data post-processing. From a computational point of view, this also avoids the need for large voltage and current highly-sampled signal data storage.

The method is developed with the objective to facilitate converter control interaction studies whilst respecting the manufacturer intellectual property and giving the user full trust into the fidelity of the converter model. The approach of the method is to determine the impedance in real-time at the same time the measurements are taken. This allows the user to directly investigate the impedance during the measurements. In addition, further post processing such as Fourier transformation requiring voltage and current signals to be saved with high sampling rates resulting in large data files, can be avoided [30].

Figure 5-3 shows the principle of the developed methods when coupled with a device under test (DUT).

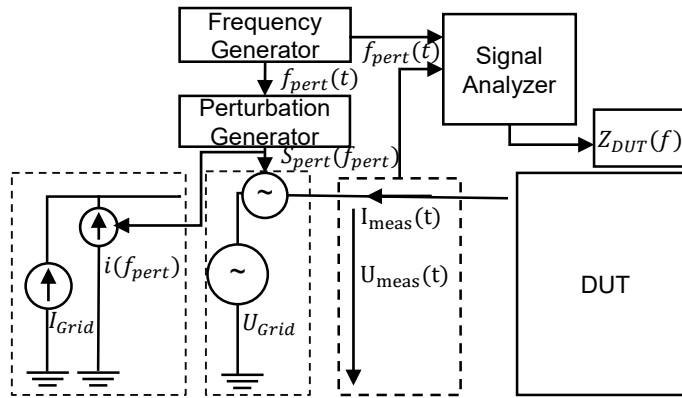


Figure 5-3: Impedance measuring method [30].

The method described relies on a positive and negative sequence approach because derived impedances do not have to be aligned on a common grid angle θ as required by deriving impedances in the dq-frame. The frequency scan method is developed for real-time applications and usable for both simulated models and physical test benches [27]. Figure 5-4 shows the setup developed in PROMOTioN for measuring the impedance of the MMC Test Bench.

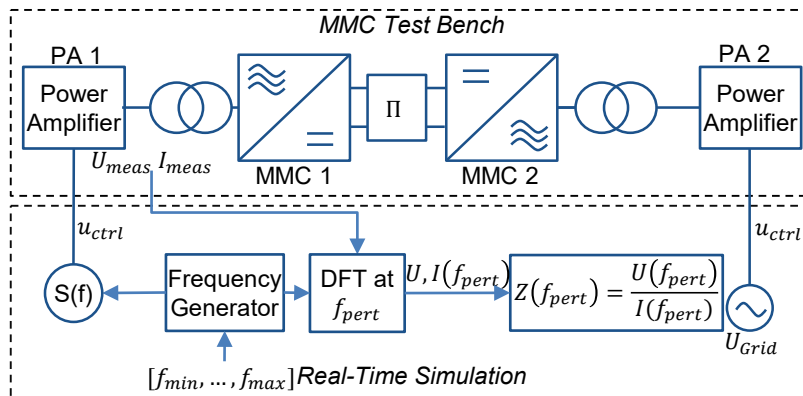


Figure 5-4: MMC Test Bench impedance measurement setup.

Two MMCs are connected on the DC side. While only the impedance of MMC 1 is measurement, MMC 2 ensures a stable operation point on the DC side. In addition, the setup allows for changing the outer control modes (e.g. DC-voltage control to active power control) without having to shut down and restart the system. The MMC-Test Bench is coupled with the real-time simulator via two power amplifiers on the AC side that amplify the signals sent by the real-time simulators via the analogue control voltages u_{ctrl} . While PA 2 supplies the AC grid voltage, PA 1 sets the AC operation point along with the frequency-varying perturbation signals based on the signal $S(f)$. When operating in grid forming control mode, PA 1 provides a current signal as opposed to a voltage signal when operating in grid following control mode. The measured voltage and current signals U_{meas} and I_{meas} are processed

in real-time by a discrete Fourier transform (DFT) to determine the MMC impedance $Z(f_{pert})$ at perturbation frequency.

5.3 AC SIDE MMC IMPEDANCE MODELS

The impedance models used for frequency-domain stability assessment are derived by either measuring the impedance of the MMC Test Bench or the respective MMC full-scale Simulink model as previously described in chapter 5.2. While the MMC full-scale model allows for an additional time-domain validation of the frequency-domain stability assessment in Matlab Simulink, the MMC Test Bench facilitates a stability assessment of real, physical components. However, the MMC Test Bench impedance needs to be scaled up when being used for full-scale stability assessments.

Figure 5-5 shows the impedances that are derived and used for the stability assessment in chapter 5.5 and 5.6.

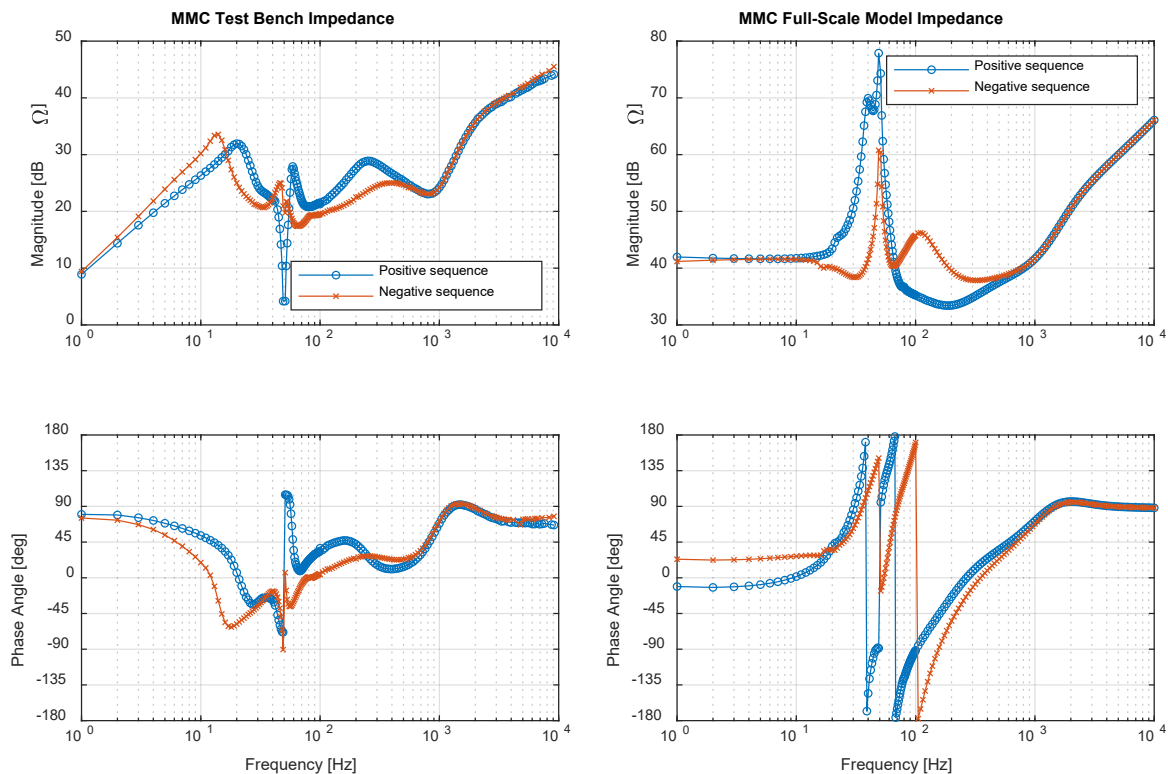


Figure 5-5: Impedance of MMC Test Bench in grid forming control mode for offshore test case (left) and impedance of simulated full-scale model in grid following control mode for onshore test case(right).

A detailed discussion of the MMC Test Bench impedances and a comparison with the simulated lab-scale and full-scale model can be found in [2]. The results show that for frequencies below 1 kHz, the impedance is heavily influenced by the converter control system and the MMC impedance differs in positive and negative sequence. At higher frequencies, positive and negative sequence match as the frequency behaviour is mainly determined by the arm inductance of the MMC.

The impedances are measured by injecting perturbation signals at frequencies ranging from 1 Hz to 10 kHz. Below 100 Hz, the impedance is measured at every integer frequency whereas at higher frequencies logarithmic distances are applied, resulting in a total of 200 measurement points.

The impedance of the MMC Test Bench, operating in grid forming control mode, is measured by injecting a current signal consisting of the fundamental current feeding 3 kW into the grid and the perturbation current having a magnitude of 5 % of the grid current. Simulations have shown that the grid operating point only affects the impedance at 50 Hz when the converter is operating in grid forming control mode. Hence, the measured impedance can be used independent of the power flow for the stability assessment.

The impedance of the simulated MMC full-scale model, operating in grid following control mode and controlling the DC voltage is measured by superimposing a perturbation voltage source with 5 % magnitude of the AC grid voltage on the grid voltage source. Because simulations show that the operating points also affects frequencies close to 50 Hz to a minor degree, MMC 2 of the measurement setup regulates the transmitted AC active power to 800 MW, thus, matching the power output of the offshore wind farm.

5.3.1 IMPEDANCE SCALING

Using the measured MMC Test Bench impedance for assessing the stability of full-scale systems requires scaling of the impedance according to a full-scale converter parameters. Because the control system is in p.u., differences in the impedance depend on the electrical parameters only. Consequently, the electrical parameters of the MMC Test Bench, and its equivalent lab-scale simulation model, as well as the full-scale simulation model are used to calculate a complex correction factor \underline{k} which, when multiplied, scales the MMC Test Bench impedance to the higher voltage level and ratings [27]. The correction factor is divided into $|k|$ and k_φ so that for an impedance $\underline{Z} = |Z|\angle\varphi_Z$, $|Z_{scaled}| = |Z| \cdot |k|$ and $\varphi(Z_{scaled}) = \varphi_Z - k_\varphi$ with

$$|k| = \frac{\sqrt{r_{FS}^2 + (\omega \cdot l_{FS})^2}}{\sqrt{r_{LS,TB}^2 + (\omega \cdot l_{LS,TB})^2}} \quad (5.10)$$

and

$$k_\varphi = \tan^{-1} \frac{r_{FS}}{\omega \cdot l_{FS}} - \tan^{-1} \frac{r_{LS,TB}}{\omega \cdot l_{LS,TB}}. \quad (5.11)$$

The equivalent resistance r_{FS} and inductance l_{FS} are calculated according to the electrical parameters of the full-scale model whereas the resistance $r_{LS,TB}$ and inductance $l_{LS,TB}$ are based on the specifications of the MMC Test Bench and hence, also match those of the lab-scale model. The resulting scaling factors are presented in Figure 5-6. With increasing frequency, $|k|$ converges to six as the impedance is dominated by the inductive parameters, indicating a six times larger magnitude of a full-scale system compared to the lab-scale model and MMC Test Bench. The phase angle of the impedance deviates only slightly due to the fact that the ratio of the inductive and resistive parameters of the full-scale and small-scale system remains similar.

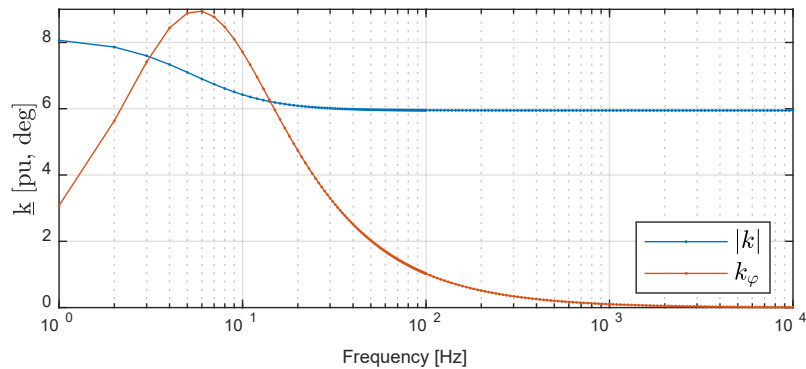


Figure 5-6: Scaling factors $|k|$ and k_φ .

To verify the scaling approach, the impedance of the lab-scale model is scaled up and compared to that of the full-scale model which can be seen in Figure 5-7.

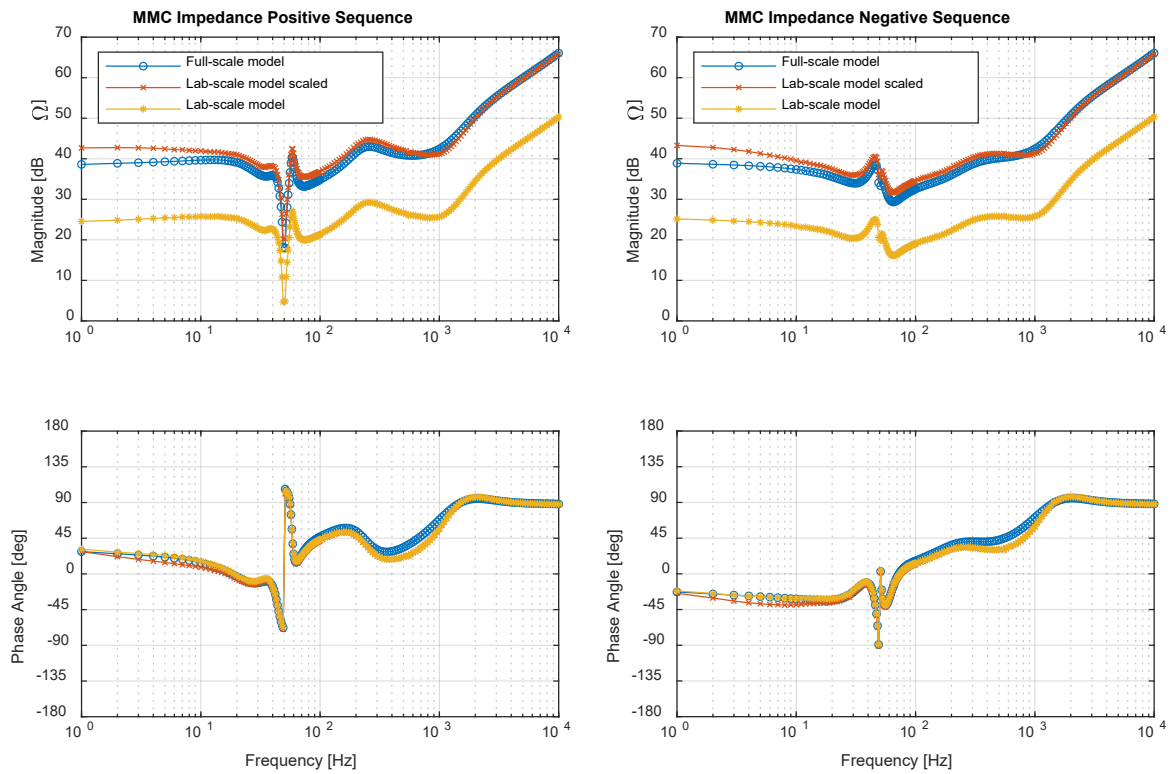


Figure 5-7: Comparison of full-scale model with lab-scaled model and scaled up lab-scaled model.

The comparison shows that the scaling approach is able to shift the magnitude of the lab-scale impedance in regions of the full-scale model, demonstrating that the scaling approach can be applied to scale up the MMC Test Bench impedances for full-scale system stability studies. Larger deviations below 10 Hz do not affect the results as sub-synchronous resonances are not the focus of the investigations

5.4 OWP IMPEDANCE DERIVATION

As a preparatory measure for the frequency-domain-based stability assessment, the framework of the impedance measurements of the MMC and the WTG have been aligned. The OWP impedance was measured in the CHiL and PHiL set-up as documented in [2], the measurement and post-processing were carried out in dq-frame and is shown in for the four component in the 2x2 impedance matrix shown in Figure 5-8. A comprehensive discussion of the results was presented in D16.3 [2].

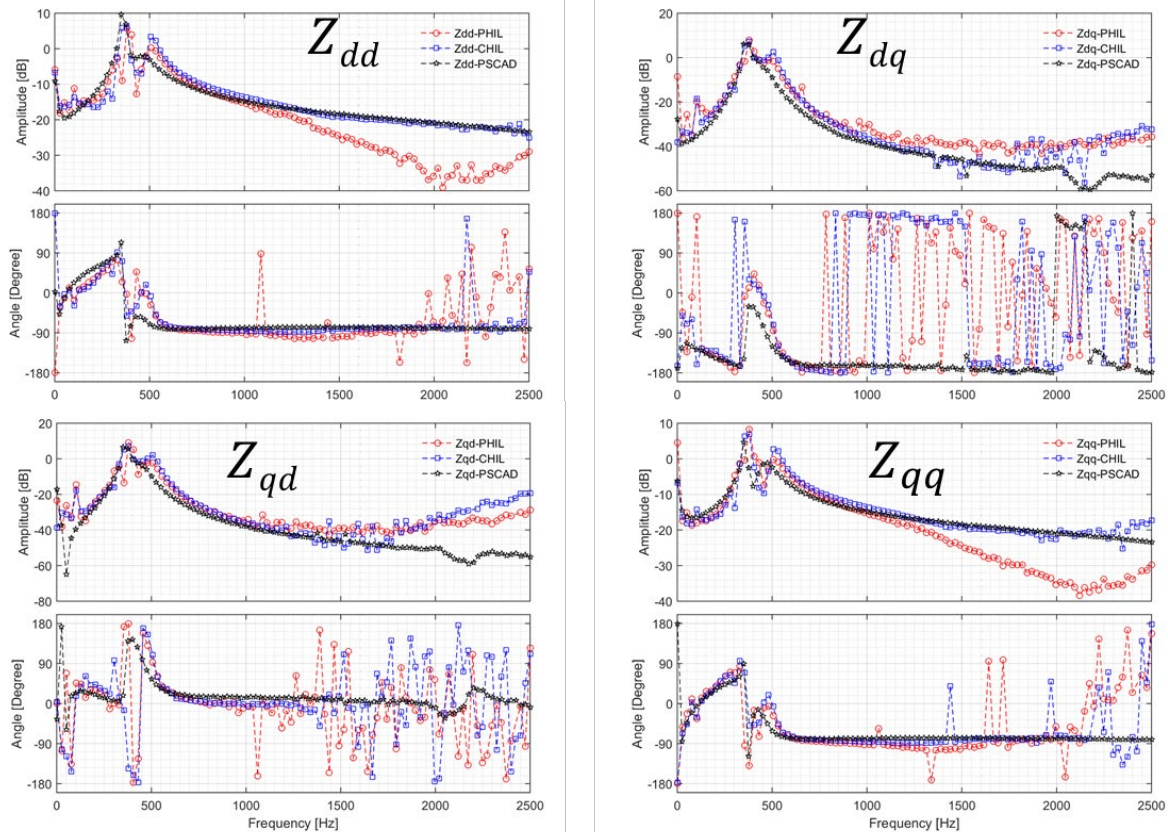


Figure 5-8: Measurement results of the offshore wind turbine impedance in CHiL, PHiL and PSCAD simulation.

The results in dq-frame are first converted into $\alpha\beta$ -frame following the conversion in section 2.3 of D16.5, the impedances in $\alpha\beta$ -frame are further transformed into positive and negative sequences using equation (1.1) and (1.2) presented in D16.5 [25].

The final impedance model of the wind turbine in positive and negative sequence from the CHiL measurement results following the conversion process mentioned above is presented in Figure 5-9. The input data is further processed by removing outliers and smoothing the measurement data. Here PHiL measurement results were not chosen for further analysis as the measurements suffers from various instability issues and measurement noise at frequency band beyond 1200 Hz [2].

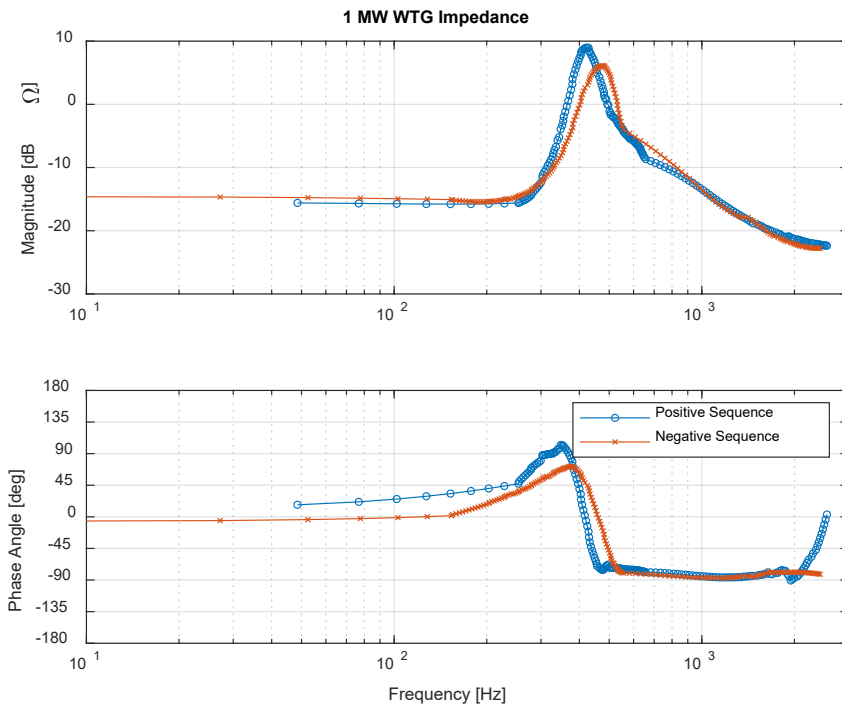


Figure 5-9: Measured control hardware in the loop impedance of 1 MW wind turbine generator.

5.5 STABILITY ASSESSMENT OFFSHORE MMC AND WIND FARM

The first test cases is shown on the right side of Figure 5-10 and investigates the stability of the offshore system due to potential interactions between the offshore MMC and the offshore wind farm. In this test case the MMC is operating in grid forming control mode and provides the voltage magnitude and frequency of the offshore grid on the AC side. The offshore wind farm controls the power output and determines the power flow.

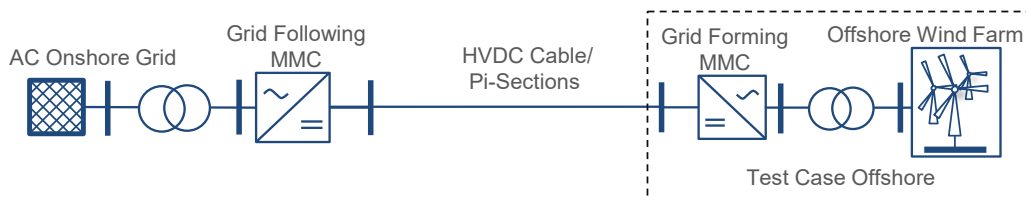


Figure 5-10: Stability analysis between offshore MMC and wind farm.

The nominal power of the MMC is 1.2 MVA whereas one wind turbine has a power output of 1 MW. The layout of the offshore wind farm consisting of the wind turbines is depicted in Figure 5-11. The wind turbines (WT) are arranged in m radial lines, each consisting of n wind turbines.

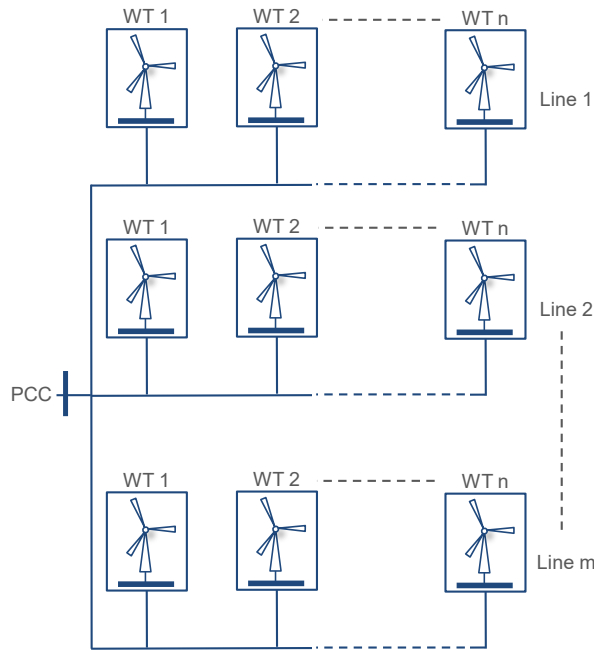


Figure 5-11: Offshore wind farm layout.

5.5.1 FREQUENCY DOMAIN STABILITY ASSESSMENT

The wind farm impedance $Z_{WF}(f)$ seen from the point of common coupling (PCC) can be determined aggregating the wind turbine $Z_{WT}(f)$ impedances into one impedance such that

$$Z_{WF}(f) = \frac{n}{m} \cdot Z_{WT}(f). \quad (5.12)$$

As a result, the offshore system can be represented by an equivalent circuit diagram as shown in Figure 5-12. Operating in grid forming control mode and thus, defining the grid voltage, the offshore MMC is represented by a voltage source in series to an impedance describing the frequency behaviour of the MMC. Controlling the output current and determining the power flow, the offshore wind farm is represented by a current source in parallel to the frequency-dependent wind farm impedance aggregated as described in (5.12).

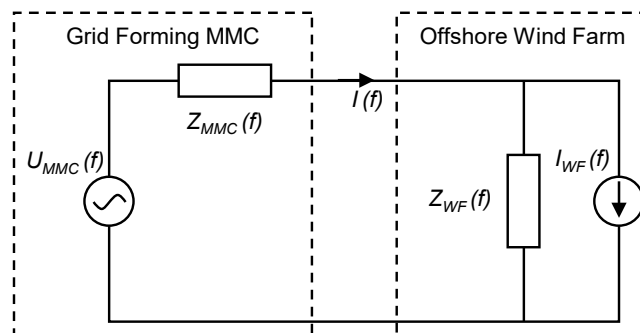


Figure 5-12: Equivalent circuit diagram of test case offshore.

As a result, the representation as an equivalent circuit diagram allows for the application of the impedance-based stability criterion (IbSC) [26]. The principle of the criterion is that a system can be understood as two subsystems interacting with each other. Potential interactions threatening the stability of the system can be subsequently investigated by applying classical control theory such as Nyquist plots and phase margin. Calculating the output current $I(f)$ and rearranging the equation so that

$$I(f) = \left(I_{WF} - \frac{U_{MMC}(f)}{Z_{WF}(f)} \right) \cdot \frac{1}{1 + \frac{Z_{MMC}(f)}{Z_{WF}(f)}} \quad (5.13)$$

Eq. (5.13) shows that the system resembles a negative feedback loop as depicted in Figure 5-13.

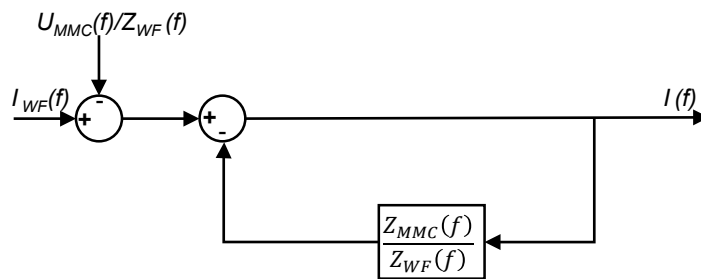


Figure 5-13: Feedback loop representation of equivalent circuit diagram.

Consequently, the phase margin of the subsystem can be calculated indicating how close the system is to instability. The phase margin PM is determined by subtracting the argument of the negative feedback loop for frequencies f_{PM} where the feedback gain is 1 meaning that for the offshore system

$$|Z_{MMC}(f_{PM})| = |Z_{WF}(f_{PM})|. \quad (5.14)$$

The phase margin of the offshore system then yields to

$$PM = 180^\circ - \arg\left(\frac{Z_{MMC}(f_{PM})}{Z_{WF}(f_{PM})}\right) = 180^\circ - \left(\arg(Z_{MMC}(f_{PM})) - \arg(Z_{WF}(f_{PM}))\right). \quad (5.15)$$

Systems having a negative or very small phase margin are predicted to be unstable. This approach makes it possible to utilize impedance data obtained from measurements due to the fact that the phase margin can be determined graphically by plotting both $Z_{MMC}(f)$ and $Z_{WF}(f)$ in one Bode plot.

The positive and negative sequence offshore MMC impedance Z_{MMC} and the wind farm impedance Z_{WF} used for determining the stability in the frequency domain are shown in Figure 5-14 and Figure 5-15, respectively.

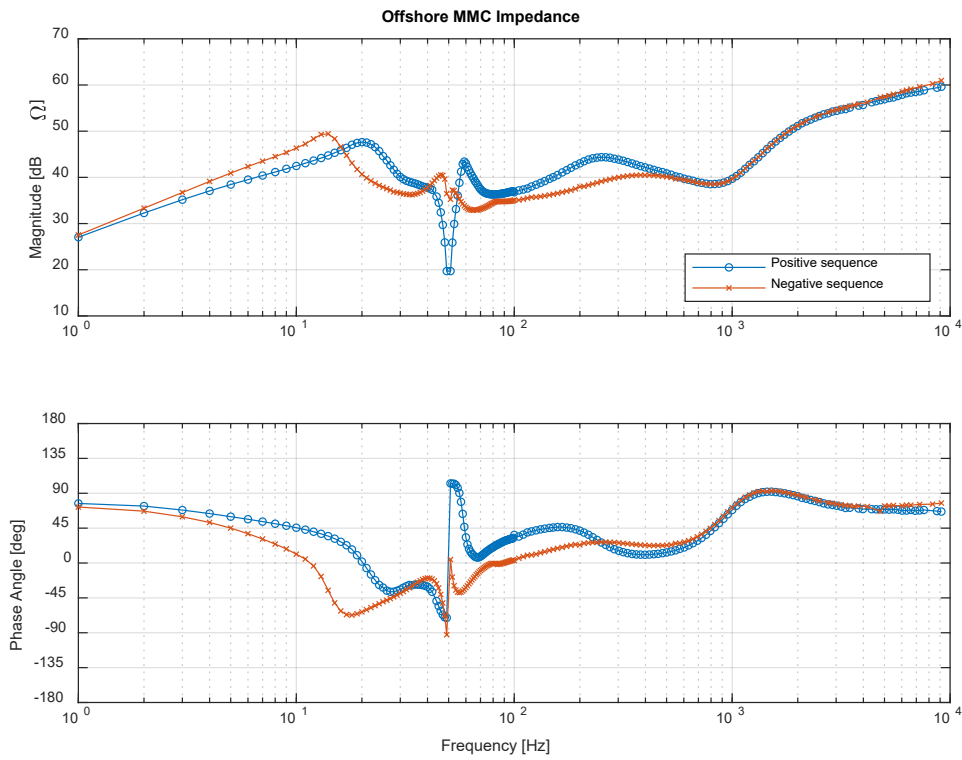


Figure 5-14: Impedance of offshore MMC in grid forming control.

The offshore MMC impedance is derived by measuring the impedance of the MMC Test Bench in grid forming control mode and scaling the impedance as described in chapter 5.3.1 according to a full-scale MMC station.

The depicted wind farm impedance comprises of an exemplarily grid layout of eight radial lines each containing 100 wind turbines. The impedance of a single wind turbine is measured according to the setup described in chapter 5.4.

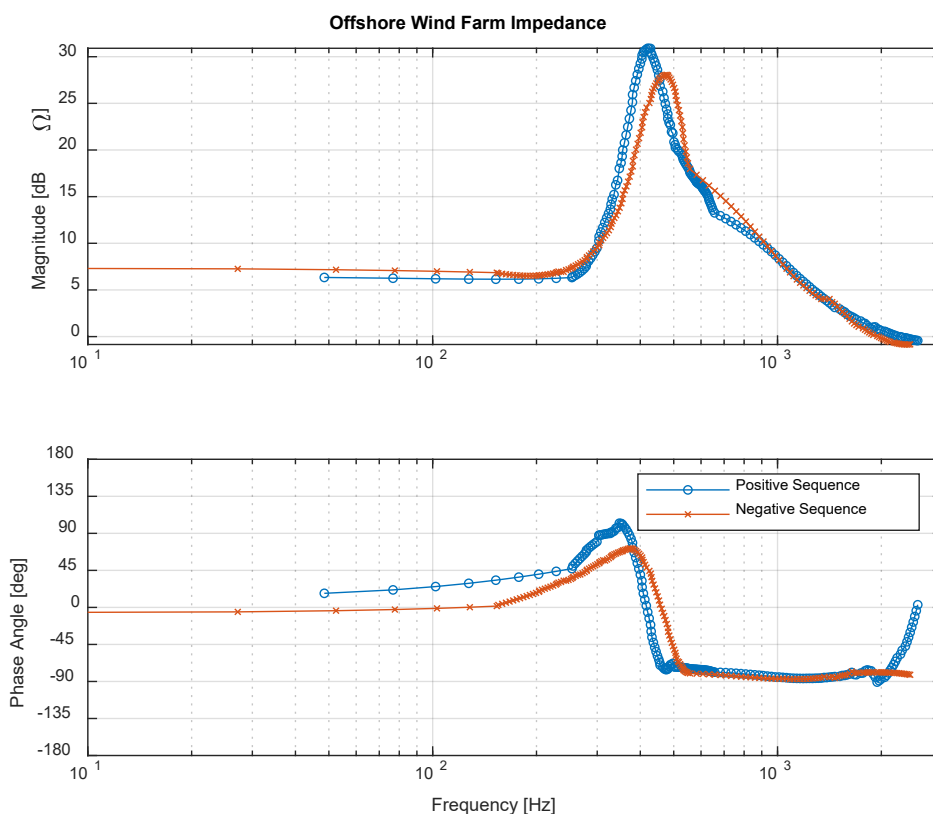


Figure 5-15: Impedance of offshore wind farm with 8 lines and 100 wind turbines each.

While the offshore MMC impedance shows an inductive behaviour at high frequencies, the equivalent wind farm impedance shows a capacitive behaviour, creating a system having a phase difference close to 180 for higher frequencies. Hence, the system is prone to phase margins being close to zero at frequencies above 1 kHz in case of magnitude intersections in that frequency range.

For the stability analysis, interactions of the wind farm and the offshore MMCs are leading to potential instabilities are determined by applying the I_{BSC} and calculating the phase margin of the system for every potential wind farm grid layout including 800 wind turbines.

Figure 5-16 shows the MMC impedance and the wind farm impedance in one Bode in positive sequence as well as negative sequence. The wind farm is depicted for grid layouts of 800 WT in one line (WF_{800,1}), 400 WT in two lines (WF_{400,2}), 200 WT in four lines (WF_{200,4}) and 100 WT in eight lines (WF_{100,8}). Other grid layouts are investigated as well but not presented due to the fact that for these layouts the wind farm and the MMC impedance magnitude do not intersect, thus, leading to an infinite phase margin indicating a highly stable system.

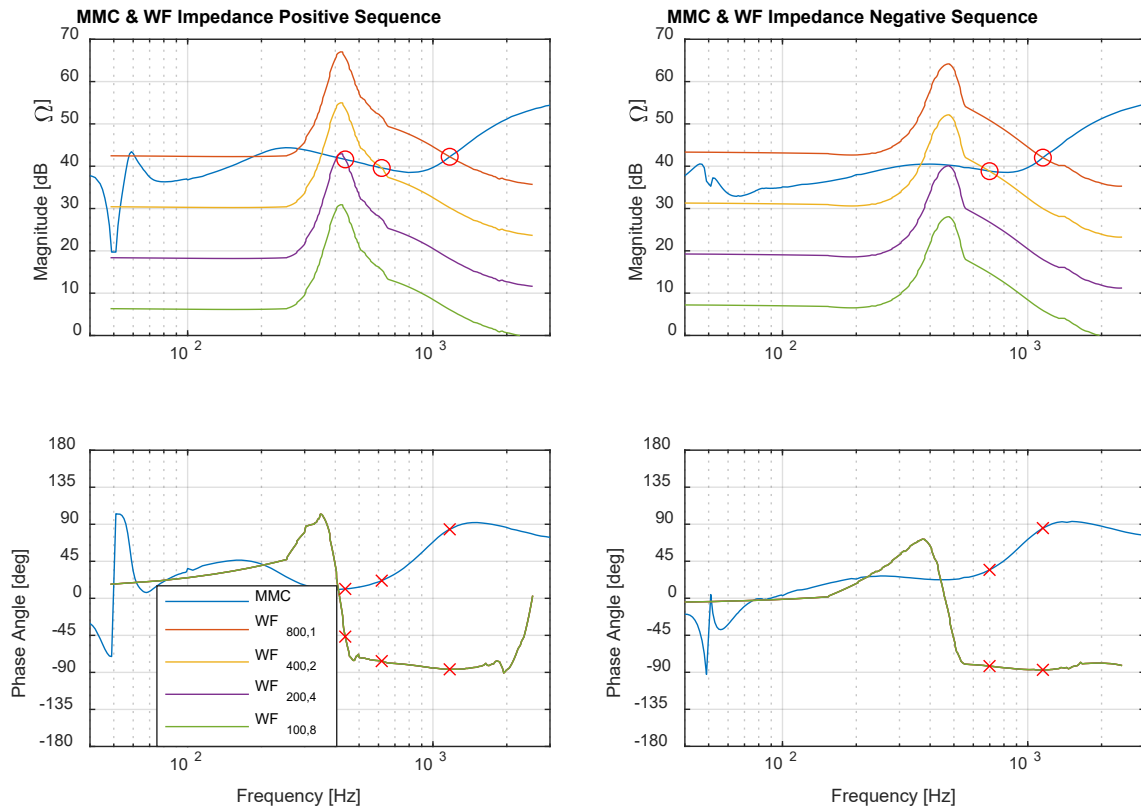


Figure 5-16: Offshore MMC & WF impedance for different offshore grid layouts.

It can be seen that the more WT are placed in one the higher the magnitude of the WF. This is the result of the aggregation method given in (5.12). The results show that a minimum impedance of the WF is required to allow for intersections of the WF and MMC impedance magnitude. Starting with 200 WT in 4 lines, the WF impedance magnitudes intersect with the magnitude of the MMC impedance. Determining the phase difference at the frequencies of the intersection points and calculating the phase margin according to (5.15) results in the phase margins for the different grid layouts that are given in Table 5-4 (positive sequence) and Table 5-5 (negative sequence). For a better overview, only the intersections frequencies at large phase differences are marked in Figure 5-16. Having no intersections, the phase margin of $WF_{100,8}$ in positive and negative sequence and $WF_{200,4}$ in negative sequence are infinite and hence, not presented in the tables.

Table 5-4: Phase margins positive sequence for different offshore grid layouts.

n	m	f [HZ]	PM [deg]						
800	1	61	173	185	173	280	233	1170	10
400	2	53	95	353	270	618	82	-	-
200	4	49	257	51	105	405	196	439	122

Table 5-5: Phase margins negative sequence for different offshore grid layouts.

n	m	f [HZ]	PM [deg]	f [HZ]	PM [deg]
800	1	1153	8	-	-
400	2	366	227	699	63

It can be seen that with a decreasing number of WT in one line, the phase margin of the offshore system decreases with the system with $WF_{100,8}$ having the lowest phase margin of 10° and 8° for positive and negative sequence. This behaviour can be explained by the fact that a higher wind farm impedance moves the magnitude intersection point to higher frequencies. As a result, the phase difference of the wind farm and MMC impedance increases because at higher frequencies the phase of the MMC converges to 90° and that of the WF converges to -90° as it can be seen in Figure 5-16. As a consequence, the higher phase difference leads to a smaller phase margin of the system. The results indicate that for the offshore system, the grid layout plays a crucial role for the stability of the system. Phase margins below 20° can be already considered low enough to lead to an unstable system [31]. In order to verify the frequency domain analysis, the following test case includes an additional time-domain comparison of the results that is not feasible for this test case due to the large number of wind turbines. However, this test case shows that measured impedances allow for a stability prediction of a system in the frequency domain, in particular for systems consisting of components such as the wind turbine and the converter that are not owned by the same party.

5.6 STABILITY ASSESSMENT ONSHORE MMC AND AC GRID

The onshore test case is aimed at investigating the stability of the onshore connection of the offshore network. In addition, by simulating the full-scale Simulink model of the MMC Test Bench in the time domain, the stability predictions made in the frequency domain are verified, demonstrating the validity of the implemented method. Figure 5-17 shows the test case consisting of the AC onshore grid and the connected MMC in grid following control mode.

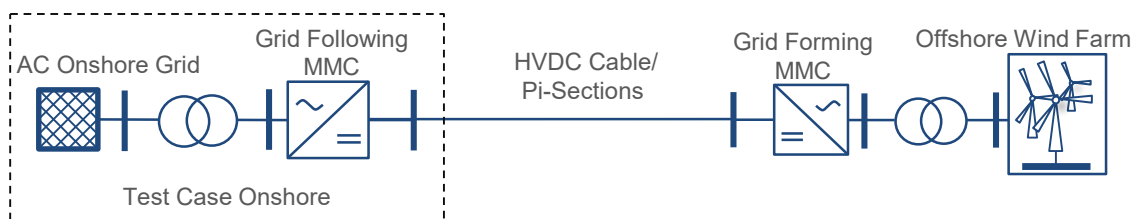


Figure 5-17: Stability assessment test case between onshore AC grid and grid following MMC.

The power transmitted from the offshore to the onshore system is set according to the offshore test system to 800 MW. The AC onshore grid is modelled as a voltage source in series to a resistance R_{Grid} and inductance L_{Grid} that model the short circuit power SC_{Grid} of the onshore grid. The short circuit power of the grid is given relative to the nominal power rating $S_{nom,MMC}$ of the MMC by means of the short circuit ratio (SCR) so that

$$SC_{Grid} = SCR \cdot S_{nom_{MMC}} \quad (5.16)$$

The grid parameters then yield to

$$R_{Grid} = \frac{U_{L,L}^2}{SC_{Grid}} \cdot \frac{1}{\sqrt{1 + XtoR^2}} \quad (5.17)$$

and

$$L_{Grid} = R_{Grid} \cdot \frac{XtoR}{2\pi f_{grid}} \quad (5.18)$$

with $XtoR = X_{Grid}/R_{Grid}$. The parameters used are given in Table 5-6. Applied short circuit ratios range from 1 to 10 where $SCRs \geq 5$ are classified as high, $SCRs < 5$ and > 3 are classified as moderate and $SCRs \leq 3$ are classified as low [32].

Table 5-6: Onshore test case parameters.

PARAMETER	VARIABLE	VALUE
MMC nominal power	$S_{nom_{MMC}}$	1,200 MVA
Transmitted power	P_{MMC}	800 MW
Grid voltage (RMS line-to-line)	$U_{L,L}$	400 kV
Grid frequency	f_{grid}	50 Hz
Short-circuit ratio	SCR	1,...,10
AC Grid short-circuit power	SC_{Grid}	1,200 MVA to 12,000 MVA
X-to-R ratio	$XtoR$	10

The connected AC onshore grid is modelled as an R-L series impedance with different grid strength where a short circuit ratio of $SCR = 4$ is classified as moderate and ratios with $SCR = 5$ and higher are classified as high [32].

5.6.1 FREQUENCY DOMAIN STABILITY ASSESSMENT

The equivalent circuit diagram of the test case is depicted in Figure 5-18. Defining the grid voltage, the AC grid is modelled by voltage source $U_g(f)$ in series to the grid impedance $Z_{g(f)}$ representing the frequency-characteristic of the ac grid as modelled as in (5.17) and (5.18). The onshore MMC, controlling the DC voltage and feeding in the power from the offshore system is modelled as current source $I_{MMC(f)}$ in parallel to the impedance $Z_{MMC(f)}$ which represents the electrical system as well as the control system of the MMC operating in grid following control mode. The MMC is derived as described in chapter 5.2 for a MMC feeding in 800 MW of power to the onshore system.

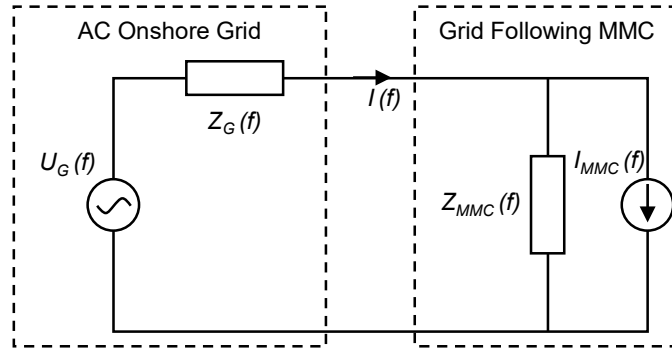


Figure 5-18: Equivalent circuit diagram of test case onshore.

Deriving the output current $I(f)$ to

$$I(f) = \left(I_{MMC} - \frac{U_G(f)}{Z_{MMC}(f)} \right) \cdot \frac{1}{1 + \frac{Z_G(f)}{Z_{MMC}(f)}} \quad (5.19)$$

gives the feedback loop gain $\frac{Z_G(f)}{Z_{MMC}(f)}$ of the equivalent feedback loop system that is depicted in Figure 5-19.

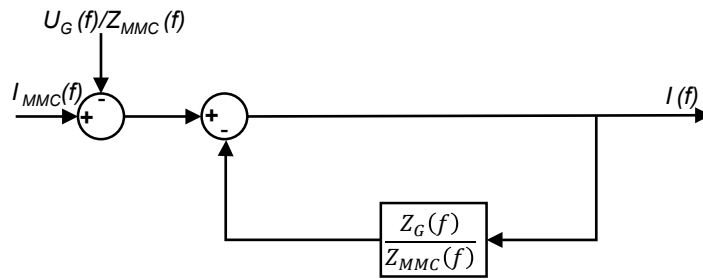


Figure 5-19: Feedback loop representation of equivalent circuit diagram.

The derived loop gain allows for the calculation of the phase margin of the system, facilitating a graphical stability assessment of the onshore test case. The phase margin frequencies f_{PM} are determined by the intersection points of the grid and MMC impedance with

$$|Z_G(f_{PM})| = |Z_{MMC}(f_{PM})|. \quad (5.20)$$

The phase margins then result from the difference in the phase angles of the impedance that is subtracted from 180° so that

$$PM = 180^\circ - \arg\left(\frac{Z_G(f_{PM})}{Z_{MMC}(f_{PM})}\right) = 180^\circ - \left(\arg(Z_G(f_{PM})) - \arg(Z_{MMC}(f_{PM}))\right). \quad (5.21)$$

$$PM = 180^\circ - \arg\left(\frac{Z_G(f_{PM})}{Z_{MMC}(f_{PM})}\right) = 180^\circ - \left(\arg(Z_G(f_{PM})) - \arg(Z_{MMC}(f_{PM}))\right). \quad (5.22)$$

Figure 5-20 and Figure 5-21 show the system from which the phase margins are obtained, for positive and negative sequence and varying short circuit ratios where the lowest SCR results in an unstable system.

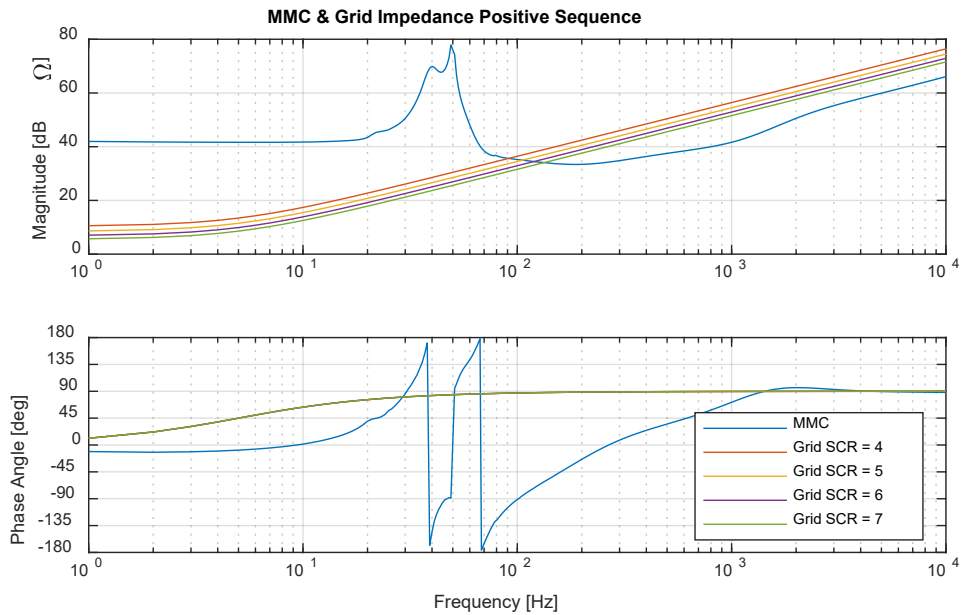


Figure 5-20: Onshore MMC impedance and AC grid impedance for different short circuit ratios.

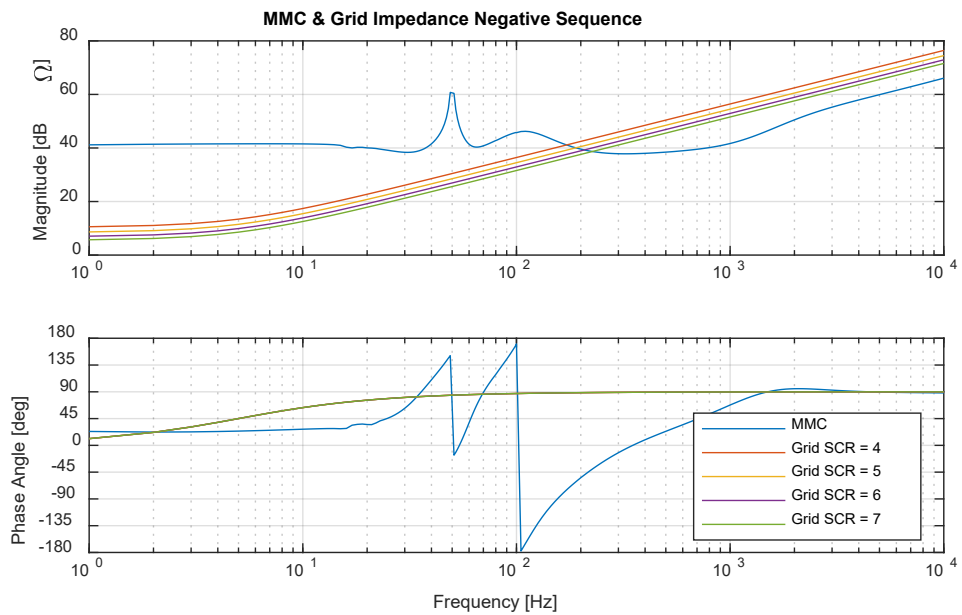


Figure 5-21: Onshore MMC impedance and AC grid impedance for different short circuit ratios.

The depicted Bode plots show that the magnitudes of the grid impedances intersect those of the MMC around 100 Hz for positive sequence and around 200 Hz for negative sequence. Having phase differences close to 180° in these frequency regions, the onshore system is prone to interactions of the MMC and the AC grid that can lead to a potentially unstable system. Figure 5-22 allows for a closer look in these frequency regions. In the figure, intersections of the magnitudes are highlighted by a circle and the corresponding phase values are marked by a cross as well.

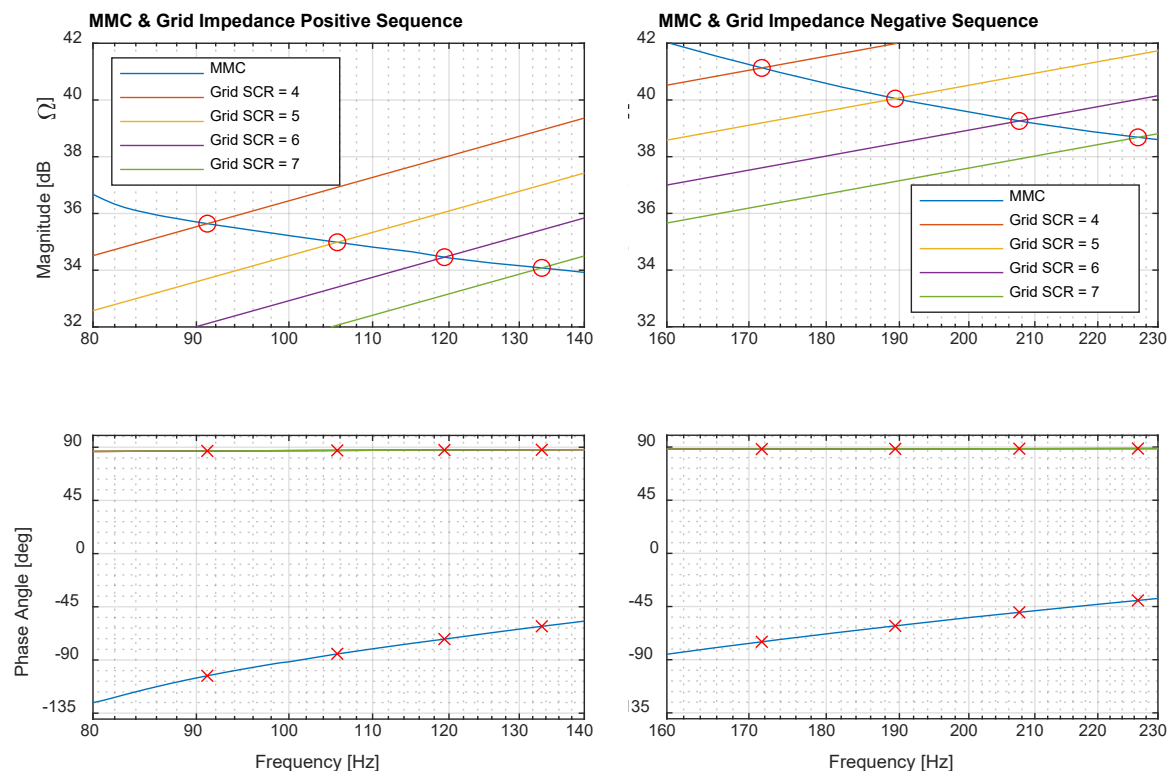


Figure 5-22: Onshore MMC impedances and AC grid impedances for different short circuit ratios.

It can be seen that decreasing SCR move the intersection points of the grid and MMC magnitude to the left and thus, lower frequencies. As the phase angles of the MMC impedance decrease with decreasing frequency, the phase difference of the MMC and the AC grid increases as it can be seen from the phase plots of the Bode diagram. At 91 Hz the phase differences exceed 180° for a $SCR = 4$ in positive sequence and thus, an unstable system is identified. The exact values for the phase margins can be seen in Table 5-7.

Table 5-7: Phase Margins Onshore Test Case

SCR	POSITIVE SEQUENCE		NEGATIVE SEQUENCE	
	f [HZ]	PM [deg]	f [HZ]	PM [deg]
4	91	-10	172	17
5	106	8	189	30
6	119	20	208	41
7	133	31	227	51

The results show that already for a moderate short-circuit ratio of $SCR=4$, the grid connected MMC system becomes unstable. This shows that not insufficiently low AC grid strengths are responsible for the instability, but that the unstable case results from interactions of the MMC and its controllers with the AC grid. To show the validity of the implemented method, the stability predictions will be verified in the time domain.

5.6.2 TIME DOMAIN VALIDATION

The onshore test case is modelled in Matlab Simulink to verify the implemented method and its stability predictions. Figure 5-23 shows the current at the AC terminal of the MMC.

After $t = 4$ s, transients from the MMC startup process can be assumed to have decayed and the MMC is connected to an AC grid with $SCR = 7$. The MMC is then consecutively switched every two seconds to an AC grid with decreasing SCR until an unstable operation point is reached.

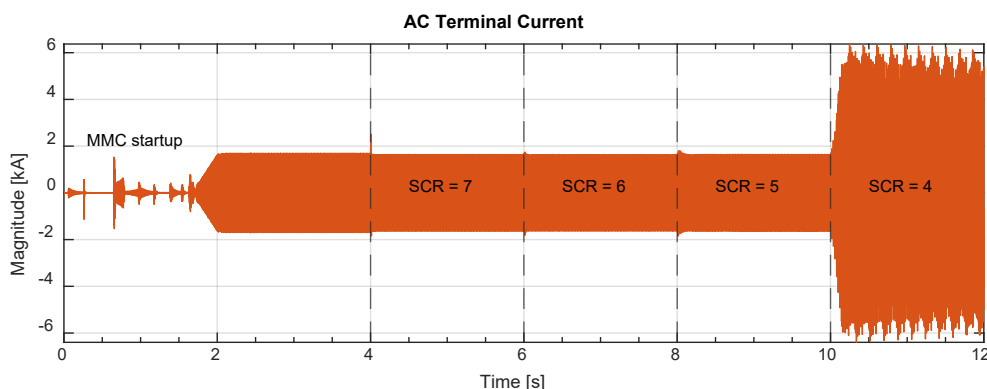


Figure 5-23: AC terminal current when MMC is connected to AC grids with decreasing SCR.

The results show that at $t = 10$ s when the MMC is switched to an AC grid with $SCR = 4$ the current suddenly rises. Looking closely at current in addition to the terminal voltage shows that both terminal current and voltage oscillate at frequencies other than the grid frequency of 50 Hz.

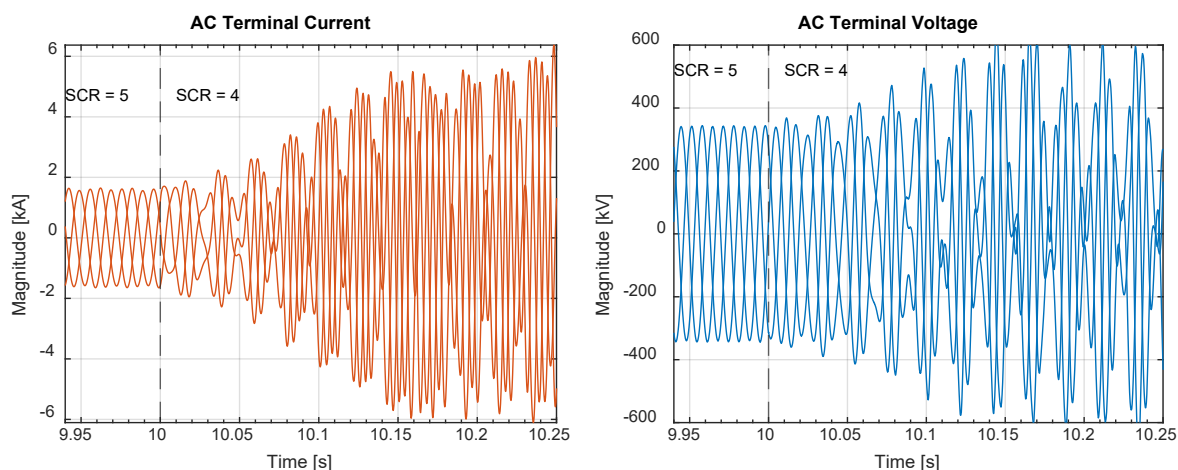


Figure 5-24: AC terminal current and voltage when switched to a grid with $SCR = 4$.

To further identify the frequencies of the observed oscillations the frequency spectrum of the AC current at $t \geq 10$ s is calculated. As it can be seen in Figure 5-25, the current is highly distorted, having a total harmonic distortion of almost 300 %. Thus, it is demonstrated that the case being predicted as unstable by the implemented frequency-domain approach, proves to be an unstable operation point in the time-domain model as well.

Furthermore, the frequency spectrum shows that the signal has the highest magnitude at a frequency of 94.5 Hz which is close to the 91 Hz predicted in the frequency domain. As a result, it can be concluded that the implemented method is not only able to predict the stability accurately, but also the frequency at which instabilities occur can be determined.

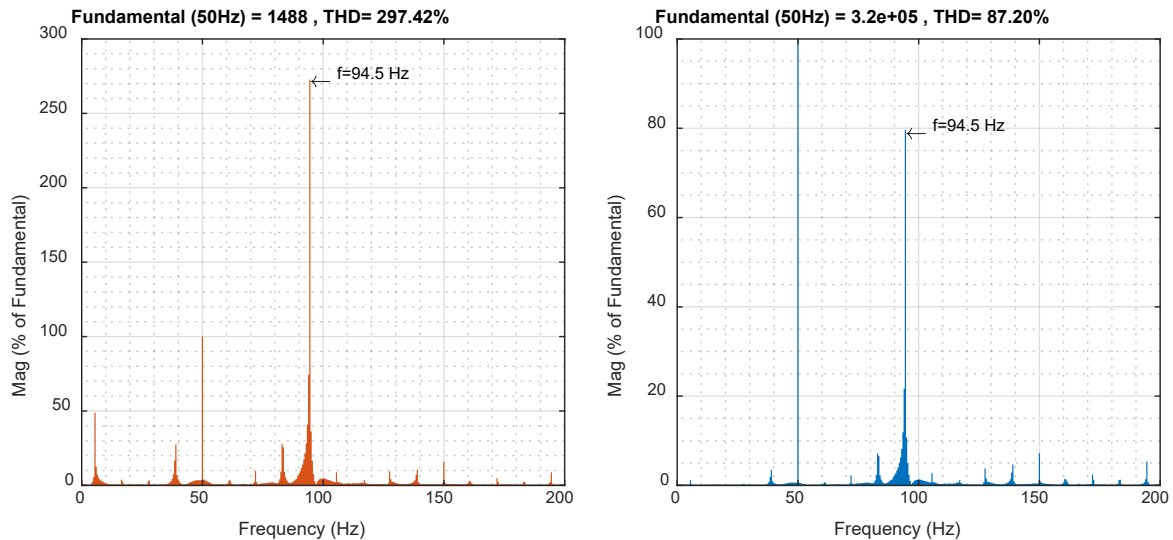


Figure 5-25: Fourier spectrum of AC terminal signals when connected to an AC grid with SCR = 4.

5.7 CONCLUSION

Two test cases were presented assessing the stability of offshore networks in the frequency domain by means of the impedance-based stability criterion. Methods developed in PROMOTiON to derive the converter impedances by perturbing the system and measuring the frequency response are successfully demonstrated on physical converter systems such as the MMC Test Bench at RWTH Aachen University, and the wind turbine control hardware-in-the-loop system at DNVGL Arnhem. While the MMC Test Bench inherently includes physical phenomena potentially not being existing in simulation models, the wind turbine control replica integrates a real manufacturer developed control system.

Comparing the stability predictions in the frequency domain to voltage and current signals from EMT time-domain simulation shows that the impedance-based stability criterion can predict stability and instability correctly as well as the frequencies at which oscillations occur in the measurements as it can be seen in chapter 5.4. This approach enables to conduct stability studies that cannot be simulated easily in time-domain simulations due to computational reasons. For instance, different offshore wind farm grid layouts and their impact on stability can be investigated as shown in chapter 5.5. The test case further utilized the impedances derived independently by RWTH Aachen University and DNVGL demonstrating that the frequency-domain stability assessments offers the possibility to investigate potential interactions of components not owned by the same party.

Deriving the impedance by a measurement-based approach has been proven advantageous when the control system is unknown in case of the wind turbine control replica or when different pre-existing control systems are investigated such as grid forming and grid following controller that are applied on the MMC Test Bench. In addition,

the analytical DC side model presented in chapter 5.2.1 gives insight into the DC side behaviour of an MMC under various control schemes. The developed model provides a straightforward approach into assessing the impact of the individual terms of the controllers on the impedance of the converter. This can be useful, e.g., when assessing the stability of the system by impedance-based stability criteria.

The results of the test cases have further shown that a grid following MMC can interact with the AC grid at moderate short circuit ratios leading to highly distorted AC currents and voltages and a marginally stable system caused by controllers such as the phase-locked loop used for grid synchronization. However, only a simplified AC grid model is applied, modelling the AC transmission grid as a resistive and inductive impedance not representing a real transmission grid.

Furthermore, the stability assessment showed that instabilities can also occur in offshore systems caused by potential interactions of the grid forming MMC and the offshore wind farm and its wind turbine converters. While the system showing the lowest stability margin is not a realistic scenario, the investigation still illustrates that the grid layout of the offshore wind turbines highly influence the stability of offshore wind farms and thus, should be considered in stability analyses.



6 RECOMMENDATIONS

Based on the investigations and demonstration the following recommendations towards grid codes, (compliance) testing and further research are derived within WP16 of the PROMOTioN project:

Utilisation of PHiL for MTDC – OWP Interoperability

The investigations regarding the integration of the offshore wind farms conducted within D16.3 for a steady state with simulated full-scale models, simulated lab-scale models show very close matching of the results with the MMC Test Bench implementation regarding the control interactions of the MMC stations with the OWF controls. Moreover, the investigated network in D16.3 is implemented as a bipolar configuration in this report. The results show a very close matching of the MMC controls between the simulated full-scale model, simulated lab-scale model and the MMC Test Bench. Utilising a PHiL system for demonstration purposes of developed control algorithms and network topologies can be recommended. PHiL systems can be considered a feasible alternative to demonstration of the developed control algorithms and network topologies with a real-life HVDC system. Utilisation of PHiL systems will increase the confidence in the developed technology and controls.

However, the existing PHiL interface algorithms, such as the Ideal Transformer Method or the Damping Impedance Model are not adequate interfaces for the implementation of weak grids, e.g. stable OWF implementation rated at full-scale in a MTDC network in a bipolar configuration. The design and the implementation of an appropriate PHiL interface algorithm for the implementation of weak grids with a PHiL system must be developed. This way, high transient phenomena, such as investigations of the OWF response in case of simulated AC side faults or DC faults can be investigated and the result comparison between a corresponding simulated full-scale system, simulated lab-scale system and a PHiL system, can lead to difference identification between the models and lastly to an improvement on the simulated models, PHiL system as well as it can lead to an increased technological readiness level that can lead to initial recommendations for the respective high transient test cases.

Fault Clearing in MTDC grids

In chapter 3.3, a demonstration of two different MTDC grid protection strategies have been shown: A non-selective strategy using FB-converters and RCBs as well as a fully-selective strategy using fast DC circuit breakers.

Both demonstrations validate the theoretical feasibility of the protection strategies shown in WP4 and have a high degree of consistency with laboratory- and full-scale simulations. According to chapter 2.2.2 the demonstrations are considered successful and there is high confidence that the protection strategies are applicable in a full-scale MTDC grid.

From the results of this demonstration it is concluded, that there are no indications, that the presented protection strategy could not be implemented in a full-scale MTDC grid. Therefore, there is a need to define standardised control interfaces and protection test setups to enable the testing of different protected and black-boxed vendor controls and protection devices. Additionally, further research on the applicability of different RCB types for the presented non-selective fault clearing strategy is recommended.



Recommendations for real time CHiL compliance simulation of grid forming converters

This deliverable showed the real time CHiL validation of grid forming converters for DRU and for black-start operation considering the functional requirements, scenarios and test cases developed in WP3 and included in deliverables D3.1, D3.4 and D3.7. Clearly, scenarios should be adapted for specific cases. Considered models should follow the requirements stated in CIGRE TB563 "Modelling and Simulation Studies to be performed during the lifecycle of HVDC systems" and CENELEC, CLC/TS 50654-1:2020 "HVDC Grid Systems and connected Converter Stations - Guideline and Parameter Lists for Functional Specifications - Part 1: Guidelines" regarding real time models used for compliance evaluation. Additionally, the following minimum requirements for the real time models are important for a reliable controller validation:

- A reasonable number of wind turbines should be considered to identify interaction between them. A reasonable compromise is to consider a detailed string, and then aggregate the rest of the wind farm in a per-string basis.
- Wind turbine back to back converter models should use full PWM models (not average models). If all converters are simulated in the same real time system, then special care should be made so PWM carriers are not synchronised.
- All transformer models should include saturation and residual flux.
- All surge arresters should be included.
- Cable models should be carefully verified so interactions between large transformers and cables are a faithful representation of actual system behaviour.
- Aeroelastic (or, at least two mass) models should be used to include the dynamics of the wind turbine mechanics.

Considerations regarding standardisation and eventual grid code modifications

The recommendations for possible grid code changes regarding DRU connection stated in D3.8 are also applicable here and the results of the real-time CHiL validation do not change the conclusions and recommendations stated in D3.8.

Recently, CENELEC, CLC/TS 50654-1:2020 "HVDC Grid Systems and connected Converter Stations - Guideline and Parameter Lists for Functional Specifications - Part 1: Guidelines" (2020) includes the use of real time simulations during the lifecycle of the HVDC project, in accordance to CIGRE TB563 "Modelling and Simulation Studies to be performed during the lifecycle of HVDC systems". The studies included in this deliverable for the diode rectifier units (type 1 converter stations) are aligned with both CENELEC CLC/TS 50654-1:2020 and CIGRE TB563.

Nevertheless, CENELEC, CLC/TS 50654-1:2020 states that the AC/DC converter station should self-protect against most dc faults and all ac faults. This behaviour is most desirable from a technical point of view. However, the requirement of self-protection should be clarified when grid forming wind power plants are used. Clearly, off-shore WPP grid forming capability can help on the AC/DC converter station protection, where the sending grid is 100% power-electronic based. This is applicable to type 3 and, particularly, type 1 converter stations.

Regarding black-start operation, the considered functional requirements are mainly based on NGESO and Elia requirements on black start operation. During islanding operation, and up to synchronisation to other islands, the WTGs are the only generators in the system and the functional specifications should not be understood as



allowing to trip the wind turbine when they are exceeded. On the contrary, the grid forming wind power plant should actively control the different magnitudes to be kept within the operational limits.

After the real-time controller compliance evaluation results in WP16, the following comments can be made to the original functional requirements in D3.7.

- **Frequency range.** Initial frequency range was 49-52Hz as required by Elia, with NGESO and NC RfG considering larger frequency ranges. When grid forming wind turbines are the only generation equipment in the islanded grid, both WP3 and WP16 results show that this frequency range can be kept even during sequential black start. However, when the system is synchronised to adjacent islands, controlled frequency range should be defined taken also into account the characteristics of the adjacent islands.
- **Voltage range.** Voltage ranges are always kept during soft-start and in a very large percentage of the sequential black-start cases. However, in some cases, cable and transformer energisation can lead to large over-voltages (and over-currents), which would trip the wind turbines. Therefore, detailed sensitivity analysis should be carried out for the energisation of long cables and large transformers. When using PoW switching (even with relatively large timing errors), in most cases, wind turbines would not trip on over-voltage for the considered scenario. However, this conclusion cannot be generalised to all scenarios and detailed studies should be carried out for the specific scenario and energisation sequences.
- **Block load size.** A directly connected resistive block load size of 0.1 pu has been considered for the compliance evaluation studies (representing the auxiliaries of a thermal power station). Frequency deviation and voltage drop seen in the test cases are usually smaller than frequency and voltage deviation due to export cable energisation. However, ramped-up block loads (or sequential connection of block loads of smaller sizes) allow for smaller voltage and frequency transients and for much reduced impact to the wind turbine mechanical drivetrain.

Therefore, WP16 has shown that the considered controllers are compliant with the functional requirements stated in D3.7, however, some requirements should be tailored to the specific scenario and service restoration strategy. Both WP3 and WP16 show that soft-start operation leads to faster service restoration and minimised risk of overvoltage and overcurrent. Therefore, soft-start of the largest possible portion of the grid should be considered when WPP are used for service restoration.

Stability Assessment & Converter Impedance Measurement

The stability assessment presented in chapter 5.5 showed that the control system of MMCs can interact with the AC grid and wind turbine converters resulting in unstable or marginally stable systems. Both the onshore as well as the offshore MMC of an HVDC system connecting offshore wind farms to the shore, can cause oscillations and highly distorted currents and voltages in certain grid situations that threaten the system stability. The investigations show the need for conducting stability studies already in the planning stage of HVDC systems to avoid controller system-induced instabilities.

The impedance-based approach has proven to be a valid and advantageous method to assess the converter-driven stability of offshore networks in non-fault situations. While EMT time-domain simulation are able to assess the converter-driven stability as well, they cannot be used to determine the stability of systems consisting of

multiple converters due to the computational effort. Moreover, the investigation showed that the topology and grid layout of offshore wind farms highly affects the stability and thus, cannot be simplified to one aggregated model. However, frequency-domain analyses using an impedance-based approach rely on linearized models of the components and are therefore only valid for a given operation point. Thus, it is recommended to conduct at least one test case that ensures the validity of the modelling approach and the accuracy of the models used, by comparing the frequency-domain stability assessment to the results of EMT-time domain simulations.

Impedances, representing the converters in the frequency domain can be derived analytically or by measuring the frequency response of a given time-domain model or control replica as well of a physical test bench. Analytical impedance model offers great insight on how control schemes and parameters shape the impedance in certain frequency regions. However, they require detailed knowledge about the converter structure and control system. Thus, the use of analytical models is recommended when developing control systems on the basis of a fully known system. In contrast, measurement-based impedance models can be derived when black-boxed systems such as control replica provided by converter manufacturers are intended to be used for converter-driven stability analyses. In addition, they can be derived on the basis of a given system without extensive modelling effort. Thus, measurement-based impedance models are recommended when assessing the stability of a system where the components are owned by different parties and open models cannot be shared due to intellectual property concerns. Moreover, it is recommended to verify provided models by comparing the model to additional measured impedances to increase the confidence of the provided model as the investigations showed that deviating impedance trajectories can lead to different stability predictions.

Further research is recommended in particular on the AC side grid models due to the fact that investigations showed the impact of the grid topology and grid strength on the stability assessment.



7 SUMMARY AND CONCLUSIONS

One of the main focuses of WP16 within PROMOTioN is to demonstrate the operability of the defined network topologies including the developed control algorithms using different approaches. Therefore, both, simulation models and a down-scaled hardware laboratory, referred to as the MMC Test Bench, are considered.

Special attention is given to the grid-following and grid-forming MMC controls developed within WP2 and WP3 of PROMOTioN as they are the basis for the successful offshore grid operation. The analysis in D16.3 shows, that differences such as the additional resistances for the cable connections between the MMC stations and the corresponding Pi-segments are identified. However, for the demonstration purposes of the MMC controls and the interaction with the OWFs in steady state, these differences can be assumed as negligible. Moreover, investigations on how to reduce these additional resistances must be carried out, so that the transient behaviour of the simulated models and the MMC Test Bench is as close as possible.

Following the demonstration of OWF integration in a MTDC network using the MMC Test Bench in D16.3, in this deliverable, the 4-terminal network topology developed within WP2 is implemented as a bipolar network configuration. Initially, the model is implemented as a simulated full-scale model, simulated lab-scale model where the system parameter specification corresponds to the MMC Test Bench specifications, and lastly the investigated network is implemented with the MMC Test Bench. The control of the MMC stations in voltage and active power control mode are demonstrated. It is shown that the results of the simulated models and the MMC Test Bench have a high degree of consistency. The implementation of weak networks in a MTDC network, such as a fully-rated OWF in the aforementioned 4-terminal bipolar configuration, using the Ideal Transformer Method and Damping Impedance Method has proven not to work properly as the system becomes unstable. A suitable PHiL interface algorithm has to be investigated and implemented, such that integration of weak grids as well as investigations regarding the OWF response in a case of an AC or a DC fault in a MTDC network utilising the MMC Test Bench can be carried out. Following the demonstration of the 4-terminal bipolar network configuration for the steady state case using the MMC Test Bench, two different fault-handling approaches are investigated in this deliverable. Using a point-to-point bipolar network, a non-selective fault clearing method based on fault blocking converters is demonstrated using the MMC Test Bench. Furthermore, a fault separation based on fast DC circuit breakers in a MTDC network is demonstrated using the MMC Test Bench. For the investigated fault-handling methods, initially the corresponding simulated full-scale model and the simulated lab-scale system are implemented and then the results are compared to the MMC Test Bench. The results show a high degree of conformity of the simulated models and the MMC Test Bench, proving that the developed fault-handling concepts work with a PHiL implementation leading to an increase in the respective technology readiness level.

The MMC control, which has been developed for the converter control of the MMC Test Bench, has been extended by the unidirectional communication less frequency support control developed in WP2. No unintended interaction with the MMC control could be observed and the considered scenarios show the expected unidirectional communication less frequency support. Therefore the investigated RMS simulations in the frame of WP 2 can be confirmed. Using a setup as the MMC Test Bench, (commercial) external frequency support controllers can be tested regarding their functionality and interaction with MMC controls.



This deliverable showed the real time CHIL compliance evaluation of grid forming converters for DRU and for black-start operation considering the functional requirements, scenarios and test cases developed in WP3 and included in deliverables D3.1, D3.4 and D3.7. The procedure has been used to validate generic DRU controllers in normal operation, transition between operational modes and during faults.

Moreover, interactions between wind turbines have been identified, particularly during synchronisation or during fault recovery. To identify such interactions, it is shown that a sufficiently large number of wind turbine generators need to be considered for real time controller compliance evaluation.

Based on the compliance evaluation tests, recommendations regarding the real-time modelling of directly connected and DRU-connected are formulated. Moreover, considerations regarding standardisation and eventual grid code modifications are given.

The impedance measuring methods developed in PROMOTioN are successfully applied on two demonstrators: The MMC Test Bench laboratory at RWTH Aachen and the wind turbine control replica system at DNV GL, Arnhem. The derived impedances are used to investigate potential instabilities due to converter control interactions in non-fault situations in offshore networks in the frequency domain. Using the digital twin of the MMC Test Bench, the frequency domain stability assessment is validated by comparing the stability predictions by means of the impedance-based approach with the results of EMT time-domain simulations. Due to insignificant computation times, the frequency-domain assessment enables to assess the stability of multiple grid situations showing that the offshore wind farm layout as well as the grid strengths of the connected onshore AC grid are crucial for the stability in offshore networks. Moreover, the investigation results reveal that the measurement-based approach does not require the exchange of sensible models and component data, enabling stability and interaction studies of systems not owned by a single entity.



8 REFERENCES

- [1] PROMOTioN WP16, “Deliverable 16.1: Definition and Specification of Test Cases,” Jun. 2018. [Online]. Available: https://www.promotion-offshore.net/fileadmin/PDFs/D16.1_Definition_and_Specification_of_Test_Cases.pdf
- [2] PROMOTioN WP16, “Deliverable 16.3: Overview of the conducted tests, the results and the associated analyses with respect to the research questions and analyses within WP3,” Feb. 2020. [Online]. Available: https://www.promotion-offshore.net/fileadmin/PDFs/D16.3_Overview_of_the_conducted_tests_the_results_and_the_associated_analyses_with_respect_to_the_research_questions_and_analyses_within_WP3.pdf
- [3] J. Freytes, S. Akkari, J. Dai, F. Gruson, P. Rault, and X. Guillaud, “Small-signal state-space modeling of an HVDC link with modular multilevel converters,” in *2016 IEEE 17th Workshop on Control and Modeling for Power Electronics (COMPEL)*, Trondheim, Norway, Jun. 2016 - Jun. 2016, pp. 1–8.
- [4] J. Beerten*,†, S. D’Arco‡, J.A. Suul†,‡, “Cable Model Order Reduction for HVDC Systems Interoperability Analysis,”
- [5] W. Ren, M. Steurer, and T. L. Baldwin, “Improve the Stability and the Accuracy of Power Hardware-in-the-Loop Simulation by Selecting Appropriate Interface Algorithms,” in *2007 IEEE/IAS Industrial & Commercial Power Systems Technical Conference*, Edmonton, AB, Canada, May. 2007 - May. 2007, pp. 1–7.
- [6] CIGRE Working Group B4/B5.59, *TB 739: Protection and Local Control of HVDC-Grids*. Paris: CIGRÉ, 2018.
- [7] PROMOTioN WP 4, “Deliverable 4.6: Functional HVDC protection IED including documentation,” non-public, Dec. 2018.
- [8] G. Chaffey *et al.*, “Requirements for functional testing of HVDC protection IEDs,” in *Proc. CIGRE Colloq*, Johannesburg, 2019, pp. 1–12. [Online]. Available: [Uhttps://lirias.kuleuven.be/retrieve/548996DRRequirements for functional testing of HVDC protection IEDs - 2019 - Lirias version.pdf](https://lirias.kuleuven.be/retrieve/548996DRRequirements%20for%20functional%20testing%20of%20HVDC%20protection%20IEDs%20-2019) [freely available]
- [9] I. Cowan *et al.*, “Demonstration of Partially Selective HVDC Grid Protection System with Hardware-in-the-loop HVDC Protection IEDs,” in *Proc. IET DPSP*, Liverpool, 2020.
- [10] M. Wang *et al.*, “Multi-vendor interoperability tests of IEDs for HVDC grid protection,” in *Proc. IET DPSP*, Liverpool, 2020.
- [11] I. Jahn, F. Hohn, G. Chaffey, and S. Norrga, “An Open-Source Protection IED for Research and Education in Multiterminal HVDC Grids,” *IEEE Trans. Power Syst.*, vol. 35, no. 4, pp. 2949–2958, 2020, doi: 10.1109/TPWRS.2020.2970477.
- [12] PROMOTioN WP 2, “Deliverable 2.3: Report on simulation results and benchmark,” non-public, Jun. 2019.
- [13] T. Athay, R. Podmore, and S. Virmani, “A Practical Method for the Direct Analysis of Transient Stability,” *IEEE Trans. on Power Apparatus and Syst.*, PAS-98, no. 2, pp. 573–584, 1979, doi: 10.1109/TPAS.1979.319407.
- [14] Manitoba HVDC Research Centre, “IEEE 39 Bus System,” 22.05.218. [Online]. Available: https://www.pscad.com/uploads/knowledge_base/ieee_39_bus_technical_note.pdf
- [15] OPAL RT Technologies, “IEEE 39 – Bus Model in HYPERSIM,” non-public, May. 2018.
- [16] PROMOTioN WP 3, “Deliverable 3.7: Compliance evaluation results using simulations,” Brussels, Belgium, Feb. 2020. [Online]. Available: https://www.promotion-offshore.net/fileadmin/PDFs/D3.7_Compliance_evaluation_results_using_simulations.pdf
- [17] PROMOTioN WP 3, “Deliverable 3.1: Detailed functional requirements to WPPs,” Brussels, Belgium, Dec. 2016. [Online]. Available: https://www.promotion-offshore.net/fileadmin/PDFs/D3.1_PROMOTioN_Deliverable_3.1_Detailed_functional_requirements_to_WPPs.pdf
- [18] PROMOTioN WP 3, “Deliverable 3.2: Specifications of the control strategies and the simulation test cases,” Brussels, Belgium, Mar. 2017. [Online]. Available: https://www.promotion-offshore.net/fileadmin/PDFs/D3.2_Specifications_Control_strategies_and_simulation_test_cases.pdf
- [19] PROMOTioN WP 3, “Deliverable 3.4: Results on control strategies of WPPS connected to DR-HVDC,” Brussels, Belgium, Jan. 2018. [Online]. Available: https://www.promotion-offshore.net/fileadmin/PDFs/D3.4_PROMOTioN_Results_on_control_strategies_of_WPPs_connected_to_DR-HVDC.pdf
- [20] C. Buchhagen, C. Rauscher, A. Menze, and J. Jung, “BorWin1 – First Experiences with harmonic interactions in converter dominated grids,” in *ETG-Fb. 147: International ETG Congress 2015*, 2015.
- [21] C. Buchhagen, M. Greve, A. Menze, J. Jung, T. TSO, and GmbH, “Harmonic Stability – Practical Experience of a TSO,” in *Proceedings of the 15th Wind Integration workshop*, 2016.
- [22] X. Wang and F. Blaabjerg, “Harmonic Stability in Power Electronic-Based Power Systems: Concept, Modeling, and Analysis,” *IEEE Trans. Smart Grid*, vol. 10, no. 3, pp. 2858–2870, 2019, doi: 10.1109/TSG.2018.2812712.



- [23] N. Hatziaargyriou *et al.*, “Stability definitions and characterization of dynamic behavior in systems with high penetration of power electronic interfaced technologies,” Techreport, IEEE Power & Energy Society PES-TR77, 2020.
- [24] J. Sun *et al.*, “Renewable energy transmission by HVDC across the continent: system challenges and opportunities,” *CSEE JPES*, vol. 3, no. 4, pp. 353–364, 2017, doi: 10.17775/CSEEJPES.2017.01200.
- [25] PROMOTioN WP16, “Deliverable 16.5: Implementation of an Analytical Method for Analysis of Harmonic Resonance Phenomena,” Jun. 2019. [Online]. Available: https://www.promotion-offshore.net/fileadmin/PDFs/D16.5_Implementation_of_an_analytical_method_for_analysis_of_harmonic_resonance_phenomena_v2.pdf
- [26] J. Sun, “Impedance-Based Stability Criterion for Grid-Connected Inverters,” *IEEE Trans. Power Electron.*, vol. 26, no. 11, pp. 3075–3078, 2011, doi: 10.1109/TPEL.2011.2136439.
- [27] M. Quester, *Frequency Behavior of an MMC Test Bench System*. Preprint. Accepted at Energycon 2020, 2020. [Online]. Available: https://www.techrxiv.org/articles/Frequency_Behavior_of_an_MMC_Test_Bench_System/12063375/1
- [28] L. Bessegato, L. Harnefors, K. Ilves, and S. Norrga, “A Method for the Calculation of the AC-Side Admittance of a Modular Multilevel Converter,” *IEEE Trans. Power Electron.*, vol. 34, no. 5, pp. 4161–4172, 2019, doi: 10.1109/TPEL.2018.2862254.
- [29] L. Bessegato, A. Narula, P. Bakas, and S. Norrga, “Design of a Modular Multilevel Converter Prototype for Research Purposes,” in *20th European Conference on Power Electronics and Applications*, 2018.
- [30] M. Quester, F. Loku, V. Yelliseti, and R. Puffer, “Online Impedance Measurement of a Modular Multilevel Converter,” in *2019 IEEE PES Innovative Smart Grid Technologies Europe (ISGT-Europe)*, Bucharest, Romania, Sep. 2019 - Oct. 2019, pp. 1–5.
- [31] Ł. H. Kocewiak, J. Hjerrild, and C. L. Bak, “Wind turbine converter control interaction with complex wind farm systems,” *IET Renewable Power Generation*, vol. 7, no. 4, pp. 380–389, 2013, doi: 10.1049/iet-rpg.2012.0209.
- [32] D. van Hertem, O. Gomis-Bellmunt, and J. Liang, Eds., *HVDC grids: For offshore and supergrid of the future*. Hoboken, New Jersey: Wiley, 2016. [Online]. Available: <http://search.ebscohost.com/login.aspx?direct=true&scope=site&db=nlebk&AN=1170142>

